UNIVERSITY OF BELGRADE
SCHOOL OF ELECTRICAL ENGINEERING
UNIVERSITY OF ANTWERP
DEPARTMENT OF PHYSICS

Marko M. Grujić

Manifestations of intrinsic and induced magnetic properties of graphene nanostructures

Doctoral Dissertation

Belgrade, 2015.

УНИВЕРЗИТЕТ У БЕОГРАДУ
ЕЛЕКТРОТЕХНИЧКИ ФАКУЛТЕТ
УНИВЕРЗИТЕТ У АНТВЕРПЕНУ
ДЕПАРТМАН ЗА ФИЗИКУ

Марко М. Грујић

Испољавање сопствених и индукованих магнетских својстава графенских наноструктура

Докторска дисертација

Београд, 2015.

Committee members

dr Milan Ž. Tadić, Thesis Supervisor
Full Professor
School of Electrical Engineering, University of Belgrade

dr François M. Peeters, Thesis Supervisor
Full Professor
Physics Departement, University of Antwerp

dr Dejan Raković,
Full Professor
School of Electrical Engineering, University of Belgrade

dr Bart Partoens,
Full Professor
Physics Departement, University of Antwerp

dr Vlada Arsoski,
Associate Professor
School of Electrical Engineering, University of Belgrade

Day of the defense:

First and foremost I would like to thank Prof. Milan Tadić, my supervisor from the University of Belgrade, for guiding my scientific development since the second year undergraduate course in Quantum Mechanics which took place at the School of Electrical Engineering in 2007. I would like to think that his genuine love and enthusiasm for physics and, more importantly, his human qualities have rubbed off on to me, at least to a certain degree. My deepest gratitude goes out to him for being supportive of all my endeavors, and especially for having enough faith to let me explore unknown territories, which has been a tremendously enriching experience.

I am also indebted to Prof. François Peeters, my supervisor from the University of Antwerp, for welcoming me into his group with open arms. The time spent at UA has been essential for my professional and personal growth. Prof. Peeters' expertise in the field of condensed matter physics has had an invaluable contribution to this thesis. I am particularly grateful for the freedom he has allowed me in pursuing my research interests.

I would also like to thank my colleagues from Condensed matter theory group at the Physics Department of UA, as well as colleagues from the Physical electronics department of the School of Electrical Engineering at UB, who provided a stimulating company at lunch breaks and for various other activities. Additionally, I would like to thank my fellow orienteers in Serbia, especially those in my home club "Pobeda". Spending weekends running through the woods and mountains with them was not only beneficial for refreshing my thoughts, but has endowed me with a great, close-knit, community of friends.

Finally, I dedicate this thesis to my mother Ankica, and my girlfriend Milica.

Marko M. Grujić

Belgrade, December 15th, 2014.

Пре свега желео бих да се захвалим професору Милану Тадићу, мом ментору са Универзитета у Београду, за усмеравање мог научног развоја још од предмета "Квантна Механика" са друге године основних студија на Електротехничом Факлутету 2007. године,. Био бих срећан ако се макар део његове искрене љубави и ентузијазма за физику, и још важније његових људских квалитета током тог процеса пренео на мене. Дугујем му најдубљу захвалност због безрезервног пружања подршке за све моје напоре, а посебно због тога што је довољно веровао у мене да ми дозволи истраживање непозантих терена, што се показало као изузетно обогаћујуће искуство.

Такође сам захвалан професору Франсоа Петерсу, мом ментору са Универзитета у Антверпену, што ме је прихватио у своју групу раширених руку. Време које сам провео на УА је било кључно за моје професионално, али и лично сазревање. Експертско познавање области физике кондензованог стања професора Петерса је имало немерљив допринос овој тези. Посебно сам му захвалан због слободе коју ми је пружио у истраживачком раду.

Захвалност дугујем колегама из Групе за теорију кондензованог стања одсека за физику УА, као и колегама са Одсека за физичку електронику Електротехничког Факултета УБ, који су били стимулишуће друштво на паузама за ручак и другим активностима. Поред тога, хтео бих да се захвалим мојим друговима оријентирцима у Србији, поготово члановима мог клуба "Победа". Трчање кроз шуме и планине са њима не само што је било од користи за разбистравање мојих мисли, већ ме је обогатило великим бројем пријатеља.

Коначно, посвећујем ову дисертацију мојој мајци Анкици, и мојој девојци Милици.

Марко М. Грујић

Београд, 15. децембар 2014.

Manifestations of intrinsic and induced magnetic properties of graphene nanostructures

Abstract

The dissertation can be roughly divided into two parts. In the first part it deals with magnetic properties of quasi-zero dimensional graphene structures, such as nanodots and nanorings. In particular, a circular graphene quantum dot is analyzed in Chapter 3 using the Dirac-Weyl equation. The energy and the optical absorption spectra are computed for the case of the present external magnetic field. The results are obtained for two distinct boundary conditions, namely *infinite-mass* and *zigzag* boundary conditions, which model different physics in the structure with different edges. It is found that the energy spectrum of a dot with zigzag boundary condition exhibits a zero energy band regardless of the value of the magnetic field, while for the infinite mass boundary condition the zero energy states appear only for high magnetic fields in the form of the zeroth Landau level. The analytical results are compared to those obtained from the tight-binding model in order to show the validity range of the continuum model. It is found that the continuum model with infinite mass boundary condition describes rather well its tight binding counterpart, which can partially be attributed to blurring of the mixed edges by the staggered potential.

The mean-field Hubbard model is subsequently used to investigate the formation of the antiferromagnetic phase in hexagonal graphene quantum rings with inner zigzag edges. The outer edge of the ring is taken to be either zigzag or armchair, and it is found that both types of structures exhibit a larger antiferromagnetic interaction than hexagonal quantum dots. This difference could be partially ascribed to the larger number of zigzag edges per unit area in rings than in dots. Furthermore, edge states localized on the inner ring edge are found to hybridize differently than the edge states of dots, which results in important differences in the magnetism of graphene rings and dots. The largest staggered magnetization is found when the outer edge has a zigzag shape. However, narrow rings with armchair outer edge are found to have larger staggered magnetization than zigzag hexagons. The edge defects are shown to have the least effect on magnetization when the outer ring edge is armchair shaped.

In the second part of the dissertation, the focus is shifted onto bulk graphene structures with augmented properties, and the resulting transport traits. This part reflects recent trends in 2D materials research, involving sandwiching different layers together, enabling functionalities beyond those found in the constituent parts. These structures are termed van der Waals heterostructures, and in particular case of graphene enable engineering of massive quasiparticles, either through enhancement of spin-orbit coupling, or by breaking the inversion symmetry. This is of interest because in honeycomb Dirac systems with broken spatial symmetry for instance, orbital magnetic moments coupled to the valley degree of freedom arise due to the topology of the band structure, leading to valley-selective optical dichroism. On the other hand, in Dirac systems with prominent spin-orbit coupling, similar orbital magnetic moments emerge as well. It is shown that they are coupled to spin, but otherwise have the same functional form as the moments stemming from spatial inversion breaking. Moreover, the impact of these moments on graphene nano-engineered barriers with artificially enhanced spin-orbit coupling is studied in detail. In particular, the transmission properties of such barriers in the presence of a magnetic field are examined. The orbital moments are found to manifest in transport characteristics through spin-dependent transmission and conductance, making them directly accessible in experiments. Moreover, it is found that Zeeman-type effects appear without explicitly incorporating the Zeeman term in the models, i.e., by using minimal coupling and Peierls substitution in the continuum and tight-binding methods, respectively. It is shown that a quasi-classical view is able to explain all the observed phenomena.

Finally, the interplay of massive Dirac fermions with strain induced pseudomagnetic fields in 1D barriers is studied. The combined presence of spin-orbit coupling and broken spatial symmetry in bulk graphene results in a spin-valley dependent gap. Thus, a barrier with such properties can act as a filter, transmitting only opposite spins from opposite valleys. It is shown that the pseudomagnetic field in such a barrier will enforce opposite cyclotron trajectories for the filtered valleys, leading to their spatial separation. Since spin is coupled to the valley in the filtered states, this also leads to spin separation, demonstrating a spin-valley filtering effect. Furthermore, it is shown that filtering behavior can be controlled by electrical gating as well as by strain.

Keywords: graphene, magnetic field, magnetic moment, quantum dot, spin-orbit coupling, valley, transport

Scientific field: Electrical and Computer Engineering

Research area: Nanoelectronics and Photonics

UDC number: 621.3

Испољавање сопствених и индукованих магнетских својстава графенских наноструктура

Апстракт

Ова докторска дисертација се може грубо поделити у два дела. У првом делу, она се бави магнетским својствима квази-нулто димензионих графенских структура, као што су нанотачке и нанопрстенови. Конкретно, кружна графенска квантна тачка је анализирана у поглављу 3 користећи Дирак-Вејлову једначину. Енергетска стања и оптички апсорпциони спектар су израчунати за случај примењеног спољашњег магнетног поља. Резултати су добијени за два различита случаја, применом граничног услова *бесконачне масе* и такозваног *цикцак* граничног услова, који описују структуре са различитим врстама ивица. Пронађено је да енергетски спектар тачке за цикцак гранични услов подржава нултоенергетски ниво, без обзира на вредност магнетског поља, док се за гранични услов бесконачане масе нултоенергетска стања појављују само за високе вредности магнетског поља и то у облику нултог Ландауовог нивоа. Аналитички добијени резултати су затим упоређени са резултатима добијеним помоћу метода јаке везе, да би се одредила област важења континуалног модела. Пронађено је да се континуални модел са граничним условом бесконачне масе добро слаже са методом јаке везе, што се донекле може приписати минимизовању утицаја ивица, што је последица наизменичног потенцијала.

Након овога дисертација се бави анализом формирања антифероманетизма у хексагоналним графенским квантним прстеновима са цикцак унутрашњом ивицом користећи Хабардов модел у апроксимацији средњег поља. Спољна ивица прстена је или цикцак или фотељастог типа. Пронађено је да обе врсте структура показују већу склоност ка антифероманетизму него хексагоналне квантне тачке. Ова разлика се делимично може приписати већој дужини цикцак ивица у прстеновима него у тачкама. Поред тога, хибридизација ивичних стања локализованих на унутрашњој страни прстена је другачије природе него хибридизација стања на ивици тачака, што доводи до битних разлика магнетизма прстенова у односу на тачке. Највећа магнетизација је добијена за случај када је и спољашња ивица цикцак типа. Ипак, врло уски прстенови са

фотељастом спољашњом ивицом имају већу магнетизацију него шестоугаоне квантне тачке са цикцак ивицама. Такође је показано да ивични дефекти имају најмање утицаја на магнетизацију када је спољна страна прстена фотељастог типа.

Други део тезе је фокусиран на масивне графенске структуре са вештачким својствима, и њихове транспортне особине. Овај део дисертације представља скорашња истраживања 2Д материјала која се баве слагањем различитих слојева, што омогућује појаву функционалности која се не може наћи у појединачним материјалима. Овакве структуре се називају ван дер Валсове хетероструктуре и код графена омогућују инжењеринг масивних квазичестица, било помоћу спин-орбитне интеракције, било нарушавањем инверзионе симетрије. Занимљив ефекат је да услед топологије енергетске структуре сачастих Диракових система без просторне симетрије долази до појаве орбиталних магнетних момената спрегнутих са долинским степеном слободе, што доводи до долински-селективног оптичког дихроизма. С друге стране, у Дираковим системима са истакнутом спин-орбит интеракцијом појављују се слични магнетски моменти. Показано је да су ови моменти спрегнути са спином, али имају идентичну функционалну зависност као и магнетни моменти настали услед непостојања инверзионе симетрије. Напослетку, анализиран је утицај ових момената на нанобаријере формиране у графену помоћу вештачки појачане спин-орбитне интеракције. Конкретно, испитивана су трансмисиона својства ових баријера у присуству магнетног поља. Орбитални моменти се манифестују у транспортним особинама спин-зависном трансмисијом и проводношћу, што их чини директно видљивим у експериментима. Пронађено је да се ефекти Земановог типа јављају без експлицитне употребе Земановог члана у моделима, тј., користећи само минимално спрезање и Пајерлсову замену у континуалном и методу јаке везе, респективно. Показано је да квазикласични опис добро објашњава све примећене ефекте.

Коначно, анализирана је спрега масивних Диракових фермиона са псеудомагнетским пољима изазваним напрезањем у 1Д баријерама. Присуство спин-орбитне интеракције и непостојање просторне симетрије има за последицу појављивање спин-долински зависног енергетског процепа. Због тога се оваква баријера понаша као филтар, пропуштајући само супротне спинове из супротних долина. Показано је да псеудомагнетско поље доводи до појаве супротних циклотронских трајекторија у супротним долинама, доводећи до њиховог просторног раздвајања. Пошто је спин спрегнут са долином у филтрираним стањима, ово такође доводи и до раздвајања спинова, што свеукупно пред-

ставља ефекат спин-долинске филтрације. Поред тога показано је да се ефекат филтрирања може контролисати електричним гејтовима као и напрезањем.

Кључне речи: графен, магнетско поље, магнетни моменат, квантна тачка, спин-орбитна интеракција, долина, транспорт

Научна област: Електротехничко и рачунарско инжењерство

Ужа научна област: Наноелектроника и фотоника

УДК број: 621.3

Contents

Chapter 1

Introduction

1.1 Elementary properties of carbon and its allotropes

Carbon is arguably the most versatile chemical element in nature. One illustration of this is offered by two of its 3D allotropes: diamond and graphite. While diamond is a very hard, transparent insulator, graphite is a soft, opaque conductor. Furthermore, carbon is a prolific atomic connector, able to form more compounds than any other element in nature, and allows unique and complex structures to take shape [1]. The molecules it builds also display a Goldilocks-like combination of stability and reactivity, a feat essential for metabolism, which makes carbon the building block of life. Such a wide diversity of properties stems from the electronic configuration of carbon.

Carbon has 6 electrons, which in the ground state occupy the $1s^2 2s^2 2p^2$ configuration. However, once the possibility of forming covalent bonds arises, the excited state becomes energetically favorable, the basis of which is formed by the orbitals $2s$, $2p_x$, $2p_y$ and $2p_z$ [1, 2]. The hybridization of these orbitals gives rise to a variety of ways carbon atoms can bond with other atoms, including themselves. For instance, in diamond the valence electrons form the sp^3 hybridization, resulting in four σ bonds between neighboring sites. While diamond has been familiar since antiquity, recent additions to the family of carbon allotropes include the exotic fullerens: quasi-0D buckyballs and quasi-1D nanotubes. These could be envisaged as a single membrane of triply connected carbon atoms wrapped around in a spherical and cylindrical shape, respectively. These low-dimensional structures were discovered at

the very beginning of the nanotechnology era, and feature a mixture of sp^2 and sp^3 hybridization due to their highly curved surfaces. Larger bending requires higher ratios of tetravalent orbitals, which in turn increases the amount of unsaturated bonds, making the structure more reactive and at the same time ties up more energy in the form of strain [3, 4]. It should not be surprising then that sheets of triply connected carbon atoms favor pure sp^2 hybridization, which is realized only in a fully planar structure - graphene.

Therefore, graphene is a honeycomb monolayer of carbon atoms connected with three σ bonds. Apart from being the fabric from which carbon's 0D and 1D allotropes are fashioned, stacking graphene layers on top of each other forms graphite, carbon's 3D allotrope. In fact graphene derives its name from graphite, which is itself an $18-$th century coinage rooted in the Greek word for writing; the sufix -ene refers to the 2D nature of its structure akin to benzene. The basic properties of graphene shed light on this feature of graphite. Since in graphene the connections between carbon atoms are completely due to in-plane sp^2 hybridization, made up of s, p_x and p_y orbitals, the remaining valence electron is to be found in the p_z orbital, wandering perpendicularly to the sheet. The sp^2 bonds are the strongest in nature, making each sheet robust. On the other hand, p_z orbitals hybridize weakly between the adjacent layers, thus keeping them loosely connected through the van der Waals forces. This loose connection, easily broken by hand, is what gives the "lead" pencils the ability to write.

While in hindsight the theory sounds clear and straightforward, imagining a stable, freestanding, one-atom thick structure requires a leap of faith, which might explain why graphene was discovered so late. This is further substantiated formally by the famous Mermin-Wagner theorem [5], stating that no crystal can be stable in two dimensions, with the conventional wisdom on this matter being laid out even earlier, by Peierls and Landau [6, 7]. It was therefore quite unexpected and surprising to learn about the observation of monolayer graphene, reported in 2004, the sheets of which were peeled away from a high quality graphite sample in a rather low-tech process known as micromechanical exfoliation, also known as the Scotch-tape technique [8]. The fact that this material displayed remarkable crystal quality and room-temperature stability sparked a world-wide research frenzy, aimed at tapping the previously unexplored theoretical and experimental resources that suddenly appeared. Such a widespread effort resulted in an expansion of knowledge further than anyone could have imagined, providing new and rich physics along

the way. Amongst other things, graphene research stimulated the discovery of time-reversal invariant topological insulators, which is proving to be a remarkably fruitful field of study on its own [9, 10].

One of the main selling points that fueled the graphene-frenzy were its extraordinary material properties. Graphene is currently the strongest and stiffest material known [11], while at the same time having the best thermal conductivity [12], outperforming its carbon cousins such as nanotubes and various forms of diamond. Moreover, it has the best electrical conductivity ever measured [13], in no small part thanks to record high electron mobility [13–15]. The fact that graphene features electrical conductivity higher than the most conductive metals, such as silver, copper or gold, is even more astonishing having in mind that graphene is not a metal at all, but a semimetal, or, alternatively, a zero-gap semiconductor, with a vanishing density of states at the Fermi energy. Despite this, the conductivity does not vanish at this point, reflecting a peculiar underlying nature of what is best described as charge-carrying quasiparticles of graphene. As it turns out, the band structure of graphene does not bear resemblance to that of massive particles described by the Schrödinger equation; this usual description of semiconducting materials in which quadratic dispersion relation is attributed to an effective mass is inadequate here. Instead, its low-energy excitations obey a linear energy-momentum relation, akin to photons, with the difference that the charge carriers in graphene are electrically charged fermions of spin one-half. In other words, graphene is a material in which electrons behave as ultrarelativistic massless particles, describable only by the Dirac equation, forged out of the union of quantum mechanics and special relativity. Therefore graphene is a unique and exotic condensed matter emulator of relativistic quantum physics, a property ultimately responsible for the first unambiguous and definitive detection of single layer graphene signatures experimentally, through the so called anomalous quantum Hall effect [16, 17]. All of the fundamental electronic properties of graphene are quite easily obtainable by standard procedures such as tight binding (TB) modeling, while the continuum picture emerges as its low-energy expansion. At the same time this process provides great insight and the ability to grasp the physics unexpected at the solid state level, so it becomes beneficial to analyze these problems analytically. This is what the following sections of this chapter are devoted to.

1.2 Tight-binding band structure of graphene

We start with the Schrödinger equation in it's most fundamental, second quantized form in two dimensions

$$H = \int_{\mathbf{r}} d\mathbf{r}\Psi^\dagger(\mathbf{r}) \left[-\frac{\hbar^2}{2m}\nabla^2 + U(\mathbf{r})\right] \Psi(\mathbf{r}). \tag{1.1}$$

Here $\Psi^\dagger(\mathbf{r})$ and $\Psi(\mathbf{r})$ are quantum field creation and annihilation operators, and $U(\mathbf{r})$ is the atomic potential landscape due to the lattice. As already mentioned, the bonds that hold carbon atoms together in the honeycomb shape originate from the s, p_x and p_y orbitals, which hybridize strongly and thus shift the energies of the corresponding σ bands away from the Fermi level, leaving them without any impact on the electronic structure of graphene. On the other hand, since we focus on a single layer here, the leftover p_z orbitals do not have an adjacent layers to bind to, which leaves them free to hybridize relatively weakly among themselves. As we will soon show, this will result in bands touching conically at the Fermi energy, near certain points in the Brillouin zone. We therefore chose to expand the quantum field operators in a basis of atomic p_z orbitals of carbon atoms $\phi(\mathbf{r})$

$$\begin{aligned}\Psi^\dagger(\mathbf{r})\,|0\rangle &= |\mathbf{r}\rangle \\ &= \sum_{i\alpha} |i\alpha\rangle\,\langle i\alpha|\mathbf{r}\rangle \\ &= \sum_{i\alpha} \phi^*\left(\mathbf{r}-\mathbf{R}_{i\alpha}\right) c_{i\alpha}^\dagger\,|0\rangle\,,\end{aligned} \tag{1.2}$$

and similarly

$$\Psi = \sum_{i\alpha} \phi\left(\mathbf{r}-\mathbf{R}_{i\alpha}\right) c_{i\alpha}, \tag{1.3}$$

where i denotes the unit cell in the sum. The periodicity of the honeycomb structure can only be appreciated by acknowledging the fact that there are two unequal atomic sites. This basis can be imagined to consist out of two interpenetrating hexagonal sublattices A and B, which are labeled by the variable $\alpha \in \{A, B\}$, as depicted in Fig. 1.1(a), and whose position in space is denoted by $\mathbf{R}_{i\alpha}$. In other words, the honeycomb lattice is not a Bravais lattice, and the three nearest neighbors of a carbon atom in one sublattice belong to the opposite sublattice. $c_{i\alpha}^\dagger$ and $c_{i\alpha}$

are the creation and annihilation operators of the electron for the p_z orbital at the appropriate site. Note that in a certain way the field operators represent the superposition of all the ways to create a particle at a given position. Replacing Eqs. (1.2) and (1.3) in Eq. (1.1) one obtains the following operator

$$H = \int_{\mathbf{r}} d\mathbf{r} \sum_{i\alpha i'\alpha'} \phi^* \left(\mathbf{r} - \mathbf{R}_{i\alpha}\right) c^\dagger_{i\alpha} \left[-\frac{\hbar^2}{2m}\nabla^2 + U(\mathbf{r})\right] \phi \left(\mathbf{r} - \mathbf{R}_{i'\alpha'}\right) c_{i'\alpha'}. \tag{1.4}$$

Only two classes of integrals are relevant in the most simple procedure, which turns out to describe graphene rather well [18]. The first one represents the site energy ϵ_α of the α sublattice sites

$$\epsilon_\alpha = \int_{\mathbf{r}} d\mathbf{r} \phi^* \left(\mathbf{r} - \mathbf{R}_{i\alpha}\right) \left[-\frac{\hbar^2}{2m}\nabla^2 + U(\mathbf{r})\right] \phi^* \left(\mathbf{r} - \mathbf{R}_{i\alpha}\right). \tag{1.5}$$

This is basically the energy of the p_z orbitals. In graphene this quantity does not depend on the sublattice, and therefore only has the effect of shifting the Fermi energy, so we shall ignore it. Note that one must take this factor into account when dealing with hexagonal boron-nitride (hBN) for instance, since in that case the sublattices A and B in the honeycomb structure are made up of boron and nitrogen atoms, rendering their on-site energies different. In fact, breaking the sublattice symmetry will result in the appearance of a band gap in honeycomb crystals in general, giving rise to massive quasiparticles. Nevertheless, these systems will still require the relativistic quantum treatment, as will be demonstrated below. The only remaining non-zero integral is the nearest neighbor matrix element, the so called hopping integral

$$-t = \int_{\mathbf{r}} d\mathbf{r} \phi^* \left(\mathbf{r} - \mathbf{R}_{i\alpha}\right) \left[-\frac{\hbar^2}{2m}\nabla^2 + U(\mathbf{r})\right] \phi \left(\mathbf{r} - \mathbf{R}_{i\tilde{\alpha}}\right), \tag{1.6}$$

where $t \approx 2.7$eV is the hopping term. Note that we anticipated the negative sign, and defined the hopping term to be positive. The Hamiltonian now reduces to the standard tight binding picture

$$H = -t \sum_{\langle i\alpha i'\alpha'\rangle} c^\dagger_{i\alpha} c_{i'\alpha'}. \tag{1.7}$$

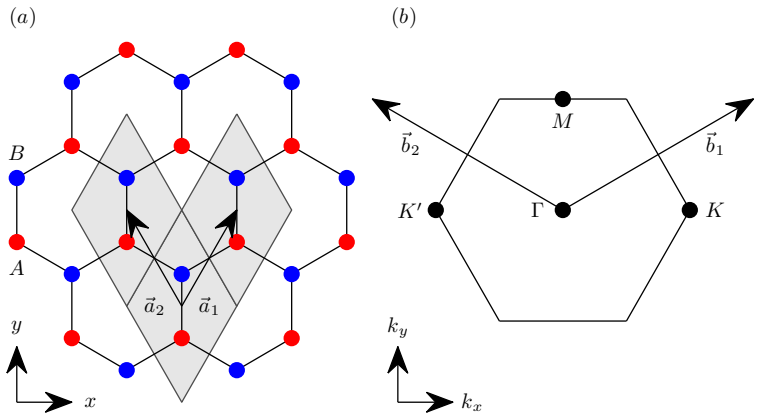

Figure 1.1: (a) Crystal lattice of graphene. Unit vectors $\mathbf{a}_1$ and $\mathbf{a}_2$ connect adjacent unit cells, which consist out of a two-atom basis, A and B. (b) The first Brillouin zone and the corresponding reciprocal unit vectors $\mathbf{b}_1$ and $\mathbf{b}_2$, with distinctive points in the reciprocal space K, K', M and Γ. This is the Wigner-Seitz cell of the reciprocal lattice.

The angled brackets denote that the hopping occurs only between the nearest neighbors in this model. In order to emphasize the 2D periodicity of the lattice, the Hamiltonian needs to be reordered. To do this, we define the two unit vectors, depicted in Fig. 1.1(a), as

$$\mathbf{a}_{1/2} = a\left(\frac{\pm\sqrt{3}}{2}, \frac{3}{2}\right), \tag{1.8}$$

where $a = 0.142$ nm is the carbon-carbon distance. The two-atom basis unit cells are also shown in Fig. 1.1(a), while the corresponding first Brillouin zone is depicted in Fig. 1.1(b), alongside with the reciprocal unit vectors and characteristic points in the inverse space. Denoting a unit cell with the coordinate $\mathbf{R}$ of the middle of a line joining the two atoms, a manifestly periodic Hamiltonian can be written

$$H = -t\sum_{\mathbf{R}} c^{\dagger}_{\mathbf{R}A}\left(c_{\mathbf{R}-\mathbf{a}_1 B} + c_{\mathbf{R}-\mathbf{a}_2 B} + c_{\mathbf{R}B}\right) + h.c.. \tag{1.9}$$

Here h.c. stands for Hermitian conjugate. Thus the Hamiltonian describes the hopping within a given unit cell, and between this and the adjacent cells displaced by $-\mathbf{a}_1$ and $-\mathbf{a}_2$ with respect to it, for all cells. In order to diagonalize the Hamiltonian at hand, it is helpful to apply the thermodynamic limit, by imagining that there are N unit cells in a superlattice, then enforcing the periodic boundary conditions at the edges, and subsequently letting $N \to \infty$. In this way we are able to apply a unitary (Fourier) transformation taking us into the momentum basis

$$c_{\mathbf{R}\alpha} = \frac{1}{\sqrt{N}} \sum_{\mathbf{k}} e^{i\mathbf{k}\cdot\mathbf{R}} c_{\mathbf{k}\alpha}, \tag{1.10}$$

while the Brillouin zone becomes a continuous space. Note that we chose the same phase factor regardless of the sublattice index. This is not necessary, but it is more convenient [2, 19]. The periodic boundary conditions ensure the closure relation

$$\frac{1}{N} \sum_{\mathbf{R}} e^{i(\mathbf{k}-\mathbf{k}')\mathbf{R}} = \delta_{\mathbf{k}\mathbf{k}'}. \tag{1.11}$$

This procedure is formally equivalent to applying the Bloch theorem (see Appendix A). Replacing this into the periodic Hamiltonian we obtain

$$\begin{aligned} H =& -\frac{t}{N} \sum_{\mathbf{R}\mathbf{k}\mathbf{k}'} e^{-i\mathbf{k}\cdot\mathbf{R}} c^{\dagger}_{\mathbf{k}A} \left(e^{i\mathbf{k}'\cdot(\mathbf{R}-\mathbf{a}_1)} c_{\mathbf{k}'B} + e^{i\mathbf{k}'\cdot(\mathbf{R}-\mathbf{a}_2)} c_{\mathbf{k}'B} + e^{i\mathbf{k}'\cdot\mathbf{R}} c_{\mathbf{k}B} \right) \\ =& -t \sum_{\mathbf{k}} c^{\dagger}_{\mathbf{k}A} c_{\mathbf{k}B} \left(e^{-i\mathbf{k}\cdot\mathbf{a}_1} + e^{-i\mathbf{k}\cdot\mathbf{a}_2} + 1 \right) + h.c.. \end{aligned} \tag{1.12}$$

Thus the diagonalized Hamiltonian in momentum space takes the form (here we explicitly represent the sublattice degree of freedom through spinors)

$$H = \sum_{\mathbf{k}} \begin{bmatrix} c^{\dagger}_{\mathbf{k}A}, c^{\dagger}_{\mathbf{k}B} \end{bmatrix} \begin{bmatrix} 0 & \gamma(\mathbf{k}) \\ \gamma^{\dagger}(\mathbf{k}) & 0 \end{bmatrix} \begin{bmatrix} c_{\mathbf{k}A} \\ c_{\mathbf{k}B} \end{bmatrix}, \tag{1.13}$$

with $\gamma(\mathbf{k}) = -t\left(1 + e^{-i\mathbf{k}\cdot\mathbf{a}_1} + e^{-i\mathbf{k}\cdot\mathbf{a}_2}\right)$. Obviously the Hamiltonian remains to be diagonalized in the sublattice subspace. The eigenvalues of the previous matrix result in the energy dispersion

$$\epsilon(\mathbf{k}) = \pm t \sqrt{3 + 2\cos\left(\sqrt{3}k_x a\right) + 4\cos\left(\sqrt{3}k_x a/2\right)\cos\left(3k_y a/2\right)}, \tag{1.14}$$

where $+$ $(-)$ refers to the conduction (valence) band stemming from the anti-bonding (bonding) state, also referred to as the π^* (π) band. The dispersion relation, Eq. (1.14), is shown in Fig. 1.2. One can see that near certain points in the inverse space, the bonding and anti-bonding states are degenerate, i.e. the conduction and the valence band touch. Even though it appears that there are six such points, the periodicity of the dispersion in the inverse space ensures that only two of them are unique. Those points are $\mathbf{K}_\tau = \left(\tau\frac{4\pi}{3\sqrt{3}a}, 0\right)$, where we explicitly include the

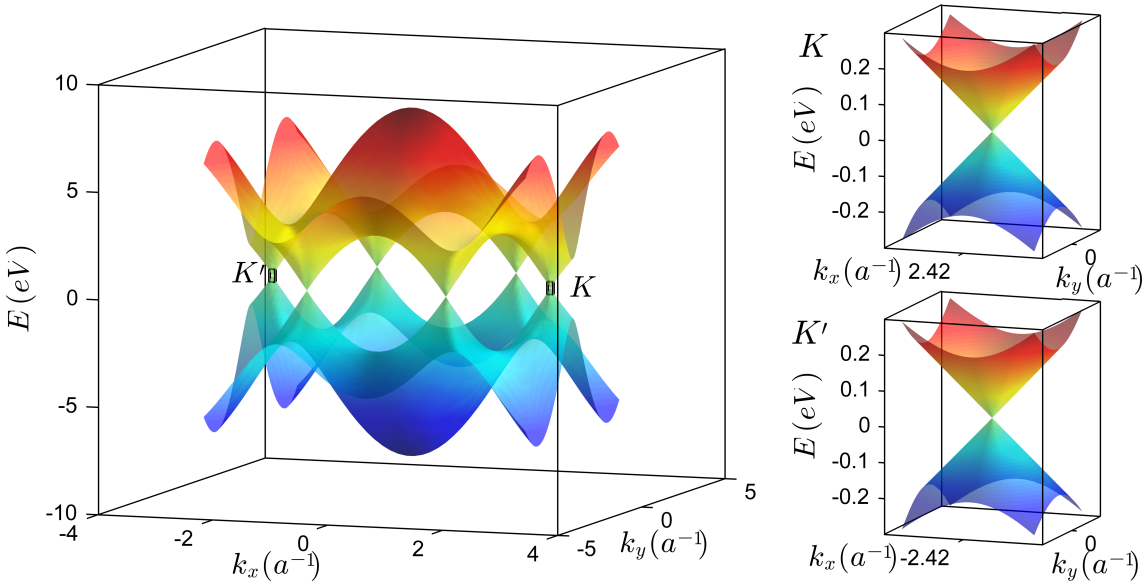

Figure 1.2: Energy dispersion of graphene, as obtained by the nearest neighbor tight binding method. The conduction and valence bands touch at the two distinct valleys. Insets show that this forms low-energy conical dispersion near the K and K' points.

valley index $\tau = \pm 1$, denoting the K and K' valley, respectively. This occurs because the effective hopping between the two sublattices in the momentum basis, $\gamma(\mathbf{k})$, vanishes, which also means that states at this particular point will have a probability amplitude either on A or on B sublattice. Since graphene is half-filled it means it is a semimetal.

1.3 The ultrarelativistic quasiparticles around the Dirac points

The insets in Fig. 1.2 show that the low-energy excitations in the two valleys experience conical dispersion. The resulting linear energy-momentum relationship resembles that of ultrarelativistic particles. With this in mind, we proceed to Taylor expand the kernel (1.13) up to linear terms around these points

$$\begin{aligned} \gamma\left(\mathbf{K}_\tau + \mathbf{q}\right) &= \gamma\left(\mathbf{K}_\tau\right) + \mathbf{q} \cdot \nabla_{\mathbf{k}} \gamma\left(\mathbf{K}_\tau\right) + \ldots \\ &= \tau \frac{3ta}{2} q_x - i \frac{3ta}{2} q_y + \ldots \end{aligned} \tag{1.15}$$

Then, by promoting the momenta displacements to operators,

$$(q_x, q_y) \to -i\,(\partial/\partial_x, \partial/\partial_y)$$

we obtain the effective continuum theory for low-energy quasiparticles, in which the underlying atomic structure is neglected, since the influence of the crystal lattice on the electron motion is inherent in it. This procedure is also known as the effective mass model, or the $\mathbf{k}\cdot\mathbf{p}$ model, with the resulting wave function being the envelope of the detailed atomic wave function. One benefit of the continuum approach is that it allows one to study large structures analytically, while the tight-binding approach is limited to relatively small structures due to the computational complexity of the numerical scheme. The continuum Hamiltonian reads

$$H = \hbar v_F \begin{bmatrix} 0 & q_x - iq_y & 0 & 0 \\ q_x + iq_y & 0 & 0 & 0 \\ 0 & 0 & 0 & -q_x - iq_y \\ 0 & 0 & -q_x + iq_y & 0 \end{bmatrix}, \tag{1.16}$$

where $v_F = \frac{3ta}{2\hbar} \approx 10^6$ m/s is the energy-independent Fermi velocity, at which the electrons travel inside graphene. This Hamiltonian is written in the

$$[\Psi_{AK}, \Psi_{BK}, \Psi_{AK'}, \Psi_{BK'}]^T$$

basis. The specific form of the Hamiltonian depends on the orientation of the axis used and on the basis implicitly assumed, and varies significantly in the literature [2, 20]. However in both valleys, and in all forms the low energy dispersion is linear. It is instructive to reorder the basis to the form $[\Psi_{AK}, \Psi_{BK}, \Psi_{BK'}, \Psi_{AK'}]^T$, which allows one to write the Hamiltonian in the compact form

$$H = \hbar v_F \tau_z \otimes \boldsymbol{\sigma}\cdot\mathbf{k}, \tag{1.17}$$

where τ_z is the Pauli z matrix operating in the valley subspace, $\boldsymbol{\sigma} = (\sigma_x, \sigma_y)$ is the vector of Pauli matrices operating in the sublattice subspace, and $\otimes$ denotes the tensor product. Equation (1.17) is now fully analogous to the celebrated Dirac-Weyl equation, the relativistic quantum equation corresponding to massless fermions. Since neutrinos have negligible mass, they are often described by this equation, leading to the popular picture, according to which carriers in graphene behave as

charged neutrinos [21].

There are four points that must be stressed here. i) The Dirac-Weyl equation for neutrinos is fully three-dimensional, the equation describing electrons in graphene operates in the 2D geometrical space. ii) The $\boldsymbol{\sigma}$ matrices in the neutrino case operate in the real spin space, while they denote the sublattice degree of freedom in graphene, consequently referred to as pseudospin degree of freedom as well. iii) Even though non-relativistic Schrödinger equation was our starting point, in the end we obtained the Dirac-Weyl equation of the relativistic quantum theory in the process. Therefore this is only an effective low-energy approximation, and not in any way some manifestation of the relativistic nature of carbon's valence electrons. iv) While massless neutrinos travel at the speed of light, electrons in graphene travel at the Fermi velocity v_F, which is approximately 300 times slower. This leads to a frequent misconception that electrons in graphene travel at speeds so great that they can only be described by the relativistic quantum theory. While it is true that electrons in graphene travel very fast, the fact of the matter is that even if this speed was orders of magnitude slower one would still have to use the Dirac-Weyl ultrarelativistic equation in order to properly describe the conical dispersion. It is the masslessness of the carriers that forces this prescription, and not their speed. Due to these properties, K and K' are known as Dirac points, while the linear low-energy dispersion in their vicinity is referred to as the Dirac cone. Note that, while it results in breaking of the electron-hole symmetry, including the next-nearest neighbor hopping in the starting model will not result in first order corrections to the low energy dispersion [18].

Another frequent misconception is that electrons in graphene are a table-top experiment in quantum electrodynamics (QED). While charge carriers on a honeycomb lattice do effectively behave as relativistic quantum particles, and are treated as such through the Dirac-Weyl equation, this approach is almost always short of the true quantum field theory. One way to see this is to note that one of the most famous achievements of QED, popularized by Feynman, is the precise calculation of the anomalous magnetic moment. The Dirac equation does not capture this small deviation of the $g-$factor away from two. Another way to see it is through the fact that position and momenta are still treated as operators in the present theory, while they are demoted to parameters in quantum field theories.

One more important thing is worth pointing out. The valley subspace, represented by τ_z in Eq. (1.19), ensures the existence of two effectively independent, and

nearly identical Dirac-Weyl fermions. The only feature distinguishing these quasiparticles is called helicity. In the case of graphene, the helicity operator is defined as the projection of the sublattice pseudo-spin on the direction of the momentum

$$h = \frac{\boldsymbol{\sigma} \cdot \mathbf{k}}{|\mathbf{k}|}. \tag{1.18}$$

Referring back to Eq. (1.17), one can easily verify that in the conduction band $h = +1$ (-1) in K (K') valley, meaning that the pseudospin is pointing parallel (antiparallel) to the momentum, while the opposite is true in the valence band. The states with $h = +1$ $(h = -1)$ are also known as right-handed (left-handed). This situation corresponds exactly to the relativistic Dirac-Weyl equation for massless neutrinos, except that all neutrinos (antineutrinos) in nature are only found to be left-handed (right-handed), while in graphene both states are allowed thanks to the existence of the additional valley flavor.

Note that it might be misleading to compare the helicity in the two valleys though. This is because we have chosen a different sublattice basis in the K' valley as opposed to the K valley, so that the Hamiltonian corresponds exactly to the one for the neutrinos. For instance, one could also chose the $[\Psi_{AK}, \Psi_{BK}, -\Psi_{BK'}, \Psi_{AK'}]^T$ basis, leading to the so-called valley-isotropic Hamiltonian [20]

$$H = \hbar v_F \tau_0 \otimes \boldsymbol{\sigma} \cdot \mathbf{k}, \tag{1.19}$$

where τ_0 is a 2×2 unit matrix. In this way, both valleys feature a right-handed (left-handed) Dirac-Weyl fermion in the conduction (valence) band. What is important to stress though, is that the pseudospin is tied to the momentum direction, regardless of the representation chosen. The most important consequence of this is that any normal-incidence backscattering process must include pseudospin flipping. The lack of any sublattice symmetry breaking potential (such as the staggered or sufficiently steep electric potential) capable of doing this, will lead to pseudospin conservation, which is the cause of the so called Klein tunneling [22, 23].

Finally, the valley subspace can be trivially taken into account, through the use of the valley quantum number $\tau = +1$ $(\tau = -1)$ for K (K') valley, which is beneficial since it reduces the size of the spinors and matrices used in the derivations. Then, after adopting the same basis for both valleys, $[\Psi_A, \Psi_B]^T$, one is left with the Hamiltonian

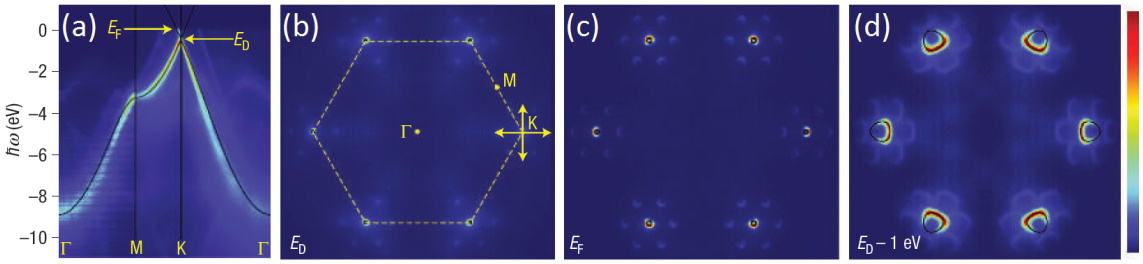

Figure 1.3: ARPES measurements verifying the TB band structure of graphene. (a) Cut along principal momentum direction gives a very good match with the theoretical results for $t = 2.82$ eV. (b-d) Energy cut shows how the conical dispersion diverges from a near-perfect linear one, and deforms through trigonal warping. Adapted from [24].

$$H = \hbar v_F \left(\tau k_x \sigma_x + k_y \sigma_y\right), \tag{1.20}$$

with the corresponding plane-wave given by

$$\Psi = \frac{e^{i\mathbf{k}\cdot\mathbf{r}}}{\sqrt{2}} \begin{bmatrix} 1 \\ \alpha\tau e^{i\tau\phi} \end{bmatrix}, \tag{1.21}$$

where $\alpha = +1$ (-1) denotes the conduction (valence) band, and $\phi = \arctan k_y/k_x$ is the angle of phase propagation with respect to the x axis.

In the end, we would like to stress that besides the indirect, albeit unambiguous, verification of the ultrarelativistic nature of graphene's quasiparticles through their magnetic properties (which are covered in Section 1.5), direct measurements of the band structure are accessible via the angle resolved photoemission spectroscopy (ARPES). This procedure is based on one of the most famous experiments which stimulated the development of quantum theory - the photoelectric effect. Energies and momenta involved in the photon-electron scattering must obey the laws of conservation, enabling precise reconstruction of the band structure throughout the Brillouin zone, and away from the Fermi energy. The corresponding measurements from Ref. [24] are depicted in Fig. 1.3, and spectacularly confirm the validity of the simple nearest-neighbor, single-orbital tight binding calculations we presented here. In particular, Fig. 1.3(a) compares the dispersion given by Eq. (1.14) (black line) with the experimentally detected energy and momenta of ejected electrons in the valence band along the principal directions, shown by a colormap. Note that this sample is slightly electron-doped, which is expected for a layer grown epitaxially on SiC [24]. Figs. 1.3(b-d) depict the energy cut through the dispersion relation, and

a deviation from the conical spectrum, called trigonal warping, which emerges for sufficiently energetic quasiparticles (Fig. 1.3(d)).

1.4 Massive relativistic particles: spin-orbit coupling and the staggered potential

The second half of the thesis deals with spin-orbit interaction, staggered potential and their interplay with the (pseudo)magnetic field. Even though spin-orbit interaction in intrinsic graphene is vanishingly small due to the small atomic number, there are some functionalization techniques through which this property can be enhanced. Similarly, a staggered potential does not appear naturally in graphene, but can be induced by forming the so-called van der Waals heterostructures. Therefore, the influence of these parameters on the band structure, effective continuum theories and the nature of quasiparticles they describe is not only of academic significance, but also practically relevant. In this section, we will give a basic introduction, leaving the practical details and particular experimental achievements for the introduction of Chapter 5.

The tight binding model with spin-orbit interaction (the celebrated Kane-Mele model [9]), alongside with the staggered potential is

$$H = -t \sum_{\langle i\alpha i'\alpha'\rangle} c^{\dagger}_{i\alpha} c_{i'\alpha'} + i\frac{\Delta_{SO}}{3\sqrt{3}} \sum_{\langle\langle i\alpha, j\alpha\rangle\rangle} s\nu_{ij} c^{\dagger}_{i\alpha} c_{j\alpha} + \Delta \sum_{i\alpha} (-1)^{\alpha} c^{\dagger}_{i\alpha} c_{i\alpha}. \tag{1.22}$$

The first term describes the usual hopping between nearest neighbor p_z orbitals, and is identical for both spins. The second term describes the intrinsic spin-orbit coupling (SOC), through the next-nearest-neighbor (NNN - symbolized by double brackets) hopping amplitude Δ_{SO}. Note that ν_{ij} determines the sign of the hopping; it is positive (negative) if an electron makes a right (left) turn at the intermediate atom in hopping from site j to site i. $s = +1$ ($s = -1$) is the spin quantum number denoting spin up $\uparrow$ (spin down $\downarrow$). It is important to stress that the single-orbital SOC part of the Hamiltonian is only phenomenological, since the underlying microscopic process leading to the appearance of the intrinsic SOC necessarily includes coupling with other orbitals. In particular, the entire process is still NNN in nature, and besides the atomic spin-orbit coupling, it also involves hopping (which are integrated out in the

effective Kane-Mele model) through either σ bands or d orbitals of the intermediate atom as well [25, 26]. The latter is dominant in determining the size of the SOC gap in pure graphene [27].

The final part of the Hamiltonian represents the so-called staggered potential, where $(-1)^\alpha$ is $+1$ (-1) on the A (B) sublattice; hence this term has opposite values on opposite sublattices, and appears when describing a material with inequivalent on-site energies on the two sublattices. This occurs either because the basis orbital energies are different on the two sublattices (since the sublattices are composed out of different atomic species - hBN), or due to a buckled lattice structure allowing a perpendicularly applied electric field to distinguish the two sublattices energetically, as is the case in silicene and germanene for example. Note that, while these effects do in general shift the zero energy point, the only non-trivial effect is the difference in on-site energies between the two sublattices, which can always be represented through a symmetric term by declaring the new zero point.

Let us focus now on the spin-orbit part of the Hamiltonian in order to obtain its form in momentum space. Indeed, the first part of the Hamiltonian was already studied, while the third part is trivial to write in momentum space. Rewriting H_{SO} in a manifestly periodic form one obtains

$$\begin{aligned} H_{SO} = is\frac{\Delta_{SO}}{3\sqrt{3}}\sum_{\mathbf{R}} & c^\dagger_{\mathbf{R}A}\left(-c_{\mathbf{R}+\mathbf{a}_1 A} + c_{\mathbf{R}+\mathbf{a}_2 A} + c_{\mathbf{R}+\mathbf{a}_1-\mathbf{a}_2 A}\right) \\ & + c^\dagger_{\mathbf{R}B}\left(c_{\mathbf{R}+\mathbf{a}_1 B} - c_{\mathbf{R}+\mathbf{a}_2 B} - c_{\mathbf{R}+\mathbf{a}_1-\mathbf{a}_2 B}\right) + h.c.. \end{aligned} \tag{1.23}$$

Here the sum again runs over all unit cells. Enforcing a unitary transformation to the momentum basis, as in the previous subsection, we get

$$\begin{aligned} H_{SO} =& is\frac{\Delta_{SO}}{3\sqrt{3}N}\sum_{\mathbf{R}\mathbf{k}\mathbf{k}'} e^{-i\mathbf{k}\cdot\mathbf{R}} c^\dagger_{\mathbf{k}A} c_{\mathbf{k}A}\left(-e^{i\mathbf{k}'\cdot(\mathbf{R}+\mathbf{a}_1)} + e^{i\mathbf{k}'\cdot(\mathbf{R}+\mathbf{a}_2)} + e^{i\mathbf{k}'\cdot(\mathbf{R}+\mathbf{a}_1-\mathbf{a}_2)}\right) \\ & + e^{-i\mathbf{k}\cdot\mathbf{R}} c^\dagger_{\mathbf{k}B} c_{\mathbf{k}B}\left(e^{i\mathbf{k}'\cdot(\mathbf{R}+\mathbf{a}_1)} - e^{i\mathbf{k}'\cdot(\mathbf{R}+\mathbf{a}_2)} - e^{i\mathbf{k}'\cdot(\mathbf{R}+\mathbf{a}_1-\mathbf{a}_2)}\right) + h.c. \\ =& is\frac{\Delta_{SO}}{3\sqrt{3}}\sum_{\mathbf{k}} c^\dagger_{\mathbf{k}A} c_{\mathbf{k}A}\left(-e^{i\mathbf{k}\cdot\mathbf{a}_1} + e^{i\mathbf{k}\cdot\mathbf{a}_2} + e^{i\mathbf{k}\cdot(\mathbf{a}_1-\mathbf{a}_2)}\right) \\ & + c^\dagger_{\mathbf{k}B} c_{\mathbf{k}B}\left(e^{i\mathbf{k}\cdot\mathbf{a}_1} - e^{i\mathbf{k}\cdot\mathbf{a}_2} - e^{i\mathbf{k}\cdot(\mathbf{a}_1-\mathbf{a}_2)}\right) + h.c.. \end{aligned} \tag{1.24}$$

In the more compact spinor form

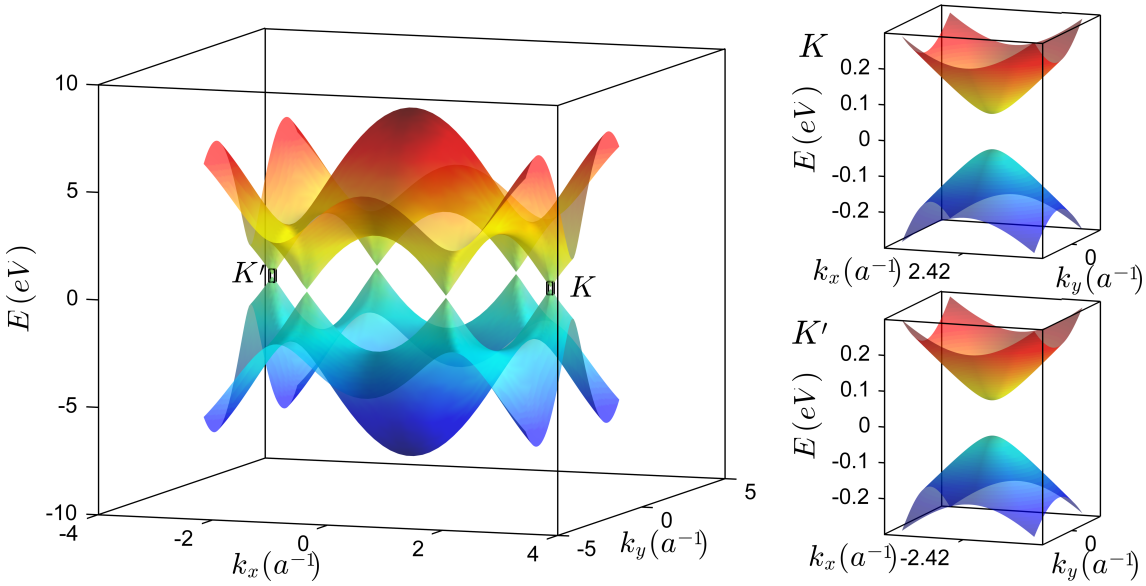

Figure 1.4: Energy dispersion of graphene with a staggered potential included. The conduction and valence bands are nearest to each other at the two distinct valleys, however they do not touch, as shown in the two insets.

$$H_{SO} = s\Delta_{SO}\sum_{\mathbf{k}}\left[c^{\dagger}_{\mathbf{k}A}, c^{\dagger}_{\mathbf{k}B}\right]\begin{bmatrix}\chi(\mathbf{k}) & 0\\ 0 & -\chi(\mathbf{k})\end{bmatrix}\begin{bmatrix}c_{\mathbf{k}A}\\ c_{\mathbf{k}B}\end{bmatrix}, \tag{1.25}$$

where

$$\chi(\mathbf{k}) = \frac{2}{3\sqrt{3}}\left[\sin(\mathbf{k}\cdot\mathbf{a}_1) - \sin(\mathbf{k}\cdot\mathbf{a}_2) - \sin(\mathbf{k}\cdot(\mathbf{a}_1-\mathbf{a}_2))\right]. \tag{1.26}$$

Adding now the kinetic and staggered potential terms, the full tight-binding band structure is given by

$$\epsilon(\mathbf{k}) = \pm\sqrt{|\gamma(\mathbf{k})|^2 + (s\Delta_{SO}\chi(\mathbf{k}) + \Delta)^2}. \tag{1.27}$$

Having in mind that $\chi(\mathbf{K}_\tau) = \tau$, the low-energy expansion around K and K' provides us with the effective continuum picture [9, 26]

$$H = \hbar v_F\left(\tau k_x\sigma_x + k_y\sigma_y\right) + s\tau\Delta_{SO}\sigma_z + \Delta\sigma_z. \tag{1.28}$$

Apart from the spin-valley dependence, it is clear that the effective term for the spin-orbit interaction takes the form of a staggered potential. However, while SOC assumes the form given in Eq. (1.28) only for low energies in momentum space, the staggered potential term remains unchanged compared to its real space representa-

tion. Also, note that the staggered potential breaks inversion symmetry, while the SOC term does not. They both also preserve time-reversal symmetry.

Setting $\Delta_{SO} = 0$ at the moment, we depict the band structure given by Eq. (1.27) for $\Delta = 0.05$ eV in Fig. 1.4. Note that the majority of the dispersion remains similar to the intrinsic band structure, displayed in Fig. 1.2. However, as shown in the insets, a difference arises near the two valleys; namely a band gap appears, indicating a transition to an insulating phase. This property reflects on the dispersion of low-energy quasiparticles near the two valleys

$$E = \pm\sqrt{\mathbf{p}^2 v_F^2 + \Delta^2}. \tag{1.29}$$

This is the energy-momentum relation obeyed by a massive relativistic particle, in which the Fermi velocity again plays the role of the speed of light, while Δ mimics the rest energy. Therefore a stationary quasiparticle sits at Δ (bottom of the conduction band), while its antiparticle counterpart is to be found at $-\Delta$ (top of the valence band), meaning that the band gap is given by 2Δ. In the case of hBN for example, the staggered potential leads to the opening of a 5.97 eV large band gap [28]. However, the band structure for $\Delta = 0$ and $\Delta_{SO} = 0.05$ eV is practically indistinguishable from the one depicted in Fig. 1.4, while the low energy quasiparticles have virtually identical dispersion relation

$$E = \pm\sqrt{\mathbf{p}^2 v_F^2 + \Delta_{SO}^2}. \tag{1.30}$$

So the question arises, what, if any, are the differences between the two cases? The key to answering this question lies in acknowledging the fact that quantum mechanics provides us not only with eigenvalues, but also with eigenvectors. And, not only are the eigenvectors in the two cases different, they are different throughout the entire Brillouin zone; so much so, that a topological invariant, denoted as Z_2 is used to distinguish the aforementioned insulators. The number in the index indicates that there are two such insulator classes; ordinary insulators with $Z_2 = 0$, and the so-called topological insulators with $Z_2 = 1$.

It must be said that topological insulators are not a new occurrence. The most famous example is the quantum Hall effect (QHE - the integer version in particular), which takes place in sufficiently cold 2D electron gases (2DEG) exposed to strong magnetic fields. The effect is easily interpreted semiclassically; magnetic field enforces cyclotron motion, which in turn leads to the formation of the Landau level

(LL) spectrum for closed orbits in the bulk. Because of this quantization, electrons can only occupy discrete energy states with vanishing group velocity, making the bulk insulating. On the sample boundary, however, the cyclotron trajectories do not close in on themselves; instead the electrons are backreflected every time they encounter the edge, thus effectively drifting along them in a motion referred to as skipping orbits. Therefore, not only are they able to carry current, but the states on opposite edges also form physically separate channels of flow in opposite directions, enabling dissipationless conduction. As a result, the Hall conductance can take only discrete values, given as n multiples of the quantum of conductance e^2/h, which itself is the conductance of a single transmission channel spared of any scattering.

Besides measuring the number of channels contributing to transport (the filling fraction), n also turns out to be a topological invariant called the Chern number. This comes out as a result of a more rigorous, and in-depth quantum treatment. The formal procedure bears an analogy to the process of characterizing closed surfaces in differential geometry through a topological attribute. As Gauss-Bonnet theorem shows, the integral of the Gaussian curvature on a closed surface equals to an even integer multiple of 2π; this integer is the topological invariant known as the Euler characteristic. In a similar fashion, the Chern index of an energy band is obtained as

$$C_n = \frac{1}{2\pi} \oint \Omega_n \left(\mathbf{k}\right), \tag{1.31}$$

where $\Omega_n \left(\mathbf{k}\right) = \nabla_{\mathbf{k}} \times \langle u_{n\mathbf{k}} | \nabla_{\mathbf{k}} | u_{n\mathbf{k}} \rangle$ and $|u_{n\mathbf{k}}\rangle$ are the so-called Berry curvature and the periodic part of the Bloch wave function, respectively. The Chern number distinguishes different QHE states.

The phenomenal transport performance of the QHE regime, however did not become of significant practical importance. The reason is that the effect appears only when the 2DEG is subject to strong magnetic field, something not achievable easily outside the lab (or even inside the lab). The major breakthrough of Kane and Mele in 2005 was the realization that a nontrivial insulating phase can arise even in the absence of magnetic fields, thus paving the way for time-reversal invariant topological insulators. Their Hamiltonian is a generalization of the Haldane model, which for spinless electrons provides quantum Hall effect strictly from the band structure, and in the absence of a (net) magnetic field and Landau levels [29]. Combining two opposite copies of this model for each spin gives rise to the so-called quantum spin

Hall (QSH) effect, that Kane and Mele showed appears in honeycomb lattices with sufficiently strong spin-orbit interaction. Roughly speaking, spin-orbit interaction plays the role of an effective magnetic field, with opposite directions for opposite spins, hence creating two copies of the Hall effect. As a result, on the edges of the sample the two spins are counter-propagating. It follows that the two spin sectors have opposite Chern numbers, but the entire system has a vanishing Chern number (no Hall effect), so the important index instead becomes the Z_2 number. Another way to interpret the appearance of edge states in the QSH phase is through the bulk-edge correspondence; since the material in the QSH phase and the vacuum surrounding it are topologically distinct insulators, the band gap must close and reopen between them for the topological invariant to change, resulting in gapless metallic edge states.

1.5 Magnetic field

We now return to the discussion of intrinsic graphene. One of the most remarkable manifestations of the ultrarelativistic nature of graphenes quasiparticles is the exotic Landau level spectrum. In fact, this spectrum provided the first definitive proofs of the monolayer structure of exfoliated samples through the QHE. We therefore study the impact of a magnetic field on an infinite graphene sample here (the Zeeman energy is disregarded).

The influence of the magnetic field on the Hamiltonian is captured through the minimal coupling scheme (a replacement rule $\mathbf{p} \to \mathbf{\Pi}$) so that

$$H = v_F \left(\tau \Pi_x \sigma_x + \Pi_y \sigma_y\right), \tag{1.32}$$

where $\mathbf{\Pi} = \mathbf{p} + e\mathbf{A}$ $(e > 0)$ is the kinematical or mechanical momentum, and $\mathbf{A}$ is the magnetic vector potential. The magnetic field is associated with the curl of the vector potential, $\mathbf{B} = \nabla \times \mathbf{A}$. Different functional forms of the vector potential, called gauges, can give the same magnetic field. While the canonical momentum $\mathbf{p}$ is gauge dependent, the kinematical momentum $\mathbf{\Pi}$ is gauge invariant, since its expectation value is proportional to a measurable property - the electron velocity. Since we are interested in a magnetic field perpendicular to the graphene plane, $\mathbf{B} = B\mathbf{e}_z$, we will employ the so-called Landau gauge $\mathbf{A} = B\,(0, x, 0)$. The resulting Hamiltonian is translationally invariant along the y direction, rendering k_y a good

quantum number

$$\Psi = e^{ik_y y}\psi(x). \tag{1.33}$$

Replacing this into the Dirac-Weyl Hamiltonian one obtains the coupled equations

$$\hbar v_F \begin{pmatrix} 0 & \pi \\ \pi^\dagger & 0 \end{pmatrix} \psi(x) = E\psi(x), \tag{1.34}$$

where $\pi = -i\tau\partial_x - ik_y - ix/l_B^2$. We transform the system of two coupled first order differential equations into two independent second order differential equations through $H^2\psi = E^2\psi$

$$\left[-\hbar^2\partial_x^2 + \frac{\hbar^2}{l_B^4}\left(k_y l_B^2 + x\right)^2\right]\psi_{A/B} = \left(\frac{E^2}{v_F^2} \mp \frac{\tau\hbar^2}{l_B^2}\right)\psi_{A/B}. \tag{1.35}$$

Compare for instance the equation for the B sublattice in the K valley, with the equation of the quantum harmonic oscillator (shifted by $x_0 = k_y l_B^2$, and rescaled by $2m$)

$$\left[p_x^2 + m^2\omega^2\left(x_0 + x\right)^2\right]\psi = 2m\epsilon\psi, \tag{1.36}$$

where m is the mass of the electron and ω is the angular frequency. By direct matching, we are able to ascertain that $m\omega = \hbar/l_B^2$. Substituting this in the standard n-th eigenstate of the quantum harmonic oscillator, shifted by x_0 we obtain

$$\langle x|n\rangle = \frac{\pi^{-1/4}}{\sqrt{2^n n!}} e^{-\frac{\left(x+k_y l_B^2\right)^2}{2l_B^2}} H_n\left(\frac{x}{l_B} + k_y l_B\right). \tag{1.37}$$

Solving for the eigenfunctions we obtain

$$|\psi_B\rangle = |n\rangle. \tag{1.38}$$

Going back to the coupled equations, and employing $H_n'(x) = 2nH_{n-1}(x)$ one can obtain the other spinor

$$|\psi_A\rangle = -i\alpha|n-1\rangle, \tag{1.39}$$

where $\alpha = +1$ (-1) in the conduction (valence) band. After performing similar calculations for the K' valley, the total spinor for both valleys can be written as

$$|\psi_n\rangle = e^{ik_y y} \begin{pmatrix} -i\alpha|n - \frac{\tau}{2} - \frac{1}{2}\rangle \\ |n + \frac{\tau}{2} - \frac{1}{2}\rangle \end{pmatrix}. \tag{1.40}$$

On the other hand, having in mind that $\epsilon = \hbar\omega\,(n + 1/2)$, the Landau levels in graphene are given as

$$E_n = \alpha v_F \sqrt{2n\hbar e B}, \tag{1.41}$$

with $n \geq 1$. Besides these solutions, a peculiar zeroth LL is a valid solution with energy $E_0 = 0$. The corresponding eigenfunction is derived from Eq. (1.35), and reads

$$|\psi_0\rangle = e^{ik_y y} \begin{pmatrix} -\tau/2 + 1/2 \\ \tau/2 + 1/2 \end{pmatrix} |0\rangle. \tag{1.42}$$

Note that the zeroth LLs are fully localized on only one sublattice, a property referred to as pseudospin polarization. There are two striking features of the magnetic spectrum of massless, Dirac-Weyl fermions as compared to the one corresponding to massive and nonrelativistic 2DEG particles. On one hand, the level energies depend on the square root of the magnetic field and the level index in the former case, whereas they disperse linearly in the latter case. Moreover, apart from the usual spin-degeneracy, each level also appears in both valleys, making the total degeneracy of a given level four-fold. On the other hand, ultrarelativistic particles form a Landau level at exactly zero energy (i.e. at the Dirac point). Intriguingly, this level is shared equally by the conduction and the valence band because of the inherent electron-hole symmetry of graphene, i.e. two of the levels have an electron-like character, while the other two have a hole-like character.

Consider what that means for the QHE measurements, given that an occupied electron (hole) LL state contributes e^2/h ($-e^2/h$) to the Hall conductance. When the Fermi energy lies between $n = 0$ and $n = 1$ levels, the zeroth LL is completely occupied, providing $2e^2/h$ of conductance, due to the spin degeneracy. Each higher LL occupied by electrons participates with $4e^2/h$ of conductance, due to full spin and valley degeneracy. Likewise, when the Fermi energy is between $n = -1$ and $n = 0$ levels, electron states are completely empty, however the zeroth LL is fully occupied by holes contributing with $-2e^2/h$ (again due to spin), with each new hole level contributing with $-4e^2/h$ of conductance. Finally, this all leads to the

anomalous Hall conductance plateaus, expressed as

$$\sigma_{xy} = \pm \frac{2e^2}{h} (2n + 1) , \tag{1.43}$$

for $n \geq 0$, which were experimentally confirmed in Refs. [16, 17], thus paving the way for the explosion of scientific exploration of graphene. It is also worth mentioning that transport signatures of the QHE in graphene can also be seen at room temperatures [30].

Chapter 2

Theoretical models and graphene nanoribbons

2.1 Introduction

In the previous chapter, we investigated the case of infinite honeycomb lattices using an analytical approach. In this chapter, we will do the opposite by applying the numerical techniques and procedures that we will introduce in order to find more about the fundamental properties of graphene nanostructures. In particular we will present the nonequilibrium Green function (NEGF) formalism for studying quantum transport for nanoscale devices [31–33], as well as the Hubbard method for predicting the appearance of spontaneous magnetic ordering due to the electron-electron interaction. Furthermore, we will employ the tight binding method for extracting the band structure for a particular type of one-dimensional graphene structures, called nanoribbons.

2.2 Nonequilibrium Green function method

The numerical transport formalism that is NEGF starts with three basic building blocks: the left lead, the device and the right lead. The leads are assumed to be translationally invariant and connected to electron reservoirs at the far ends. Given that NEGF operates in the quantum domain, all of the blocks are described by a corresponding Hamiltonian, written in a matrix form in the tight binding language. Therefore, NEGF explicitly incorporates the atomic structure into the calculations of the conductance, through the probability amplitudes for transition between different

orbitals that are the matrix elements.

The quantum nature of transport that NEGF captures, differs substantially from the Ohmic point of view. For instance, enlarging the length of the channel (resistor), would always bring about the increase in the resistance of the device in which transport is diffusive. On the other hand, for the devices in which the decoherence effects are minimized (by fabricating very small structures for example), the underlying quantum nature can be manifested and a resistance decrease can occur. Such a counterintuitive phenomena comes about from the interference of the electron waves; a feature captured only by the complex numbers present in the Hamiltonians. The NEGF is a robust and powerful formalism, easy to implement numerically due to its straightforward approach. However, this also means that some of the underlying physics remains obscure. In fact, a deep and detailed theoretical understanding of the obtained results is often missing. Therefore, it is always helpful to supplement these sorts of calculations with some analytical, usually effective low-energy theories, which could provide the essential details for interpreting the obtained results.

The Green's function of a system is given by

$$G = (EI - H)^{-1}, \tag{2.1}$$

where H is the Hamiltonian of the entire structure. Here it is implicitly assumed that the energy is shifted infinitesimally along the imaginary axis, i.e. $E \to (E + i\eta)$. This is done so as to enforce the computation of a retarded Green's function, while the advanced one can obtained by simply taking the Hermitian conjugate [33]. In the case of a system consisting of a device attached to a couple of leads the tight binding Hamiltonian can be written as

$$H = \begin{bmatrix} H_L & H_{LD} & 0 \\ H_{LD}^{\dagger} & H_D & H_{RD}^{\dagger} \\ 0 & H_{RD} & H_R \end{bmatrix}. \tag{2.2}$$

The only finite matrix here is the device Hamiltonian H_D, while all other matrices are infinite in size. H_L describes the hopping in the left lead, H_R describes the hopping in the right lead, H_{LD} and H_{RD} describe the hopping from the device to the left lead, and from the device to the right lead respectively, while their Hermitian adjoints describe the hopping in the reverse direction.

The corresponding Green function is likewise represented via submatrix blocks

$$G = \begin{bmatrix} G_L & G_{LD} & G_{LR} \\ G_{DL} & G_D & G_{DR} \\ G_{RL} & G_{RD} & G_R \end{bmatrix}. \tag{2.3}$$

Having in mind the definition of the Green function, Eq. (2.1), one can arrive at the following set of equations

$$\begin{aligned} (E - H_L)\, G_{LD} + H_{LD} G_D &= 0, \\ H_{LD}^{\dagger} G_{LD} + (E - H_D)\, G_D + H_{DR} G_{RD} &= I, \\ H_{DR}^{\dagger} G_D + (E - H_R)\, G_{RD} &= 0. \end{aligned} \tag{2.4}$$

After some manipulation one obtains

$$G_D = \left(E - H_D - \Sigma^L - \Sigma^R\right)^{-1}, \tag{2.5}$$

where $\Sigma^L = H_{LD}^{\dagger} g_L H_{LD}$ and $\Sigma^R = H_{RD}^{\dagger} g_R H_{RD}$ are the effective self-energy terms appearing in the Green function of the device due to the semi-infinite left and right leads, and $g_{L/R} = \left(E - H_{L/R}\right)^{-1}$ are their respective Green functions [34]. The self-energy matrices are not Hermitian, which reflects the fact that stationary states are absent in the device connected to the leads. This is analogous to the case when the complex energy of a particle results in a finite life time - there is a nonzero rate of electrons escaping from the device. The entire coupling between the device and the leads is contained in the self-energy matrices. A beneficial trait of the self energy matrices is that they are finite, thanks to the fact that the semi-infinite leads connect via hopping elements only to the surface sites in the device. Therefore it can be said that in this procedure the leads are integrated out of the problem, since we are left with the finite-size Green function of the device itself. In order to obtain these functions we employ the scheme laid out in Ref. [35]. It is important to point out that incorporating the influence of the infinite leads through the finite self-energy matrices is exact, although it may not appear so.

Once these and the broadening matrices $\Gamma_{L/R} = i\left(\Sigma_{L/R} - \Sigma_{L/R}^{\dagger}\right)$, are obtained, the transmission probability through the structure can be calculated via the Fisher-Lee relation [36]

$$T = Tr\left(\Gamma_L G_D^{\dagger} \Gamma_R G_D\right). \tag{2.6}$$

Note that this equation holds for infinitesimal bias ($V \to 0$), and the conductance is then given by

$$G = \frac{e^2}{h}T. \tag{2.7}$$

This is the Landauer-Büttiker expression, which treats the devise as a scattering region, in which the waves from different leads are incident or reflected. Therefore, in quantum transport the conductance is fundamentally related to the transmission coefficient of the incoming waves, with the proportionality constant being the quantum of conductance. Execution of the exposed algorithm can become computationally intractable, since the process involves matrix inversion which is numerically troublesome. An additional procedure is then taken, known as the recursive algorithm [37].

Having introduced the NEGF method, one could wonder, how justified is it to employ it in studying graphene nanodevices? As it turns out, owing to exceptional crystal quality, electrons in graphene have phase coherence lengths of several micrometers [38]. This puts nanoscale graphene structures well into the ballistic quantum regime of transport, warranting the NEGF approach.

2.3 Graphene nanoribbons

Graphene nanoribbons are one-dimensional quantum wires, in which a finite width leads to quantization of transverse modes, with freely propagating longitudinal channels. The two most important types of graphene nanoribbons are classified according to the orientation of their edges, which can be either zigzag or armchair. These are depicted in Figs. 2.1(a) and (b), respectively, alongside the corresponding unit cells. Note that in contrast to armchair nanoribbons, edges of a zigzag nanoribbon are composed out of atoms of only one sublattice. The edge atoms are considered to be the ones which have dangling bonds, i.e. that are connected only with 2 carbon atoms. The dangling bonds are implicitly assumed to be saturated by hydrogen, thus providing no contribution to the energy dispersion. The two methods of categorizing the width of the nanoribbons is presented as well. In the case of zigzag structures one counts the number of zigzag lines, while one counts the number of atomic dimer pairs along the width in the case of armchair nanoribbons ($N_{ZG} = 8$ and $N_{AC} = 14$ for the particular structures presented in Fig. 2.1).

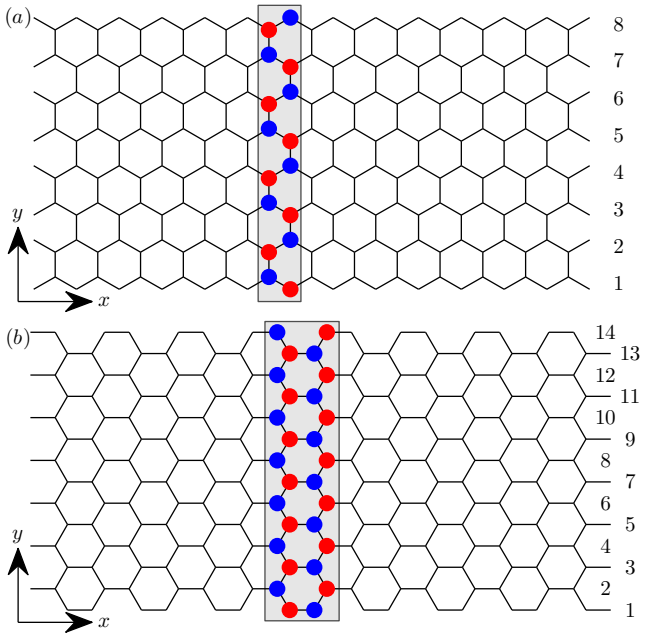

Figure 2.1: Graphene nanoribbons, created by translation of the unit cells depicted in gray along the x direction. (a) zigzag and (b) armchair nanoribbons. The numeration system used to denote the width of the structures is displayed on the right-hand side; in particular $N_{ZG} = 8$ and $N_{AC} = 14$.

In order to obtain the corresponding band structures, one can again follow the recipe used in Chapter 1. However, the structures are periodic only along one direction (x), while they enforce quantum confinement along the other direction (y). Therefore the band structure is not represented by surfaces, but by lines depending on the Bloch momentum k_x. The number of bands, as in the case of plane graphene, is equal to the number of atoms in the unit cell.

In Figs. 2.2(a), (b) and (c) we depict the density of states, the band structure and the conductance, respectively, for a zigzag nanoribbon with $N_{ZG} = 10$, while the corresponding diagrams for $N_{ZG} = 40$ are shown in Fig. 2.3. The conductance is calculated using the NEGF approach introduced in the previous section, and the crystal momentum k_x is normalized by the lattice vector of the nanoribbon (in this case $\sqrt{3}a$). The density of states is obtained as

$$D(E) = \frac{1}{2\pi} \sum_n \int_{BZ} \delta\left(E - E_n\left(k_x\right)\right) dk_x \tag{2.8}$$

$$= \frac{1}{2\pi} \sum_n \int_{BZ} \sum_i \frac{\delta\left(k_x - k_{xi}\right)}{\left|E_n'\left(k_x\right)\right|} dk_x, \tag{2.9}$$

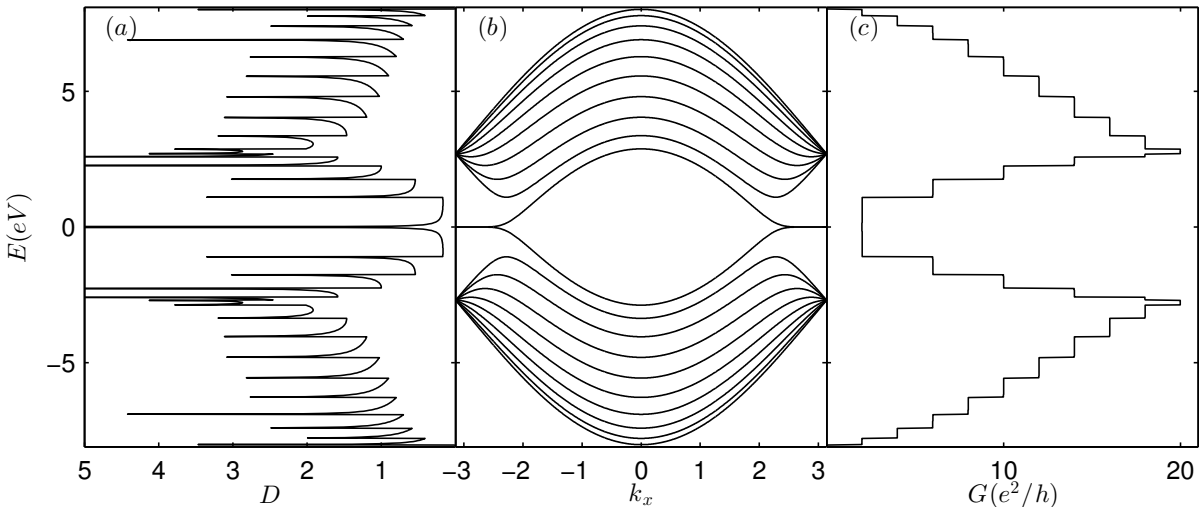

Figure 2.2: (a) Density of states, (b) band structure and (c) conductance for a $N_{ZG} = 10$ nanoribbon.

where $E_n(k_x)$ is the $n-$th band energy dispersion, and k_{xi} are the roots of the function $E - E_n(k_x)$. Alternatively, the NEGF formalism also yields the density of states through the Green function

$$D(E) = \frac{i}{2\pi}\mathrm{Tr}\left(G_D - G_D^\dagger\right) \tag{2.10}$$

which coincides with the one calculated from the band dispersions.

Therefore, only those bands intersecting a particular energy contribute to the density of states at that energy. Furthermore, this contribution is inversely proportional to the steepness of the bands at the intersection points. This in turn means that flat bands provide a major boost to the density of states, as can be witnessed in Figs. 2.2 and 2.3. In particular note that there are flat bands at the neutrality point, appearing roughly within $2\pi/3 \leq |k_x| \leq \pi$, which is a general trait of zigzag nanoribbons. Therefore, not only are they metallic, they also exhibit a large density of states at the Fermi energy. These are the so-called zero-energy or edge modes of the zigzag nanoribbons, and they are stationary at the edges since their group velocity is vanishing [39]. This is also manifested in vanishing effective hopping along the longitudinal (x) direction in the momentum-space Hamiltonian. In fact, at $k_x = \pi$ the longitudinal hopping is zero, and only the transverse hopping exists ensuring connection within the atomic dimers. In this case the edge states are completely localized on the edge atoms, which do not have a dimmer pair and are effectively

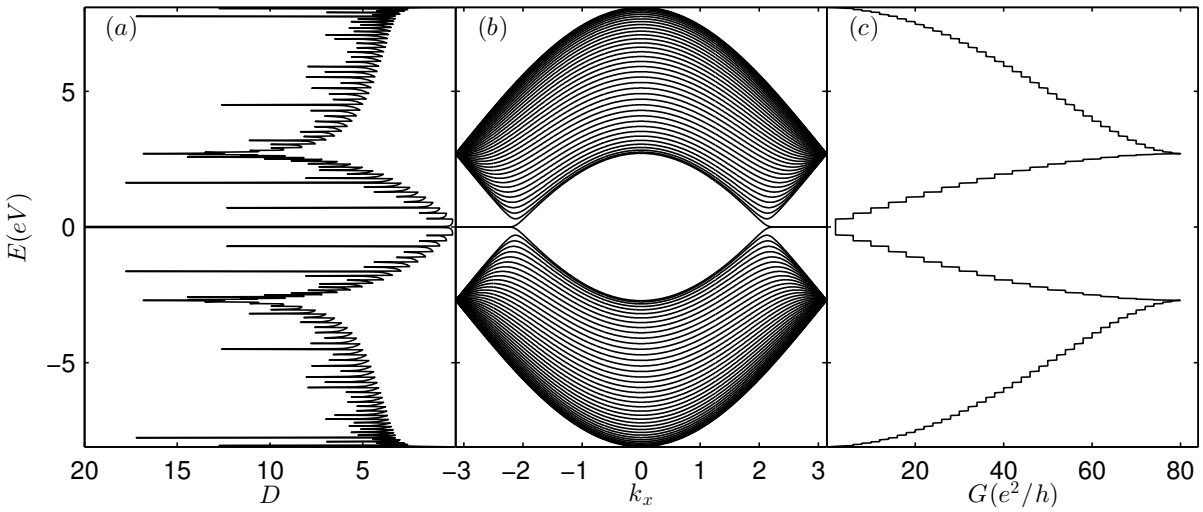

Figure 2.3: (a) Density of states, (b) band structure and (c) conductance for a $N_{ZG} = 40$ nanoribbon.

isolated, making them incredibly sensitive to local perturbations. This property will turn out to be quite important, and will be studied in more detail, both in the rest of this, as well as in the subsequent chapters.

Additionally, note that zigzag nanoribbons preserve the two-valley structure of bulk graphene. This comes about as a consequence of the transverse quantization, which being along the y direction, "samples" both valleys of the band structure of graphene (shown in Fig. 1.2) along discreet k_y values. In other words the bands can be obtained by projecting cuts of the dispersion (1.14) along particular values of k_y, and for the range of ($\sqrt{3}a$ normalized) longitudinal momentum $-\pi \leq k_x < \pi$. This range is large enough to contain both valleys, albeit k_y quantization criteria always misses the exact K and K' points. The line closest to these points represents the bottom (top) of the conduction (valence) band. Having this in mind, we can deduce that the valley near $k_x = -2\pi/3$ ($\pm$ a multiple of 2π) is a projection of the K valley onto the $E - k_x$ plane. Zone-folding does not capture the flat, gapless part of this band, since such a feature is not present in bulk graphene.

The two-valley structure reflects on the conductances, shown in panel (c). Since the structure is translationally invariant, all bands provide a quantum of conductance, which, given the twofold spin degeneracy and the aforementioned valley degree of freedom, for low energies means that G jumps in steps of $4e^2/h$.

On the other hand, armchair nanoribbons reveal different behavior. In Figs. 2.4 and 2.5 we again show D, $E(k_x)$ and G, but for armchair nanoribbons of widths $N_{AC} = 10$ and $N_{AC} = 40$, respectively. Unlike for zigzag nanoribbons, zone-folding

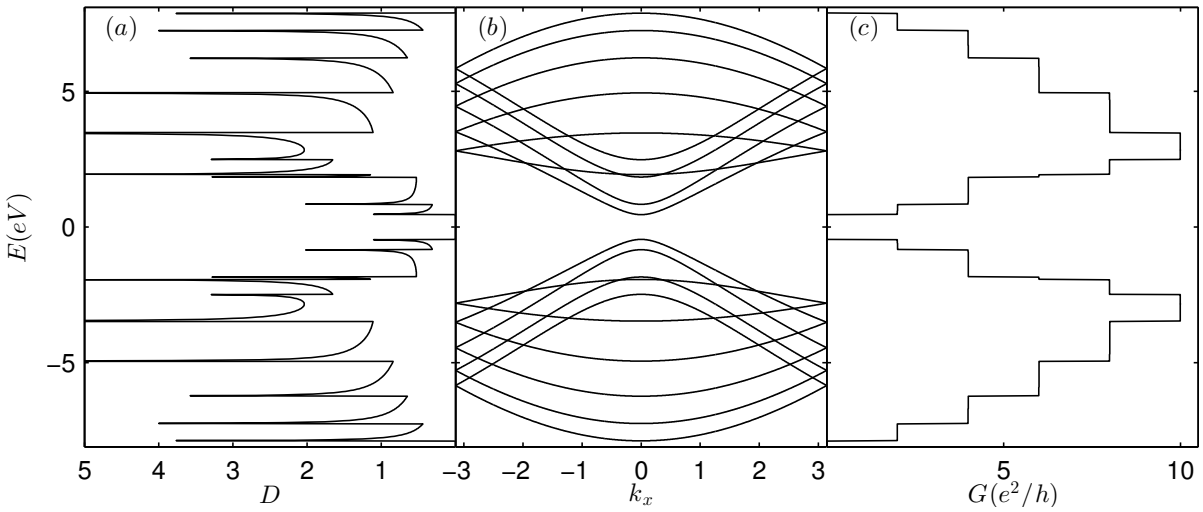

Figure 2.4: (a) Density of states, (b) band structure and (c) conductance for a $N_{AC} = 10$ nanoribbon.

captures the entire spectrum of armchair nanoribbons. It can be seen that they are insulating, with a vanishing density of states at the Dirac point. However, armchair nanoribbons with $N_{AC} + 1$ divisible by three are metallic; otherwise their band gap is inversely proportional to the width [39]. The zero-energy edge states are actually a generally robust property of all edge orientations, however their density varies from zero in armchair, to a maximum value in zigzag nanoribbons [40]. Armchair nanoribbons also do not feature a valley degree of freedom like their zigzag counterparts; in fact the two valleys get mixed. The lack of valley flavor is reflected in the conductances of the two cases. In particular, even though there are equal number of energy bands for $N_{ZG} = 10$ and $N_{AC} = 10$ nanoribbons, the conductance in the former case is double that of the latter case.

2.3.1 Staggered potential and spin-orbit coupling

In Figs. 2.6(a) and (b) we examine the energy dispersion of zigzag graphene nanoribbons in the presence of the parameters Δ and Δ_{SO} introduced in Chapter 1, respectively. While in bulk graphene both terms lead to an insulating state, indistinguishable from the band structure point of view, the situation here is drastically different. In particular, only Δ preserves the band gap, while a pair of linearly dispersing bands crosses what used to be the band gap in bulk for Δ_{SO}, rendering the nanoribbon conducting. Obviously, the topological nature of the insulating state dictates this phenomenon; the pair of linearly dispersing bands originates from the

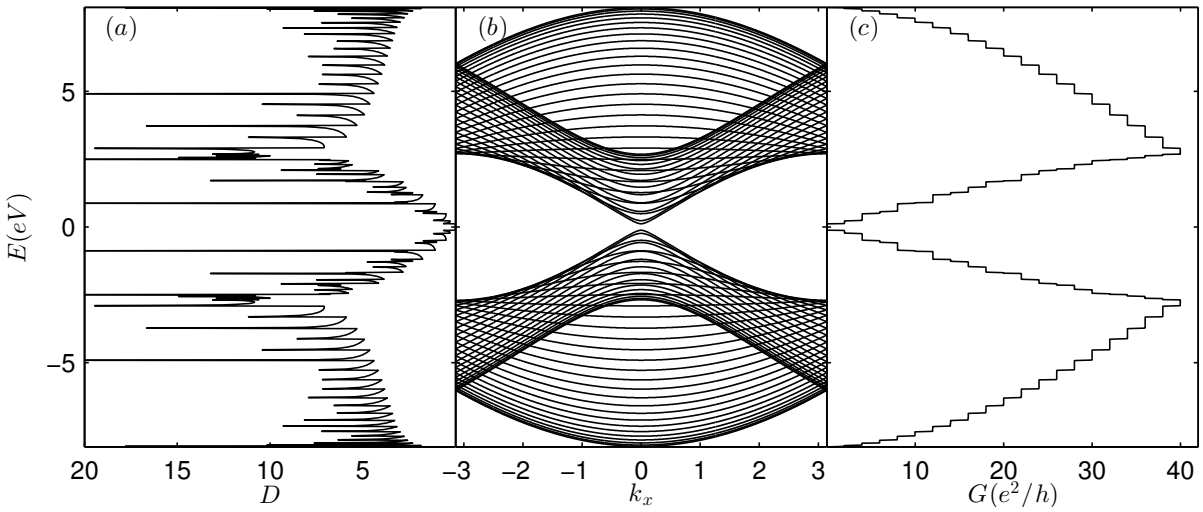

Figure 2.5: (a) Density of states, (b) band structure and (c) conductance for a $N_{AC} = 40$ nanoribbon.

flat bands of ordinary zigzag graphene nanoribbons (Fig. 2.2) due to the aforementioned bulk-edge correspondence.

The ribbon with SOC is topologically different from the surrounding vacuum, which is considered to be a trivial insulator with an infinite band gap. This difference is overcome only after smoothly closing the band gap, which occurs near the edges and produces the chiral states. The left (upper panel) and right (lower panel) moving chiral states are shown in real space next to Fig. 2.6(b), with spin up (down) denoted by red (blue) filled circles, and they correspond to a particular Fermi energy depicted in Fig. 2.6(b). Spin up (down) propagates to the right mainly along the top (bottom) edge, while the opposite is true for the left-movers. In other words it is effectively as if there are two opposite copies of the QHE for the opposite spins.

Note that we have chosen a quite high Fermi energy, for which the chiral states penetrate deeply toward the opposite edge. The closer the Fermi energy to the neutrality point, the more localized the states get. This prevents any overlap between the left and right moving channels located on the opposite sides of the ribbon, leading to the prevention of backscattering. This in turn results in disipationless conductance, and gives rise to the quantum spin Hall effect. Note that the effect is undermined in the presence of time-reversal breaking perturbations, such as localized magnetic defects. In this case, spins can get flipped, and the counter-propagating modes on the same edge can get coupled.

In the particular case of zigzag nanoribbons, the penetration depth is proportional to the SOC [41]. Turning on the SOC from zero is an adiabatic process, during

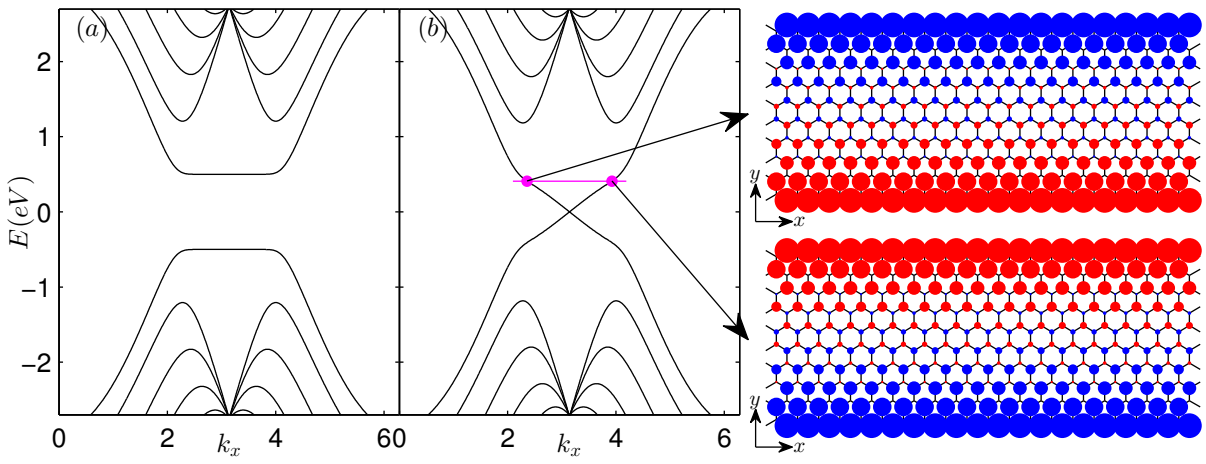

Figure 2.6: Band structure of a $N_{ZG} = 10$ nanoribbon with nonzero (a) $\Delta = 0.5$ eV, and (b) $\Delta_{SO} = 0.5$ eV. The panels on the right show the real space weight of left (top) and right (bottom) moving chiral states marked in (b). Spin up is shown in red and spin down in blue, while the marker area is proportional to the probability.

which the flat bands get progressively more tilted, and turned into topologically protected modes. However, in semiconducting armchair nanoribbons such an adiabatic process can not discontinuously close the gap. This is manifested through the penetration depth which in this case is inversely proportional to the SOC. Hence, for small SOC, the zero energy modes on each edge hybridize with each other leading to bonding and anti-bonding bands, which explains the enduring band gap, a feature often referred to as the finite size effect. Therefore, the quantization of conductance in armchair nanoribbons appears for higher SOC than in zigzag nanoribbons.

Incidentally, one realization of a quantum valley Hall effect (QVHE) can occur in systems with inversion symmetry broken by a staggered potential. The lowest conduction band in Fig. 2.6(a) inherits the localization properties of the state it is smoothly deformed from, namely those of the flat gapless zigzag bands. Again, the state at $k_x = \pi$ is the most extreme with all of its weight on the outer atoms, while the surrounding states display an increasing penetration depth. Therefore, the application of the potential at the edge will shift the flat bottom of the conduction band to a varying degree, thus creating dispersing bands. The energy at $k_x = \pi$ gets bent the most, while outside the region $2\pi/3 \leq k_x \leq 4\pi/3$ extended states scarcely feel the potential, so that there the band remains firmly in place. A sufficiently strong potential applied to the outermost atoms can lower the band at $k_x = \pi$ into the valence band. At this point the band represents a left-moving channel in one valley and a right-moving channel in the other valley. On the other hand, in the

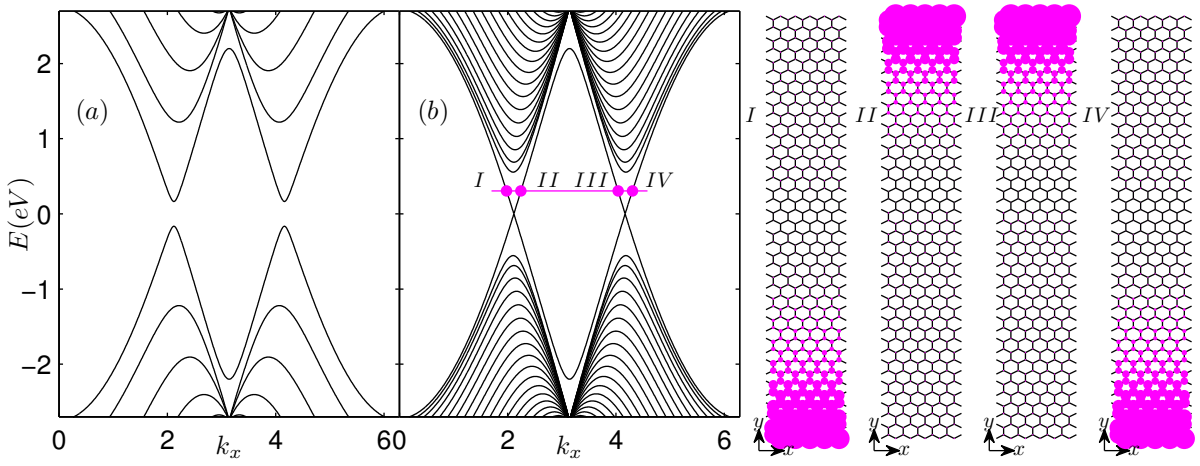

Figure 2.7: Band structure of a (a) $N_{ZG} = 10$ and (b) $N_{ZG} = 40$ nanoribbon with $\Delta = 0.5$ eV and a potential applied to the outermost atoms of the ribbon. The panels on the right show the real space weight of corresponding states depicted in (b). The markers are colored purple since they correspond to both spins, while the marker area is proportional to the probability.

valence band the situation is similar, albeit with localization on the opposite edge. Hence disipationless valley current becomes possible in theory [42].

The situation is depicted in Fig. 2.7. In panel (a) the effect gets spoiled since for a narrow nanoribbon (in this particular case $N_{ZG} = 10$) the states on opposite edges overlap, resulting in hybridization and preservation of a gap. For wider nanoribbons (panel (b)), this is not the case, and the low energy spectrum consists of Dirac cones for the two valleys. Counter-propagating states on a given edge belong to opposite valleys, as shown in panels I, II, II and IV. Note that besides the spin-degenerate band structure, in this scenario there are no spin-distinguishing real space features either, as opposed to the QSHE case.

2.4 Electron-electron interaction and the Hubbard model

The most simple way of incorporating the influence of electron-electron interaction within the tight-binding models is through the Hubbard model

$$H = -t \sum_{\langle ij \rangle \beta} c^{\dagger}_{i\beta} c_{j\beta} + U \sum_{i} n_{i\uparrow} n_{i\downarrow}, \tag{2.11}$$

where the first sum is the standard kinetic part of itinerant electrons describing jumps between sites on a lattice. The second part is the Hubbard term which describes the potential energy cost arising due to the Coulomb repulsion energy of two electrons with opposite spins orbiting the same atom. The operator $n_{i\beta} = c^\dagger_{i\beta} c_{i\beta}$ is the number operator of spin β on site i. In the large U limit, the energetic penalty of such a repulsion is high, which signals the on-set of strongly correlated physics. The ground state is forced to avoid this expense by minimizing the double occupancy. Due to the competition between the kinetic and potential energy, at half-filling, when the number of electrons equals the number of lattice sites, it can be more favorable for the entire lattice to consist of singly occupied sites with non-itinerant electrons. In such a case a Mott insulator is formed, whose nature does not derive from the band structure, but rather from the interaction between the particles.

While the kinetic part of the Hamiltonian is quadratic in terms of the number of creation/annihilation operators, the Hubbard part is quartic, meaning it has four of them, a general feature of interaction terms. This has some serious implications regarding the applicability and solvability of the model. The quadratic Hamiltonians, that we have studied thus far, are easy to diagonalize. Such Hamiltonians can in general be expressed as $H = \sum_{ij} c^\dagger_i h_{ij} c_j$, with h_{ij} being the matrix elements of the Hermitian matrix h. As such, there will exist a unitary matrix U transforming h into diagonal form $H = \sum_i \epsilon_i a^\dagger_i a_i$, with the rotated bases given by $a_i = \sum_j U_{ij} c_j$, which is true for any single-particle problem.

In the case of many-body problems, to which the Hubbard model belongs, the Hamiltonian can also be solved by exact diagonalization, albeit in a much larger generalization of Hilbert space known as Fock space. The Fock space is a set of Hilbert spaces, each of which describes a given system with a different number of identical particles. The fact that the total electron number operator, $N = \sum_i n_{i\uparrow} + n_{i\downarrow}$, commutes with the Hubbard model is somewhat alleviating, since it reduces this space to the case of particular filling. To illustrate that this is still not enough to render the problem numerically tractable let us consider the case of a simple three-site model at half filling. In such a case the number of electrons equals the number of sites, $N = 3$, and the relevant space is spanned by vectors $\{|\downarrow,\downarrow,\downarrow\rangle, |\uparrow,\downarrow,\downarrow\rangle, |0,\uparrow\downarrow,\downarrow\rangle, |0,\downarrow,\uparrow\downarrow\rangle, \ldots, |\uparrow,\uparrow,\uparrow\rangle\}$. The size of this space is in general easily calculable and amounts to every possible rearrangement of N electrons on N sites

$$\sum_{n_\uparrow=0}^{N} \binom{N}{n_\uparrow}\binom{N}{N-n_\uparrow}, \tag{2.12}$$

which for $N = 3$ gives 20. Therefore, instead of diagonalizing a 3×3 matrix one is forced to diagonalize a 20×20 matrix. This quickly gets out of hand with increasing system size. Note that since there are no spin-flipping processes, $n_{i\beta}$ also commutes with the Hamiltonian, and one might further break down the problem into subspaces with definite $n_\uparrow$ and $n_\downarrow$, for which the problem is block diagonal. Still, this does not help resolve the issue in general, since the bottleneck subspace size for $n_\downarrow = n_\uparrow = N/2$ is given by $\binom{N}{N/2}^2$, which for $N = 30$ electrons comes to about $\approx 2.4 \times 10^{16}$.

Because of the computational obstacles in analyzing even the smallest systems people usually resort to the so-called mean field approximation (MFA). This approximation allows the transformation of the problem to a quadratic one at the expense of disregarding the quantum fluctuations, while still retaining some of the essential physics. The mean field approximation then allows the study of much larger system sizes, with the drawback of overestimating the stability of the magnetic order. Moreover, the lower the Coulomb repulsion U, the better the fit between exact diagonalization results and the MFA.

In order to make this transition one starts by expressing the number operators in Eq. (2.11), as an average plus the deviation from the average $n_{i\beta} = \langle n_{i\beta}\rangle + (n_{i\beta} - \langle n_{i\beta}\rangle)$, and then ignoring the product of the two deviations

$$H = -t\sum_{\langle ij\rangle\beta} c^\dagger_{i\beta}c_{j\beta} + U\sum_i \left(n_{i\uparrow}\langle n_{i\downarrow}\rangle + n_{i\downarrow}\langle n_{i\uparrow}\rangle - \langle n_{i\uparrow}\rangle\langle n_{i\downarrow}\rangle\right). \tag{2.13}$$

The quartic nature of the interaction is lost, while the resulting quadratic form captures only an interaction of one spin species with the average occupation of the other spin species at a given site. Besides the loss of fine details, one other drawback of this approach is that the problem now has to be solved self-consistently. The procedure begins with an assumed distribution of spins, expressed trough $\langle n_{i\beta}\rangle$. At each iteration the Hamiltonian is diagonalized, and until the change of average occupation is not sufficiently low the next iteration step is started. The method is suitable for analyzing periodic structures as well [39]. One again needs to perform the Fourier transformation of the basis, while the occupation is obtained after averaging over the entire Brillouin zone.

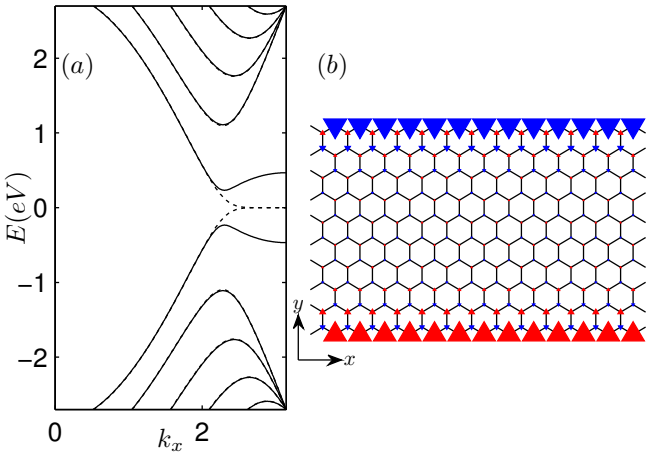

Figure 2.8: (a) Band structure of $N_{zg} = 10$ nanoribbon with (solid) and without (dashed) interactions. (b) Real space distribution of magnetic moments.

As it turns out, the large density of states at the Fermi energy in zigzag nanoribbons discussed previously leads to an instability once the electron-electron interaction is taken into account. This instability is avoided by transitioning into a broken symmetry state, with the most stable configuration being the antiferromagnetic one. In this phase, spins of opposite orientation get localized on opposite sublattices. In Fig. 2.8 we depict the band structure and the real-space distribution of the magnetic moments, $\langle n_{i\uparrow}\rangle - \langle n_{i\downarrow}\rangle$, for a $N_{ZG} = 10$ nanoribbon with $U = 1.2t$. The gapless band structure of the non-interacting model (dashed lines) is stabilized by the opening of an interaction-induced band gap (solid lines). On the other hand, the magnetic moments are predominantly localized near the edges, where the instability originated. The spin arrangement along the edges is ferromagnetic, since only a single sublattice is present there. Recent transport experiments seem to confirm the validity of the simple MF Hubbard model [43]. Moreover, the data is best fitted by a Coulomb repulsion parameter $U = 3.24$ eV, i.e., with $U = 1.2t$ [43].

Chapter 3

Electronic and optical properties of circular graphene quantum dots in a magnetic field

3.1 Introduction

As already mentioned in Chapter 1, the energy spectrum of graphene is linear at two inequivalent points (K and K') in the Brillouin zone, and such a linear behavior is a characteristic of relativistic massless particles, which can be described by the Dirac-Weyl equation [44]. Due to the well-known Klein tunneling effect [22], which prevents carrier confinement, manufacturing graphene based quantum structures is a big challenge for its future applications in electronic devices. However, the energy of charge carrier states in graphene can be manipulated either by using external magnetic fields, which leads to the appearance of Landau levels for an infinite graphene sheet, or by using finite size graphene quantum dots (GQD's), which will be the subject of this chapter [45].

The energy levels of circular graphene dots in the presence of a perpendicular magnetic field were first investigated analytically in Ref. [46], for the special case of the infinite mass boundary condition (IMBC). On the other hand, it is well known that the electron and hole states in graphene nanostructures depend sensitively on the edge topology. As has been extensively shown and discussed in Chapter 2, in graphene nanoribbons with zigzag edge termination a band of zero-energy edge-localized states is found, a feature present in graphene flakes, such as triangular and hexagonal GQD's [47, 48]. In fact, except for the case where all the edges of the

graphene flake have armchair shape, the appearance of the zero energy states seems to be robust with respect to edge roughness, as demonstrated by the persistent finite density of these states observed in realistic quasi-circular GQD's [40].

In the end of previous chapter it has been shown that zigzag nanoribbons with zero energy edge states are prone to spontaneous magnetic ordering once the electron-electron interaction is included [49]. This many-particle interaction leads to a small energy gap. In similar systems, such as zigzag-edge dominated GQD's, spin polarization is found as well [50]. In the presence of an IMBC, the single-particle energy spectrum of a GQD already exhibits a gap around zero energy for low magnetic fields [46]. Thus in this case no magnetic ordering is expected. Therefore, it is important to determine what notable differences in the energy spectra may arise from the application of different boundary conditions. Furthermore, because of the possible applications of the GQD's for light detection and solar energy conversion [51], it is interesting to explore how the choice of the boundary condition affects the absorption spectrum.

In this chapter, we analytically solve the Dirac-Weyl equation for a circular graphene quantum dot in the presence of a perpendicular magnetic field, for both infinite-mass and zigzag boundary conditions (ZZBC). A comparison between the energy spectra and angular current densities obtained for each boundary condition will be made. In addition to the exact solutions, we also present analytic expressions where the magnetic field is treated as a perturbation, which agrees well with the exact solution for small fields. Further, we discuss the effect of a magnetic field on the optical spectrum of a circular GQD, where we analyze the effect of different boundary conditions (i.e. ZZBC and IMBC) on the inter-band optical transitions.

Finally, in order to validate the continuum model we will also present the results obtained within the tight binding model, where there is no ambiguity as far as the boundary conditions are concerned [52]. The analytical spectra obtained by the Dirac-Weyl equation will be compared to those obtained by the tight-binding (TB) model for circular dots. Two kinds of dots will be considered in the TB model: i) a circular dot cut out from a graphene honeycomb lattice, and ii) a circular confinement region delimited by an infinite-mass barrier. The former case has an admixture of zigzag and armchair edges and, due to the zigzag parts, a band of quasi-zero energy levels is found. In the latter case, no zero energy states are present. It is critically examined how the continuum model results compare to the TB results, and which microscopical details in the latter are not captured by the approximations

made in the former.

3.2 The continuum approach

The Dirac-Weyl Hamiltonian for low-energy electron states in graphene, in the presence of a perpendicular magnetic field and a mass-related potential, reads

$$H = v_F(\mathbf{p} + e\mathbf{A}) \cdot \boldsymbol{\sigma} + V(r)\sigma_z. \tag{3.1}$$

Here $\boldsymbol{A} = (0, B\rho/2, 0)$ is the vector potential in symmetric gauge and $\boldsymbol{\sigma}$ denotes the Pauli matrices, which takes into account contributions of two different graphene sublattices. The polar coordinate system is employed since it better suits the geometry at hand. In this chapter we uphold the convention so that this equation holds for the K valley states, and $\boldsymbol{\sigma}$ in this equation should be replaced by its complex conjugate $\boldsymbol{\sigma}^*$ when considering states in the K' valley. It is assumed that the carriers are confined in a circular area of radius R, which is modeled by an infinite mass outside the dot, i.e. $V(r) = 0$ for $r < R$, and $V(r) \to \infty$ for $r \geq R$, where r is the radial coordinate of the cylindrical coordinates system. In the case of the adopted ZZBC, the two Dirac cones are labeled by the quantum number k, which has the value $+1$ in the K valley, and -1 in the K' valley. For the IMBC, however, we use the so called valley-isotropic form of the Hamiltonian, with fixed $k = +1$, and the valleys are differentiated by another quantum number τ, which appears in the boundary condition itself[1]. Furthermore, we introduce the dimensionless variables $\rho = r/R$, $\beta = R^2/2l_B^2 = eBR^2/2\hbar$ and $\varepsilon = E/E_0 = ER/\hbar v_F$, where E is the carrier energy, v_F is the Fermi velocity, and $l_B = \sqrt{\hbar/eB}$ is the magnetic length. The Dirac equation (3.1) in these dimensionless units reduces to the form

$$\begin{bmatrix} 0 & \pi_- \\ \pi_+ & 0 \end{bmatrix} \begin{bmatrix} \psi_1(\rho,\phi) \\ \psi_2(\rho,\phi) \end{bmatrix} = \varepsilon \begin{bmatrix} \psi_1(\rho,\phi) \\ \psi_2(\rho,\phi) \end{bmatrix}, \tag{3.2}$$

where $\pi_\pm = -ie^{\pm ik\phi}\left[\partial_\rho \pm \frac{ik}{\rho}\partial_\phi \mp k\beta\rho\right]$. Because of the coupling between the orbital angular momentum L_z and pseudospin $\hbar\sigma_z/2$ we define the total momentum $J_z = L_z + \hbar\sigma_z/2$. We have $[H, J_z] = 0$, i.e. the total angular momentum is a conserved

[1] k is used for ZZBC and τ is used for IMBC which was done in order to simplify our calculations.

quantity, and thus the two-component wave function has the form:

$$\psi(\rho,\phi) = e^{im\phi}\begin{pmatrix} \chi_1(\rho) \\ e^{ik\phi}\chi_2(\rho) \end{pmatrix}, \tag{3.3}$$

where $m = 0, \pm1, \pm2, ...$ is the total angular momentum quantum number. The two components of the wave function correspond to different sublattices, say χ_1 corresponds to the sublattice A, and χ_2 corresponds to the sublattice B.

Equation (3.2) is solved with the boundary condition which expresses that the outward current at the graphene edge is zero. This leads to the following relation at the dot edge [53]

$$\tan(\phi) = -\Re\big[\psi_1^*(1,\phi)\psi_2(1,\phi)\big]/\Im\big[\psi_1^*(1,\phi)\psi_2(1,\phi)\big]. \tag{3.4}$$

where $\Re(\Im)$ is the real (imaginary) part. The following two boundary conditions

$$\frac{\psi_2(1,\phi)}{\psi_1(1,\phi)} = i\tau e^{i\phi} \rightarrow \frac{\chi_2(1)}{\chi_1(1)} = i\tau, \tag{3.5a}$$

$$\psi_1(1,\phi) = 0 \rightarrow \chi_1(1) = 0, \tag{3.5b}$$

both satisfy Eq. (3.4). The condition given by Eq. (3.5a) is called the infinite mass boundary condition [53] and imposes the requirement that the region outside the dot is forbidden for particles, due to the relationship $v_F \propto 1/m$, as demonstrated in Ref. [54]. $\tau = +1(-1)$ is used to label the $K(K')$ states. The condition Eq. (3.5b) requires that one of the wave function components is zero at the dot edge, which is called the zigzag boundary condition (ZZBC) [55]. Note that a graphene quantum dot with circular geometry in principle includes both armchair and zigzag edges at the boundary, which will be considered in Section 3.3 within the TBM model. Here, within the continuum model, we consider for definiteness only ZZBC at the edges. In the case of armchair edges the boundary condition includes the wave function spinors corresponding to both K and K' points which is given by

$$\psi_1^K e^{i\boldsymbol{K}.\boldsymbol{r}} + \psi_1^{K'} e^{i\boldsymbol{K'}.\boldsymbol{r}} = 0, \tag{3.6a}$$

$$\psi_2^K e^{i\boldsymbol{K}.\boldsymbol{r}} + \psi_2^{K'} e^{i\boldsymbol{K'}.\boldsymbol{r}} = 0. \tag{3.6b}$$

In addition to k and τ, we show below that the states in the analyzed circular GQD are labeled by the total angular quantum number m and the principal quantum

number n. Therefore, it is convenient to denote them by the symbol (m, n). The symbol n is also identified as the Landau level number. In discussing the various properties of the spectrum in the continuum model we use the notation $\varepsilon^{p}_{k,m,n}$, where $p \in e, h$ denotes electron (hole) eigenvalues, k is the valley index if considering the ZZBC spectrum, while it is relpaced by τ if considering the IMBC spectrum. Furthermore n is omitted in zero field discussions.

3.2.1 Zero energy solutions

When $\varepsilon = 0$, the differential equations (3.2) are decoupled,

$$\frac{d\chi_1(\rho)}{d\rho} - \frac{mk}{\rho}\chi_1(\rho) - k\beta\rho\chi_1(\rho) = 0, \tag{3.7a}$$

$$\frac{d\chi_2(\rho)}{d\rho} + \frac{(mk+1)}{\rho}\chi_2(\rho) + k\beta\rho\chi_2(\rho) = 0. \tag{3.7b}$$

which offers straightforward solutions of the form $\chi_1(\rho) = C_1\rho^{mk}e^{k\beta\rho^2/2}$ and $\chi_2(\rho) = C_2\rho^{-(mk+1)}e^{-k\beta\rho^2/2}$.

These solutions can not simultaneously satisfy the IMBC of Eq. (3.5a) and be normalizable. Namely, if the normalization condition is imposed, either C_1 or C_2, depending on the sign of m, should vanish, which prevents Eq. (3.5a) from being satisfied. Thus, we conclude that there are no zero energy states in the IMBC spectrum.

If the ZZBC, Eq. (3.5b) is employed, it is possible to find normalizable zero energy solutions in both valleys. Those solutions are constructed by assuming $C_1 = 0$, and $C_2 \neq 0$ for both the $m < 0$ states in the K valley and the $m > 0$ states in the K' valley. Therefore, adopting the ZZBC allows the appearance of a zero energy band. Those wave function components have the form $\chi_1(\rho) = 0$ and $\chi_2(\rho) = C\rho^{-(mk+1)}e^{-k\beta\rho^2/2}$, with $mk = -1, -2, -3, \ldots$. Obviously, these states are completely pseudo-spin polarized, and reside on the B sublattice sites. The form of the wave function indicates that all states, except $mk = -1$, are edge localized, as is expected for zero energy zigzag states. Furthermore, states with larger $|m|$ are localized closer to the edge.

3.2.2 Non-zero energy solutions for $\beta = 0$

When $\varepsilon \neq 0$ and when the magnetic field is zero, i.e. $\beta = 0$, Eqs. (3.2) are coupled. Substitution of χ_2 from the second into the first differential equation leads to the Bessel differential equation

$$\rho^2 \frac{d^2\chi_1(\rho)}{d\rho^2} + \rho \frac{d\chi_1(\rho)}{d\rho} + \left(\varepsilon^2\rho^2 - m^2\right)\chi_1(\rho) = 0, \tag{3.8}$$

with solution

$$\chi_1(\rho) = C_1 J_m(\varepsilon\rho). \tag{3.9}$$

From Eq. (3.2), the relation between the first and the second component of the wave function follows

$$\psi_2(\rho,\phi) = \frac{e^{ik\phi}}{\varepsilon}\left(-i\partial_\rho + \frac{k}{\rho}\partial_\phi + ik\beta\rho\right)\psi_1(\rho,\phi), \tag{3.10}$$

and thus

$$\chi_2(\rho) = ikC_1 J_{m+k}(\varepsilon\rho). \tag{3.11}$$

The boundary condition (3.5a) leads to the equation $\tau J_m(\varepsilon) = J_{m+1}(\varepsilon)$, while the boundary condition (3.5b) gives $J_m(\varepsilon) = 0$. Recalling that the Bessel functions obey the properties $J_m(\varepsilon) = (-1)^m J_{-m}(\varepsilon)$ and $J_m(\varepsilon) = (-1)^m J_m(-\varepsilon)$, several interesting properties of the zero-field energy spectra are derived: i) there is electron-hole symmetry in both valleys for ZZBC, which is reflected by the expression $\varepsilon^e_{\pm1,m} = -\varepsilon^h_{\pm1,m}$. Unlike ZZBC, IMBC is known to break electron-hole symmetry [55], so the former relations do not hold. However there is a similar symmetry property for the IMBC, for which the expression $\varepsilon^e_{\pm1,m} = -\varepsilon^h_{\pm1,-(m+1)}$ holds. ii) Intervalley spectrum symmetry is present for the ZZBC: $\varepsilon^{e,h}_{+1,m} = \varepsilon^{e,h}_{-1,m}$, whereas for the IMBC $\varepsilon^{e,h}_{+1,m} = \varepsilon^{e,h}_{-1,-(m+1)}$. The latter two properties for IMBC further indicate intervalley electron-hole symmetry between states of the same m, i.e. $\varepsilon^e_{\pm1,m} = -\varepsilon^h_{\mp1,m}$. iii) Finally, we may deduce that the energy spectrum within each valley is either doubly degenerate (for $m \neq 0$, $\varepsilon^{e,h}_{\pm1,+m} = \varepsilon^{e,h}_{\pm1,-m}$) or non-degenerate (for $m = 0$) if ZZBC is adopted where this is not the case for IMBC.

3.2.3 Non-zero energy solutions for $\beta \neq 0$

For the general case $\varepsilon \neq 0$ and $\beta \neq 0$, we obtain the differential equation for χ_1

$$\left(\frac{d^2}{d\rho^2} + \frac{1}{\rho}\frac{d}{d\rho} - [2\beta(m+k) + \frac{m^2}{\rho^2} + \beta^2\rho^2 - \varepsilon^2]\right)\chi_1(\rho) = 0, \tag{3.12}$$

where the symmetric gauge is used for the magnetic field. This equation has the normalizable solution

$$\begin{aligned}\psi_1(\rho,\phi) =& Ce^{im\phi}\rho^m e^{-\beta\rho^2/2}\times \\ & {}_1\widetilde{F}_1\left(\frac{2m+k+1}{2} - \frac{\varepsilon^2}{4\beta}, m+1, \beta\rho^2\right),\end{aligned} \tag{3.13}$$

where we used the relation $\psi_1(\rho,\phi) = e^{im\phi}\chi_1(\rho)$, obtained from Eqs. (3.2) and (3.3), and ${}_1\widetilde{F}_1(a,b,z)$ is the regularized confluent hypergeometric function. The second component of the wave function is extracted from Eq. (3.10), and for the $K(k=1)$ and $K'(k=-1)$ valleys read

$$\begin{aligned}&\psi_2(\rho,\phi) = ikCe^{i(m+k)\phi}\frac{2\rho^{m+k}}{\varepsilon}\left[\frac{(1-k)}{2} + \frac{(1+k)}{2}\frac{\varepsilon^2}{4}\right]\times \\ &e^{-\beta\rho^2/2}{}_1\widetilde{F}_1\left(\frac{2m+k+1}{2} - \frac{\varepsilon^2}{4\beta}, m+k+1, \beta\rho^2\right).\end{aligned} \tag{3.14}$$

The IMBC leads to the following eigenvalue equation:

$$\begin{aligned}&\frac{\tau\varepsilon}{2}{}_1\widetilde{F}_1\left(m+1-\frac{\varepsilon^2}{4\beta}, m+2, \beta\right) - \\ &\qquad {}_1\widetilde{F}_1\left(m+1-\frac{\varepsilon^2}{4\beta}, m+1, \beta\right) = 0,\end{aligned} \tag{3.15}$$

while for the ZZBC we obtain

$${}_1\widetilde{F}_1\left(\frac{2m+k+1}{2} - \frac{\varepsilon^2}{4\beta}, m+1, \beta\right) = 0. \tag{3.16}$$

From (3.15) and (3.16) we may deduce that for each BC the magnetic field breaks all but one symmetry property, which were stated in previous section. Thus from Eq. (3.15) one may notice that the energy levels of the K and K' valleys are symmetric as $\varepsilon^e_{\pm1,m} = -\varepsilon^h_{\mp1,m}$. On the other hand, when the ZZBC is adopted, Eq. (3.16) depends on ε^2, and consequently the electron and hole states in each valley are symmetric with respect to each other.

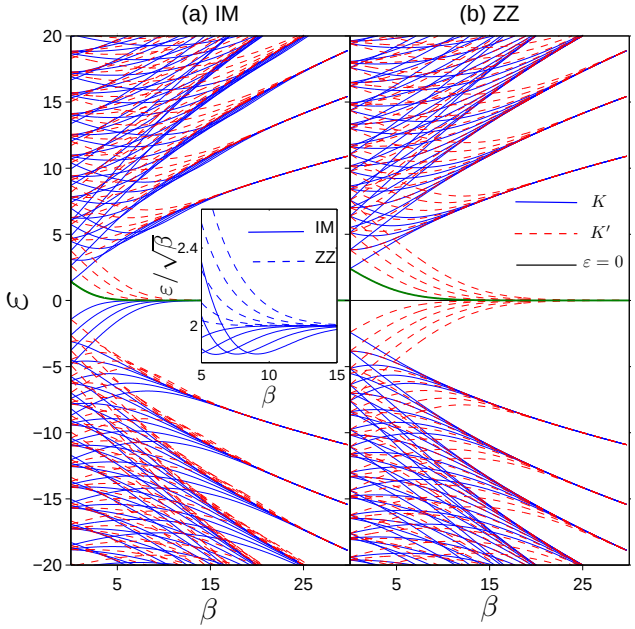

Figure 3.1: Energy spectrum of a circular graphene quantum dot with $R = 70$ nm in a perpendicular magnetic field for: (a) the IMBC, and (b) ZZBC. The energy levels corresponding to the K and K' valleys are shown respectively by the blue solid curves and red dashed curves. The zigzag zero energy state (ZES) is shown by the black solid line. The green solid curves display the fitted function to the first energy levels. Only the six lowest electron and hole energy levels are shown for $-4 \leq m \leq 4$. The inset of panel (a) shows an enlargement of the energy levels, corresponding to the K valley, around the region where the quantum dot states merge to form the first LL for both IMBC (solid curves) and ZZBC (dashed curves).

3.2.4 Energy spectrum

We now analyze the magnetic field dependence of the energy spectra in more detail. In Fig. 3.1 we show the energy levels of a circular dot with radius $R = 70$ nm and $-4 \leq m \leq 4$ for both the (a) IMBC and (b) ZZBC cases. The spectrum at the K valley is displayed by the solid blue curves, whereas the red dashed curves denote the energy levels in the K' valley. The zero energy localized zigzag state (ZES) is shown by the horizontal solid black line in Fig. 3.1(b). Notice that IMBC leads to an energy gap in the spectrum for low magnetic fields, as evident in Fig. 3.1(a). The lowest non-zero electron energy level in both IMBC and ZZBC initially decreases linearly with magnetic field (as is similar for semiconductor quantum dots) but then decreases as a Gaussian at high magnetic fields (which is different from the $1/\beta$ behavior found in semiconductor quantum dots). We fitted the energy level to a Gaussian function $\varepsilon(\beta) = a\exp(-([\beta - b]/c)^2)$ (see green solid curves in Fig. 3.1(a,b)) where $(a, b, c)_{IMBC} = (3, -3.9, 4.55)$ and $(a, b, c)_{ZZBC} = (4.47, -7.1, 9)$ are

the fitting parameters, respectively, for the IMBC and ZZBC. We found a relation between the parameter c of the different energy levels: $c^i_{IMBC} \approx 1.15\ c^{i-1}_{IMBC}$ and $c^i_{ZZBC} \approx c^{i-1}_{ZZBC}$ (with i being the eigenstate index) respectively for IMBC and ZZBC [56].

The magnetic ordering at the dot edge breaks reversal symmetry, and thus the electron-hole symmetry for each valley is broken, even when an external magnetic field is absent. Therefore, the energies of the electron and hole states in a given valley are not mutually related. However, the magnetic ordering cannot break the intervalley electron-hole symmetry for IMBC which is apparent by the $\varepsilon^e_{\pm 1,m} = -\varepsilon^h_{\mp 1,m}$ relationship in Fig. 3.1(a) [46].

Unlike the IMBC, the ZZBC produces the ZES, composed of the $m \leq -1$ states in the K valley, and $m \geq +1$ states in the K' valley (see Section 3.2.1). Zero-energy states are a trademark feature of infinite structures with bipartite lattices which have the property of a *global imbalance* in the number of sublattice sites. These states are pseudo-spin polarized, inhabiting exclusively one sublattice, and are found at exactly zero energy. On the other hand, GQD's possess *local imbalance* in the number of sublattice sites, and should therefore exhibit quasi-zero-energy states, without pseudo-spin polarization. As a matter of fact, the shift from zero energy occurs due to the hybridization between close sites with different character of the imbalance [57]. This means that the zigzag edges in real GQD's will be host to quasi-zero energy states, a property captured well with the Dirac-Weyl model, since we find a band of states at exactly zero energy in the case of zigzag boundary condition. This issue will be discussed in more detail in Section 3.3, where we use the TB model when calculating the energy spectrum of a circular GQD. For a different geometry which includes both zigzag and armchair edges at the boundaries, e.g. a rectangular graphene flake, the energy spectrum exhibits zero-energy states due to the presence of the zigzag edge. It was shown in Ref. [58] that for the case of a rectangular graphene dot the number of degenerate zero energy states depend on the number of armchair atoms.

With increasing magnetic field, the quantum-dot states merge to form the Landau levels of graphene. In contrast with semiconductors, the LL's in graphene are non-equidistant and exhibit a square-root dependence on the magnetic field [59]. For the IMBC, the first LL ($n = 1$) is composed out of $m \leq 0$ states, and the higher energy ($n > 1$) LL's are formed out of $m < n$ states in both the K and K' valleys. Such a behavior is similar to semiconductor QD's [59]. This behavior is also true

for the LL's in the K valley of the ZZBC, displayed by the solid lines in Fig. 1(b). The $m \leq 0$ states in the K' valley spectrum for the adopted ZZBC and the $m < 0$ states in both valleys for the applied IMBC form the zero energy ($n = 0$) Landau level (ZLL). We point out that for both IMBC and ZZBC, only one of the valleys contribute to the zeroth Landau level in each band, which is known to be the case in bulk graphene, and is the reason behind the anomalous QHE [44]. For the IMBC, Eqs. (3.7a) and (3.7b) do not exhibit a physical solution at zero energy, therefore the quantum dot states which form the ZLL cannot have exactly zero energy in the employed continuum model.

The asymptotic dependence of the energy levels (except for the $n = 0$ state) in both the K and K' valleys for the employed IMBC and large β is given by

$$\varepsilon^{e,h}_{\pm 1,m,n}(\beta) = \pm\sqrt{4\beta\left(n_\rho + \frac{|m| + m}{2}\right)}, \tag{3.17}$$

where $+$ $(-)$ corresponds to electrons (holes). For the ZZBC,[1] this relationship also holds for the K valley LL's, whereas the energy level dependence on magnetic field in the K' valley for large β is given by

$$\varepsilon^{e,h}_{-1,m,n}(\beta) = \pm\sqrt{2\beta\left(2n_\rho + |m| + m - 2\theta(m)\right)}. \tag{3.18}$$

Here, $n_\rho = 1, 2, 3, ...$ is the radial quantum number, which labels the solutions of Eqs. (3.15) and (3.16) and $\theta(m)$ is the Heaviside step function. For $m = 0$ Eq. (3.18) leads to Eq. (3.17) for IMBC. Note that each expression in parentheses in Eqs. (3.17) and (3.18) is equal to an integer, and therefore has the meaning of the Landau level index n, as discussed in Chapter 1. Furthermore, two different regimes of carrier confinement might be resolved: at low magnetic fields, the confinement is due to graphene termination (i.e. edge confinement). The influence of the edge is suppressed when the magnetic field is large, and the confinement becomes dominated by magnetic field. However, in the continuum model, no matter how large the magnetic field is, it will not suppress the zero energy band. ZES and its degeneracy will persist throughout the magnetic confinement regime in the ZZBC spectrum, while its wave function is pushed inwards, toward the center of the dot (see Sec-

[1] One can also easily calculate the spectrum stemming from $\psi_2(1, \phi) = 0$. The differences, as opposed to the $\psi_1(1, \phi) = 0$ spectrum, can be summed up by valley inversion and a shift in angular momentum quantum number so that $\varepsilon^{\psi_2(1,\phi)=0}_{\pm 1,m} = \varepsilon^{\psi_1(1,\phi)=0}_{\mp 1,m\pm 1}$. This means that the ZLL is found only in the K valley, i.e. $\varepsilon = 0$ states exist only for $mk = +0, +1, +2, \ldots$, etc.

tion 3.2.1). For both adopted boundary conditions, the transition between the two confinement regimes takes place as the magnetic field increases (see Fig. 3.1). We may define the transition points between the two regimes as the points where the energies of the states in the quantum dot differ negligibly from the LL energy. These transitions shift towards larger magnetic field with lower m. We should note that the observed dependence of the electron and hole energy levels on magnetic field differ from the one in semiconductor quantum dots, where neither ZES nor $n = 0$ LL are found, and the Landau levels increase linearly with β. Moreover, energies of the negative m states obtained from (3.15) have a tendency to undershoot the positive m energies of the same Landau level, which is not the case for solutions of Eq. (3.16), as displayed in the inset in Fig. 3.1(a).

Approximate variations of the electron energy levels with magnetic field, as obtained from first order perturbation theory (see Appendix B), are displayed in Fig. 3.2. These energy levels are compared with the exact solutions for the IMBC K valley. Because the applied magnetic field is considered as a perturbation for the zero-field states, a good agreement between the approximate and exact energy levels is found at low magnetic fields. As a matter of fact, the two approaches start to disagree when the confinement starts to be dominated by the magnetic field. Except for the ZES, similar agreement between the exact calculations and perturbation theory is found for the states in both valleys when the ZZBC is adopted. Notice that the approximate model cannot describe the states which form the $n = 0$ LL.

3.2.5 Angular current

In spite of the major differences in nature of the low-energy quasiparticles, there are some unexpected similarities between semiconductor and graphene quantum dots. One such similarity is the magnetic field dependence of the spatial distribution of the angular current density. The angular current for the K valley states is given by

$$j = v_F \left[\psi^\dagger \sigma_\phi \psi\right], \tag{3.19}$$

where

$$\sigma_\phi = \begin{bmatrix} 0 & -ie^{-i\phi} \\ ie^{i\phi} & 0 \end{bmatrix}. \tag{3.20}$$

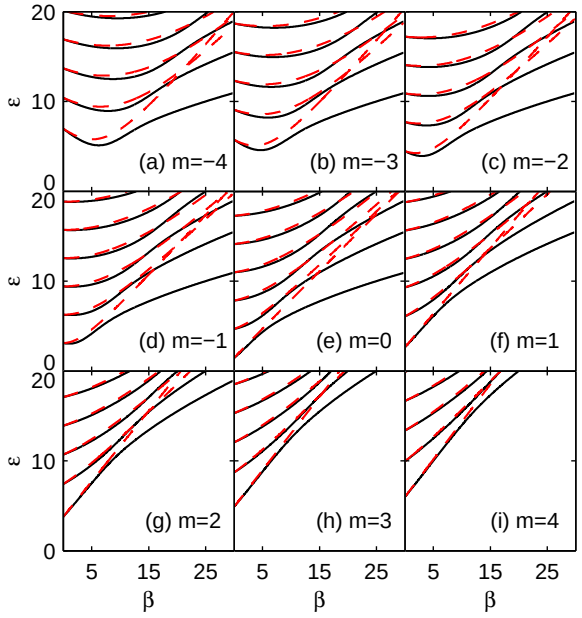

Figure 3.2: Energy levels of a circular graphene dot as function of magnetic field, $\beta = eBR^2/2\hbar$ with $R = 70$ nm. The red dashed curves show the approximated spectrum in low magnetic fields, while the exact results are shown by the black solid curves.

For K' valley one has to use the complex conjugate of the previous operator. The final expressions for the angular currents are:

$$j_{\phi K} = -2iv_F\chi_1\chi_2, \tag{3.21a}$$

$$j_{\phi K'} = 2iv_F\chi_1\chi_2. \tag{3.21b}$$

A density plot of the angular current as a function of magnetic field and radial coordinate is shown in Fig. 3.3. The ZES exhibits a peculiar property of zero angular current, due to their pseudo-spin polarization. Eq. (3.21b) indeed indicates that if any of the two wave function components is zero, the current vanishes. The angular currents for the $m = +1, n = 2$; $m = -4, n = 0$; $m = -10, n = 1$ and $m = -1, n = 1$ states are shown in Fig. 3.3. We show results for the positive m states, the states which form the ZLL, and the $m < 0$ states which form the $n = 1$ LL. The angular currents are shown for the IMBC K valley, but quite similar contourplots are obtained for IMBC K' valley, and both valleys for the ZZBC. The angular currents for the non-negative m states have the same direction as the current of classical orbits (see Fig. 3.3(a)). The internal magnetic field (due to the motion of the electron) is in the opposite direction to the external magnetic field, therefore

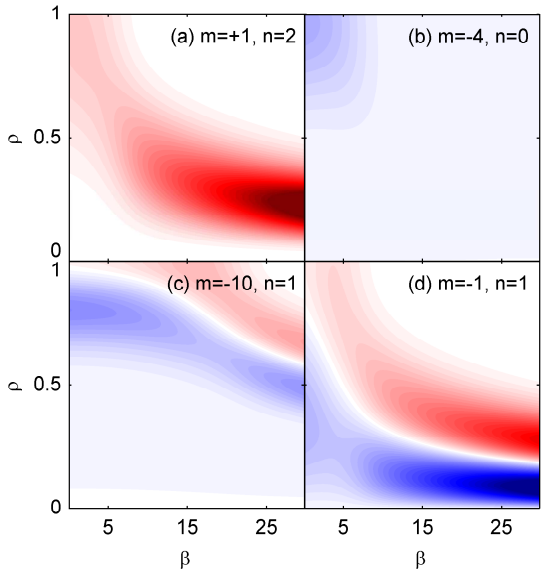

Figure 3.3: Contourplot of the angular current density for several states versus the normalized magnetic field and the radius. (a) The $(+1, 2)$ state, (b) the $(-4, 0)$ state, (c) the $(-10, 1)$ state, and (d) the $(-1, 1)$ state. The counterclockwise and clockwise currents are denoted by red and blue colors, respectively.

all non-negative m states exhibit diamagnetic behavior.

Conversely, the state $(m, n) = (-4, 0)$ which forms the ZLL shows weak paramagnetism (small angular current) at low magnetic fields, which diminishes when the magnetic field increases, as displayed in Fig. 3.3(b). Such a paramagnetic behavior might be explained by edge skipping orbits close to the edge of the dot that result in a clockwise current. However, as the magnetic field increases, the angular current in the $n = 0$ states vanishes due to the sublattice polarization, like in the ZES. Indeed, a closer look at Eqs. (3.10) reveals the reason behind it: since $|\psi_2| \sim |\psi_1|/\varepsilon$, shrinking ε will cause the second sublattice wave function to increase in magnitude as compared to the first sublattice wave function. Hence, the ZLL state becomes almost completely localized on the second sublattice with increasing magnetic field, which results in the reduction of the angular current.

The $m < 0$ and $n > 0$ states exhibit a different behavior with increasing magnetic field, as demonstrated in Figs. 3.3(c) and (d) for the $(-10, 1)$ and $(-1, 1)$ states. Both these states converge to the $n = 1$ Landau level as β increases. As is depicted, paramagnetic, i.e. clockwise current located mostly close to the edge is the prominent feature of an uncondensed state $(-10, 1)$ at low β. On the other hand, the $(-1, 1)$ state is energetically closer to the respective Landau level at $\beta = 0$ than $(-10, 1)$, which accounts for the larger diamagnetic part of the angular current in

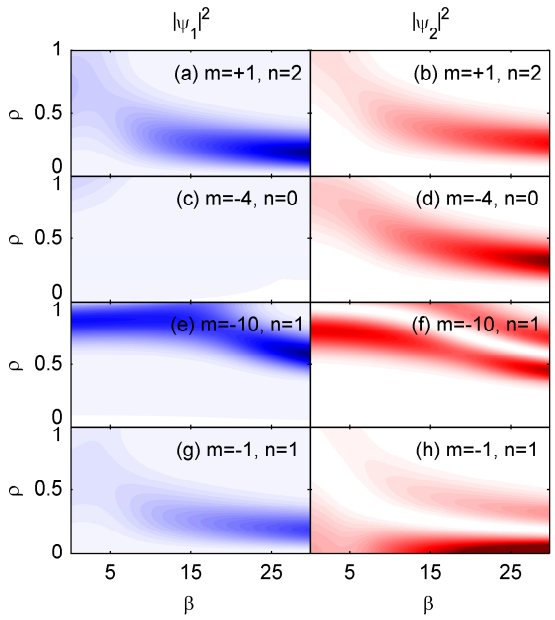

Figure 3.4: Contourplot of the sublattice contributions for several states versus the normalized magnetic field and the radius. (a) $m = +1, n = 2$ state, (b) $m = -4, n = 0$, (c) $m = -10, n = 1$ state and (d) $m = -1, n = 1$ state. Red and blue denote electron weights on sublattices 2 and 1, respectively.

this state. As the magnetic field increases, three effects take place: i) the regions of clockwise current shift towards the ring center, which might be explained as the displacement of the centers of the electron classical orbits inward, i.e. towards the dot center. ii) Two concentric regions of oppositely oriented angular currents become distinct, i.e., increasing field gives rise to a counterclockwise current on the outer side of the orbits. In fact the latter property is related to the degree of Landau level condensation of each state, i.e. to the energy difference between the quantum dot state and the Landau level. The lower this difference is, the more pronounced the diamagnetic component is. This is made clear in Fig. 3.3(d), for the $(-1, 1)$ state, which is closer to the first Landau level than $(-10, 1)$, and thus has comparatively stronger counterclockwise current. iii) The region of the counterclockwise current shifts inward too, almost parallel to the region of the clockwise current, as shown in both Figs. 3.3(c) and (d).

In order to describe in more details how the magnetic field affects the electron localization and the angular currents analyzed above, we show in Fig. 3.4 contourplots of $|\psi_1|^2$ and $|\psi_2|^2$, in the ρ and β plane, for the same states as in Fig. 3.3. All the states become localized close to the dot center with increasing magnetic field, with the $n = 0$ state resisting the most. Notice that the components of the

wave function of the $(+1, 2)$ state are comparable to each other over the considered magnetic field range. The latter state has $|\psi|^2$ localized close to the dot edge when the magnetic field is low. For the $(-4, 0)$ state, when β increases, ψ_2 starts to dominate, as previously explained, and at high magnetic field ($\beta \approx 10$) it becomes pseudo-spin polarized, as shown in Figs. 3.4(c) and (d). Notice the transition from a non-polarized to a polarized pseudo-spin state, which also highlights the transition from the edge dominated to the magnetic field dominated confinement regime. The eigenfunction representing the n-th Landau level in an infinite monolayer graphene sheet, considering the Landau gauge for the vector potential, is given by [60]

$$\langle x, y|\psi\rangle_n = \frac{e^{ik_x x}}{\sqrt{4\pi}} \begin{pmatrix} \pm\langle y|n-1\rangle \\ \langle y|n\rangle \end{pmatrix}, \tag{3.22}$$

where k_x is the wave vector in the x-direction and $|n\rangle$ is the n-th eigenfunction of the quantum harmonic oscillator in the y-direction. For the ZLL ($n = 0$), the upper component is zero and, consequently, this state is fully pseudo-spin polarized for an infinite graphene sample. In the GQD case, as the magnetic field increases, the lowest energy states, which are not pseudo-spin polarized in the edge confinement regime, approach the ZLL and become pseudo-spin polarized, as expected for this level if no edges are present, i.e. in the regime where the magnetic field confinement dominates. Figures 3.4(e) and (f) show how the wave function components vary in the $(-10, 1)$ state. The spatial localization in this state is less affected by the magnetic field than the localization of the $(-1, 1)$ state, which is displayed in Figs. 3.4(g) and (h). However, $|\psi_2|^2(\rho)$ of both the $(-10, 1)$ and $(-1, 1)$ states have two maxima, which is related to the simultaneous presence of paramagnetic and diamagnetic currents in these states shown in Figs. 3.3(c) and (d).

3.2.6 Optical absorption

Optical absorption, for transition between states i and j, is measured by $|M_{ij}|^2 = |\langle\Psi_i|re^{i\phi_p}|\Psi_j\rangle|^2$, where ϕ_p is formally the polarization angle, having no impact on the final result. Having calculated the matrix elements describing the transition for each possible pair of states, we introduce a Lorentzian-type broadening for the absorption spectrum, and consider Fermi-Dirac statistics:

$$A_{ij}(E) = \frac{\Gamma_{ij}}{\omega} \frac{\left(f_{FD}(\varepsilon_i, \varepsilon_F, T) - f_{FD}(\varepsilon_j, \varepsilon_F, T)\right) M_{ij}}{(\varepsilon - \varepsilon_{ij})^2 + \Gamma_{ij}^2}, \tag{3.23}$$

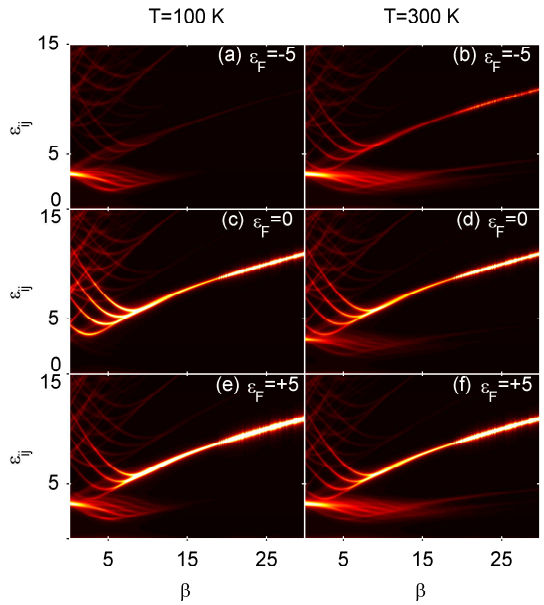

Figure 3.5: Contourplot of the total absorption spectrum $A(\varepsilon)$ for the IMBC, versus magnetic field and transition energy for different values of temperature. Left and right panels respectively correspond to temperatures $T = 100$ K and 300 K. (a) $\varepsilon_F = -5$, $T = 100$ K, (b) $\varepsilon_F = -5$, $T = 300$ K, (c) $\varepsilon_F = 0$, $T = 100$ K, (d) $\varepsilon_F = 0$, $T = 300$ K, (e) $\varepsilon_F = +5$, $T = 100$ K, (f) $\varepsilon_F = 5$, $T = 300$ K.

where T is the temperature, and ω corresponds to the energy of the incident photon ($E = \hbar\omega$). f_{FD} is the Fermi-Dirac distribution and Γ_{ij} is the broadening parameter, which is assumed to be 1 meV in our calculations. The total absorption spectrum is taken to be the sum of all individual transitions $A(E) = \sum_{i,j} A_{i,j}(E)$ for both valleys.

The integral with respect to ϕ in the matrix element M_{ij} is non zero only when $m_j = m_i$. Furthermore, no selection rule applies to n, which differs from the case of massive graphene, where transitions are allowed only between adjacent Landau levels [61]. Although transitions between states which do not differ by ± 1 in the value of n are allowed in the GQD, we found that their contribution to the overall absorption is a few orders of magnitude smaller than the contribution of the $n \to n \pm 1$ transitions. The matrix elements between the six lowest energy states for m in the range $[-4, +4]$ are taken into account when computing the absorption spectra, which are displayed as contour plots in Fig. 3.5 for the applied IMBC and two values of temperature, $T = 100$ K and $T = 300$ K. For each T, the absorption spectra are computed for (dimensionless) Fermi energies $\varepsilon_F = -5$, 0, $+5$. In all cases displayed in Fig. 3.5, there exist bright spots around $\varepsilon_{ij} = 3$. They arise from the $n = -2 \to n = -1$ and $n = 1 \to n = 2$ transitions, and are appreciable when the Fermi level is either

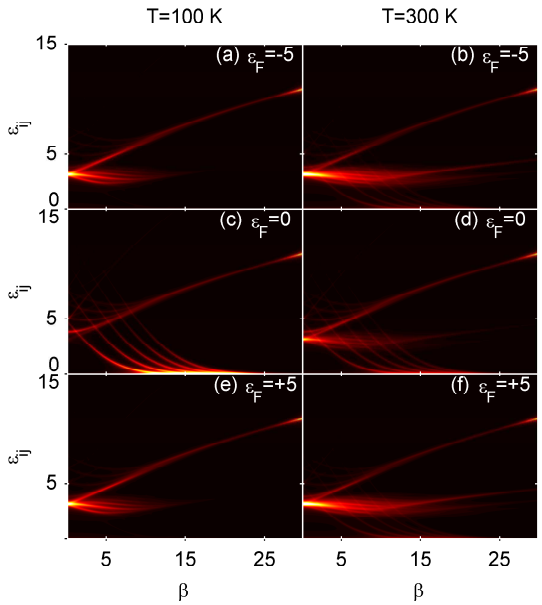

Figure 3.6: The same as in Fig. 3.5, but for the ZZBC.

in the conduction or the valence band (Figs. 3.5(a), (b), (e) and (f)). Because of the peculiar statistical distribution for $\varepsilon_F = 0$ at temperature as low as $T = 100$ K, the central bright spot disappears from the absorption spectrum, as Fig. 3.5(c) indicates. However, when T increases to 300 K, the statistical distribution of the initial and final states changes, and the bright spot reappears for $\varepsilon_F = 0$ (see Fig. 3.5(d)).

The absorption spectra for the ZZBC shown in Fig. 3.6 display similar features as the absorption for the IMBC in Fig. 3.5. In addition to the bright spot, the absorption spectra for both applied boundary conditions exhibit the bright and narrow absorption line which traverses all diagrams in Figs. 3.5 and 3.6 nearly diagonally, and it is stronger for the IMBC. This absorption takes place by means of the $n = -1 \rightarrow n = 0$ and $n = 0 \rightarrow n = 1$ transitions in the case of the IMBC. For this case, the energies of the transitions between the states in the two valleys are equal, which favors the appearance of this line. On the other hand, for the adopted ZZBC the energy spectrums of the electron and hole are symmetric within each valley, whereas intervalley electron-hole symmetry is absent. It leads to a less pronounced central absorption peak in the spectrum, which is due to transitions between the ZES and $n = \pm 1$ LL in both valleys. The other noteworthy feature for the ZZBC and $\varepsilon_F = 0$ is the absorption due to interband transitions between the $n = 0$ quantum-dot states in the K' valley, whose transition energy tends to zero when the magnetic field increases [62].

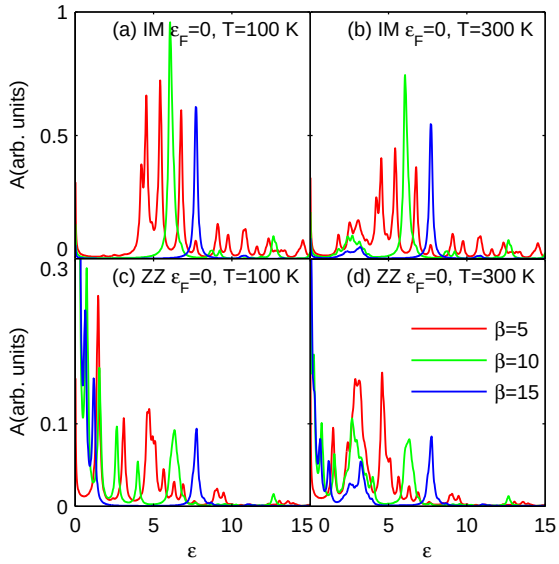

Figure 3.7: The absorption spectra $A(\varepsilon)$ for $\varepsilon_F = 0$, and two different boundary conditions. Results are shown for $T = 100$ K and 300 K which are displayed in the left and right panels, respectively. (a) The IMBC and $T = 100$ K, (b) the IMBC and $T = 300$ K, (c) the ZZBC and $T = 100$ K, and (d) the ZZBC and $T = 300$ K.

The absorption spectra for $\varepsilon_F = 0$ and three values of the magnetic field, $\beta = 5$, 10, and 15, are shown in the left and right panel of Fig. 3.7 for $T = 100$ K and $T = 300$ K, respectively. The strongest absorption line is due to the $n = -1 \rightarrow n = 0$ and $n = 0 \rightarrow n = 1$ transitions for the IMBC and for transitions between ZES and $n = \pm 1$ LL for the ZZBC. As previously explained, the lack of intervalley electron-hole symmetry for the ZZBC leads to much smaller absorption than for the IMBC. Furthermore, the absorption might increase when the magnetic field increases [63].

3.3 The tight-binding analysis of circular graphene dots

It is clear that the advantage of using the continuum model lies in the fact that it illuminates the underlying physics with analytical solutions which are easy to handle. However, the continuum model was derived from the tight-binding model [18] for an infinite graphene sheet, under the restriction of low-energy charge carriers around the Dirac cones in K and K'. Therefore, it is of interest to investigate the validity range of the continuum model for finite size structures such as GQD's.

Actual dot structures are normally cut out from a graphene honeycomb lattice,

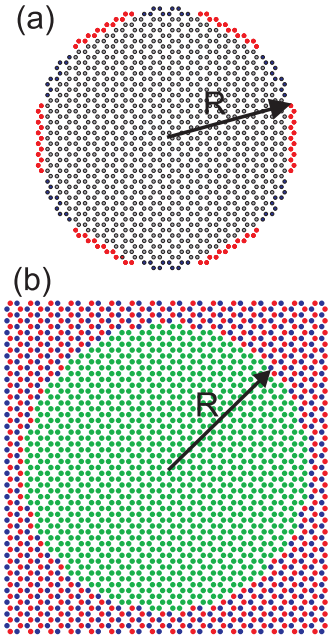

Figure 3.8: Sketch of the two circular graphene dots of radius R considered in our TB calculations: (a) a circular dot cut out from the graphene honeycomb lattice, where the red (blue) sites refer to zigzag (armchair) boundaries; (b) a circular region (green) surrounded by an infinite mass medium, which is obtained by applying a staggered potential, i.e. a $+1$ (-1) eV on-site potential for lattice A (B) sites, represented by red (blue) atoms. In both cases, the dot is made out of all the atomic sites which are inside a circle of radius R, and which have at least two nearest-neighbors sites inside the circle. Adapted from [56].

instead of being surrounded by an infinite mass media, and therefore cannot have only one type of edges, as illustrated in Fig. 3.8. However, we intend to demonstrate that the simple boundary conditions described in Section 3.2 provide results which agree somewhat with the TB results. The results in this section are obtained from the nearest-neighbor tight binding Hamiltonian, which is given by

$$H = \sum_n E_n c_n^\dagger c_n - \sum_{nm} t e^{i\phi_{nm}} c_n^\dagger c_m, \tag{3.24}$$

where E_n is the on-site energy and $c_i(c_i^\dagger)$ is the annihilation (creation) operator, $t = 2.7$ eV is the zero magnetic field hopping term for the C-C distance $a_0 = 0.142$ nm, $\phi_{nm} = \frac{e}{\hbar}\int_{r_n}^{r_m} \boldsymbol{A}\cdot d\boldsymbol{l}$ is the Peierls phase with $\phi_0 = h/e$ being the magnetic quantum flux (see Appendix A for a detailed derivation of this factor), and $\boldsymbol{A} = Bx\,\hat{\boldsymbol{y}}$ is the vector potential taken in the Landau gauge for perpendicular magnetic field B.

Let us first analyze the case of a circular dot cut out from a graphene lattice,

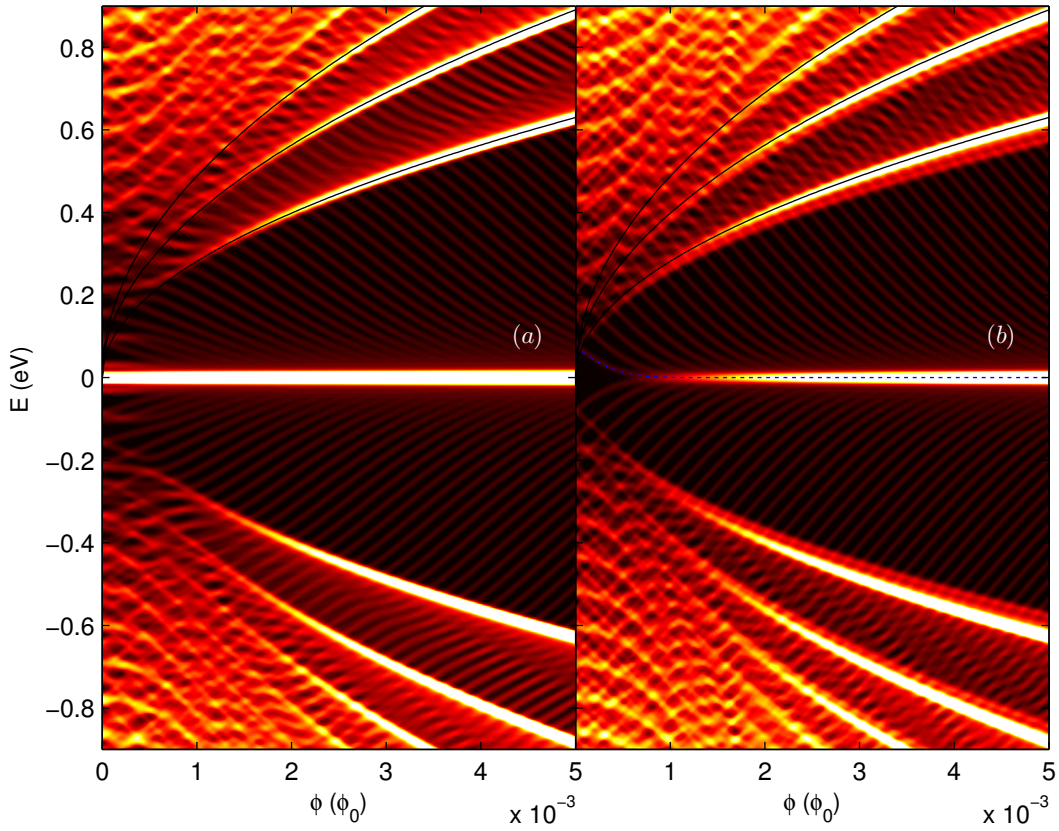

Figure 3.9: Density plot of the energy spectrum as function of the magnetic field, obtained from the TB model for (a) the cut-out graphene dot and (b) for confinement in the quantum dot delimited by the region with massive particles. The dot radius equals $R = 10$ nm in both cases. The black curves represent the Landau levels in graphene. The blue dashed curve in panel (b) shows the function which fits the dependence of the first energy level from ϕ/ϕ_0.

which is shown in Fig. 3.8(a). The energy spectrum for $R = 10$ nm is shown in Fig. 3.9(a) as a function of the magnetic flux through one carbon hexagon $\phi = (3\sqrt{3}a_0^2/2)B$. It looks qualitatively similar to the one shown in Fig. 3.1(b) for a circular dot with ZZBC computed by the continuum model. In both cases, groups of states decrease in energy with increasing magnetic field, eventually converging to the Landau levels, and the zero energy level is observed irrespective of magnetic field. On the other hand, some details of the energy spectrum at low magnetic field are not properly described by the continuum model, even at low energy. For instance, the results of both the continuum and TB models exhibit a decrease of the first non-zero level with increasing field, whereas the second level starts to increase with field until it crosses a higher energy level. However, the TB results exhibit anticrossings immediately above the crossing, which are not observed in the continuum model with the ZZBC. The IMBC results shown in Fig. 3.1(a) lack such anticrossings.

One should note that this feature is observed even in the low energy range, in which the continuum approximation should be valid. Therefore, it can be said that the continuum model cannot capture the details of edge physics in this case.

There is also a surprising feature in the energy spectrum obtained by the TB model: as we zoom in around the zero-energy region, we realize that it is not really a single $E = 0$ curve, but rather a band of curves, as Fig. 3.10 shows. We considered three different ranges of energy and found curves that exhibit a self-similar-like pattern, which persists except for the lowest energy levels, which are indeed very close to zero ($\approx 10^{-8}$ eV).

The results in Figs. 3.9 and 3.10 were obtained for $R = 10$ nm. As the dot

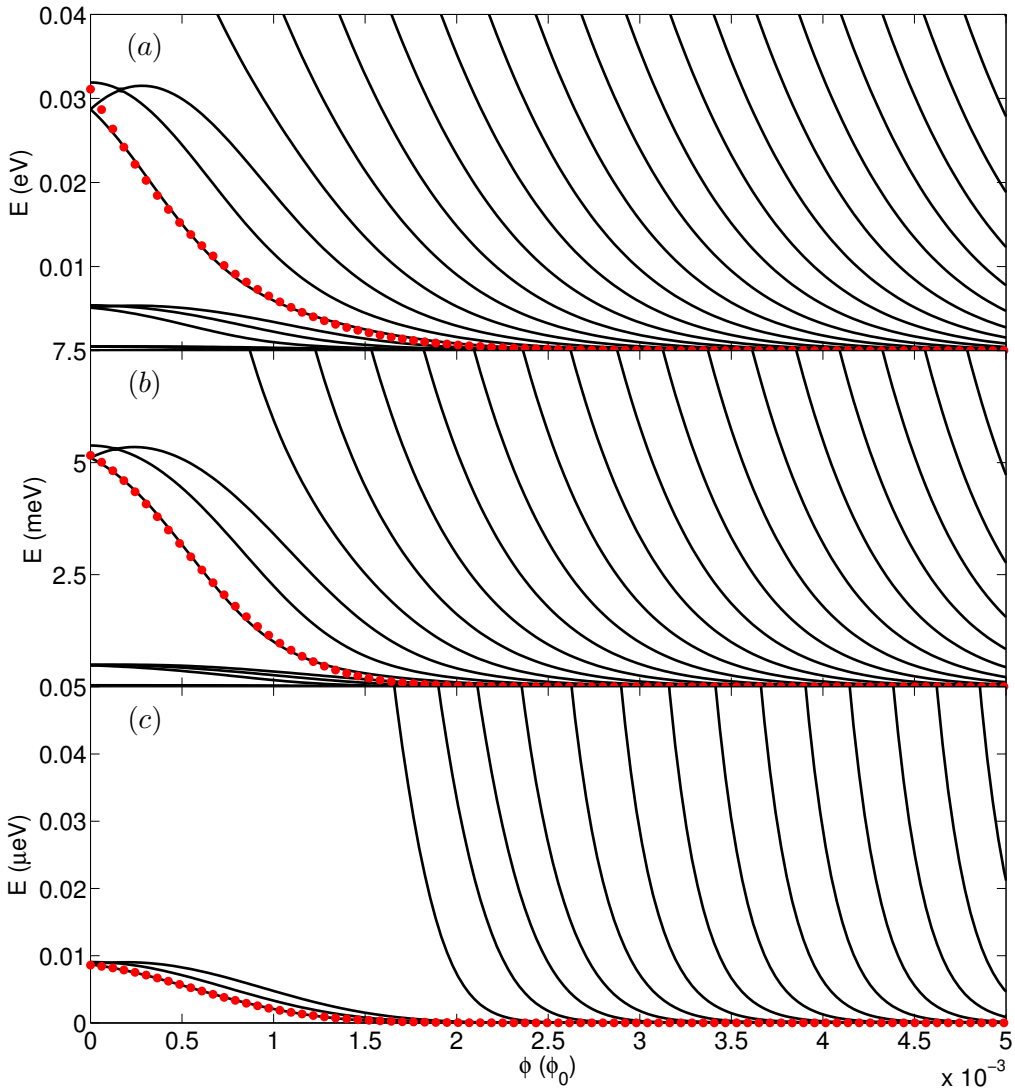

Figure 3.10: The energy spectra shown in Fig. 3.9(a) are repeated at three different energy scales. The red dots are obtained by fitting the several lowest energy states with the Gaussian functions.

radius is reduced, similar results are observed but the low energy states appear further away from the zero level. For example, for $R = 2$ nm, the lowest level has the energy $E \approx 0.095$ eV, i.e. a 0.19 eV wide energy gap, even though the dot still exhibits zigzag edge segments. The wave functions of these low energy states are localized at the zigzag edges of the circular dot (see Fig. 3.11). The lowest energy states are maximally localized, being confined only to pockets in the vicinity of zigzag-edge dominated regions (indicated by the red dots in Fig. 3.8(a)). Notice furthermore that for small B those low energy levels are grouped in threesomes: 1) the two lowest are degenerate for $B = 0$ and their wave functions are identical up to a rotation of 60° and 2) the third level has a slightly larger energy with a wave function exhibiting more pockets at the edge with a higher rotational symmetry than the previous two. As the magnetic flux increases, the degeneracy of the two lowest levels becomes lifted in each group and the second state crosses the third non-degenerate state at some value of the magnetic flux. For even higher flux, all these states decrease and eventually form the zeroth Landau level.

Similar to the results of the continuum model the first energy levels for both IMBC and ZZBC can be fitted by the Gaussian function, $f(\Phi) = a \exp\big(-([\Phi - b]/c)^2\big)$, where $(a, b, c)_{IMBC} = (0.16, -0.0006, 0.0007)$ are the fitting parameters for the IMBC (see the blue dashed curve in Fig. 3.9(b)) and the fitting parameters for the first energy level for the ZZBC are $(a, b, c)_{ZZBC} = (0.0008, -11, 92) \times 10^{-5}$ (see the red dotted curve in Fig. 3.10(c)). Note that the upper energy levels (those decreasing with magnetic field) can also be fitted by the Gaussian function, as shown by the red curves in Figs. 3.10(a,b) for the ZZBC. The fitting parameters for the states shown by red lines in Fig. 3.10(a) and Fig. 3.10(b) equal $(a, b, c)^{(a)}_{ZZBC} = (0.13, -0.0022, 0.0018)$ and $(a, b, c)^{(b)}_{ZZBC} = (0.0053, -0.00018, 0.0009)$, respectively.

We now analyze the case of a circular dot surrounded by an infinite mass medium, as illustrated in Fig. 3.8(b). Spatial symmetry breaking in epitaxial graphene, although challenging, is quite achievable, as recent experiments demonstrated [64–67]. As explained in Chapter 1, such a symmetry breaking is translated into a mass term in the Dirac-Weyl Hamiltonian for graphene. This suggests that a circular graphene dot embedded in an medium with massive fermions might be experimentally feasible by means of substrate engineering. Besides, as previously mentioned, the IMBC provides a good description of the magnetization at the edges of a graphene dot. This motivated us to study circular GQD surrounded by a staggered potential, which is illustrated in Fig. 3.8(b). For this case we have applied the magnetic field through-

out the entire structure. The results obtained by the TB model for such a system are indeed comparable to those obtained for the IMBC in the continuum model. As a matter of fact neither case demonstrates zero energy levels. Furthermore the anticrossings in the structure displayed in Fig. 3.9(a) are not present in the energy spectrum for the infinite mass confinement in the TB model.

Finally, we investigate how the size of the graphene dot affects their energy spectrum and compare the results from the TB and continuum models. The energy spectrum in the case of the mass confinement, illustrated in Fig. 3.8(b), obtained by means of the TB model is shown by the solid bullets in Fig. 3.12(a). The Dirac-Weyl results for the IMBC are shown by red curves, and exhibit very good qualitative and

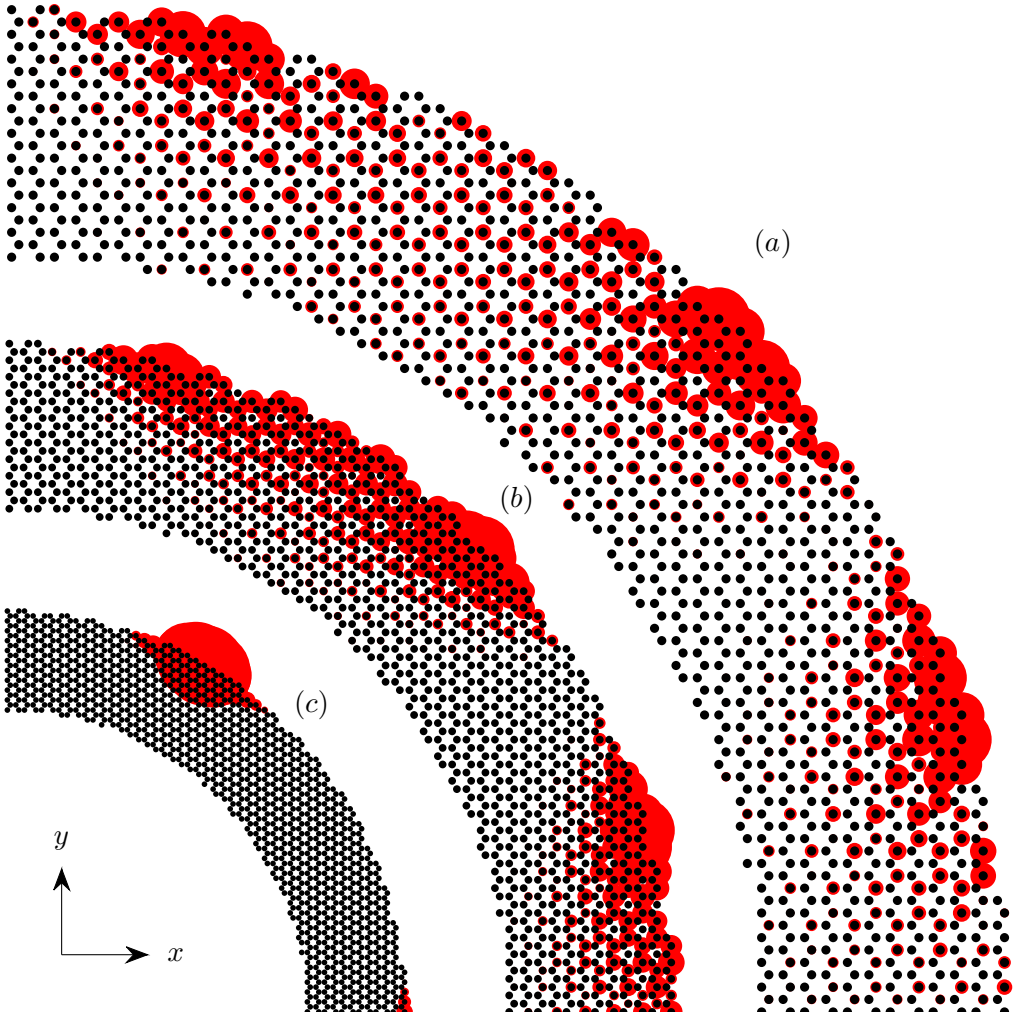

Figure 3.11: Electron densities corresponding to the energy levels shown by the red dots in Fig. 3.10 for $\phi/\phi_0 = 0$. The black dots are the position of the C-atoms, and only a small strip in the first quadrant of the circular graphene flake is shown. The energy of the states are (a) 0.0287 eV, (b) 0.0051 eV and (c) 8.7×10^{-9} eV.

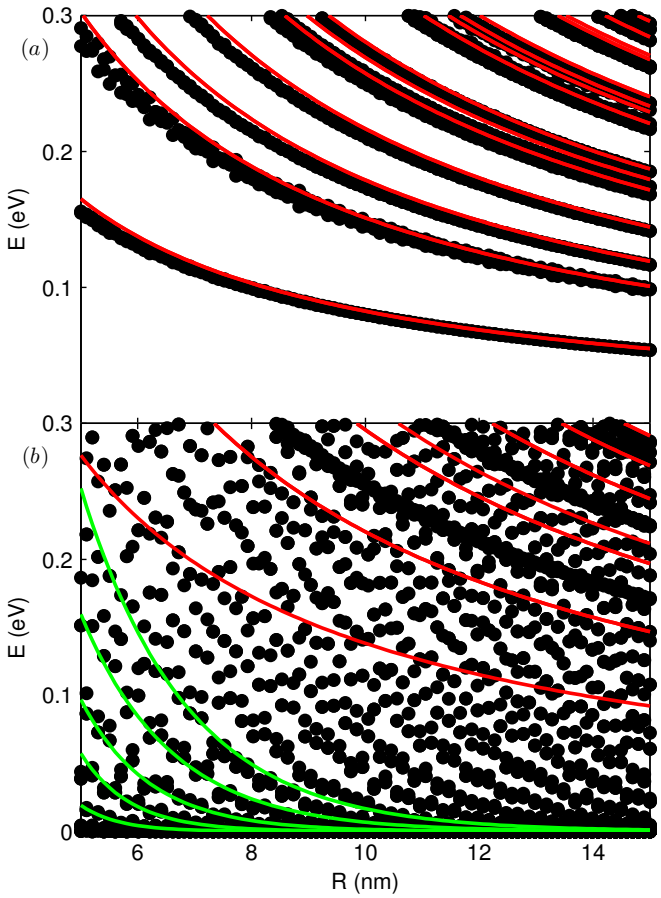

Figure 3.12: Energy spectrum as function of the dot radius, in the absence of a magnetic field, obtained from the continuum (red curves) and TB (solid bullets) models, for (a) the infinite-mass confinement in a quantum dot, and (b) the flake cut out from a graphene layer.

quantitative agreement with the TB results, especially for the low-energy states and large dots. Some curves in the TB results do not decay monotonically as $\propto 1/R$. Instead, they exhibit a fluctuating behavior, which is more pronounced for smaller radii. Such fluctuations can be linked to the fact that the GQD's studied within the TB model are never perfectly circular, as verified in the sketch of Fig. 3.8(b). In other words, the microscopical details become important as R decreases, and these details cannot be described properly by the analytical model for circular GQD's, based on the continuum approach. For a larger dot radius, these edge imperfections are less important, which explains the less pronounced fluctuations in the energy levels when R increases.

The energy spectrum as function of the radius of the circular dot which is cut out from the graphene layer is shown in Fig. 3.12(b). When compared with Fig. 3.12(a) it exhibits even larger fluctuations, the energies decrease much faster than

$1/R$, and the energy levels are spread out more evenly in the shown energy window. This is due to the fact that besides the imperfections in the circular shape of the dot, the variations in the number of zigzag and armchair atoms at the edge of the dot also plays a role in the energy spectrum when R increases. Also, the increase of the radius forces the low-energy states to merge into a very dense $E = 0$ band. This is not expected to be the case in the continuum approximation, where the states of zero energy band are perfectly degenerate with zero energy even for small radius, and higher energy states tend to zero only for $R \to \infty$. Along with the self-similarity behavior mentioned earlier, this feature is a pure manifestation of a microscopic character of the GQD's, which cannot be described by the IMBC nor ZZBC, or by any analytical model within the continuum approach known to date. Indeed, the results obtained by the ZZBC in the continuum model (red curves) do not capture the (somewhat) chaotic energy spectrum, except for the fact that they predict the $1/R$ behavior of some states observed in the TB results. The energy states that decrease much faster than $1/R$, can be fitted by an exponential function, i.e. $E^i = E_0^i e^{-R/R_0^i}$, where E_0^i and R_0^i are the fitting parameters and i denotes the eigenstate index. In Fig. 3.12(b) the five lowest energy levels are shown by the green solid curves where $E_0^{i=1,2,\ldots,5} = [33.3, 17.96, 6.24, 3.78, 3.82]$ eV and $R_0^{i=1,2,\ldots,5} = [0.67, 0.87, 1.2, 1.58, 1.84]$ nm. The parameters R_0^i can be related to each other by $R_0^i \approx 1.3 \times R_0^{i-1}$. Given these results, one is led to the conclusion that the analysis of very small graphene flakes is best done with atomistic methods able to account for the detailed picture.

Chapter 4

Antiferromagnetism in hexagonal graphene structures

4.1 Introduction

Tremendous progress in graphene research is driven by its remarkable properties, e.g. high crystalline quality, high electron mobility, lack of a band gap, and a minimal possible thickness, to name a few [8]. The mentioned properties are advantageous for various emerging applications of graphene, such as piezoelectric devices [68], supercapacitors [69], photodetectors [70], and field-effect transistors [71, 72]. On the other hand, magnetic ordering favored by zig-zag edge dominated structures is potentially advantageous for spintronic applications [73, 74]. This effect is essentially related to either the global or local imbalance of sublattice atoms in bipartite lattices. An imbalance might give rise to zero energy states in the electron spectrum. These states are localized near the zigzag edges or vacancies, and along with the repulsive electron-electron (e-e) interaction could eventually lead to a spin polarization of the ground state of the system [73]. Furthermore, the spins on the same sublattice are found to exhibit ferromagnetic coupling along the graphene edges, whereas the spins on different sublattices along the graphene edges couple antiferromagnetically.

In theory, magnetic ordering has been demonstrated for graphene flakes [50], nanoribbons [75], and vacancies in bulk graphene [57]. On the other hand, experimental reports on magnetism in graphene structures have been rare and conflicting. They range from the detection of ferromagnetic or antiferromagnetic ordering [76–78] to measurements of defect-induced paramagnetism [79, 80]. Magnetic ordering was even found to be preserved at room temperature [81, 82]. The essential cause

of magnetism in graphene is the existence of a peak in the density of nonbonding edge states near the Fermi energy. However, due to the high reactivity of these states, magnetism might be strongly suppressed [83]. Several theoretical studies offered explanations for a diversity of phenomena related to magnetic ordering and its suppression, which might occur by means of nonmagnetic edge passivation, edge reconstruction, or vanishing of spin correlations with increasing temperature [83, 84]. Hence, in order to experimentally detect magnetic ordering graphene samples should be kept under rigorously controlled conditions. In the latest turn of events, these conditions seem to have been met, as reported in Ref. [43]. This experimental work is the first to offer convincing evidence of magnetic ordering in graphene nanoribbons with precisely fabricated edge structure.

The tendency of electrons in graphene to reorganize in response to the Coulomb interaction served as an inspiration to many proposals for practical applications. They involve half-metallicity with electrically controlled spin propagation [74], defect induced spin filtering [85], and spin logic devices [86, 87]. In this chapter we employ the mean-field Hubbard model to study the formation of local magnetic moments in hexagonal graphene rings. Our aim is to explore how magnetic ordering is affected by the ring size and the edge type.

4.2 Magnetic ordering in hexagonal rings

In order to identify different hexagonal rings, we introduce the following notation which might be visually aiding. We assume that the type of the inner ring edge is zigzag, and that N unit hexagons are adjacent to this boundary. The outer ring edge is assumed to be comprised of either M dimers if it is of armchair type, or M unit hexagons if it is of zigzag type. Therefore, the ring is denoted by $M : N$. As an example, consider the ring shown in Fig. 4.1, which is assumed to be formed out of the hexagonal dot with armchair edge, which contains seven dimers at each side of the hexagon, as shown in Fig. 4.1(a). The ring is formed when the carbon atoms around the center of the dot are removed, as depicted in Figs. 4.1(a) and (b). Potentially these exotic structures could be manufactured via substitutional doping of boron nitride nanostructures with carbon [88]. Because the edge of the removed dot has four unit hexagons at each side, the ring is denoted as $7_{AC} : 4_{ZG}$. The distributions of the magnetic moments in the graphene rings will be compared with the magnetic moment distributions in the hexagonal graphene dots. Those

dots are assumed to have zigzag edges, and are labeled by N_{ZG}, where N has the same meaning as the symbol M for the rings.

Magnetic ordering of a graphene structure is governed by Lieb's theorem [89]. It states that the total ground-state spin of a bipartite lattice with repulsive *e-e* interaction as described by the Hubbard model equals half of the difference of the sublattice sites. For symmetrical structures, this rule is related to the arrangement of the carbon atoms with respect to lines of reflection symmetry in the graphene plane: if there is a symmetry line which does not intersect any of the carbon atoms the total ground state spin is zero; otherwise there exists a finite magnetic moment. All the hexagonal rings analyzed here possess such a symmetry, thus their total magnetization equals zero, unlike triangular rings which display a ferrimagnetic phase [90]. However, Lieb's theorem does not dictate the distribution of the local magnetic moments or the lack of zero energy states. Furthermore, the number of zero-energy states in the analyzed ring is an integer multiple of six, which is a consequence of the C_{6v} symmetry of the ring. In the $9_{AC} : 10_{ZG}$ ring, six zero energy states are found, which agrees with graph theory, and which is a topological property related to the nonperfect matching of the p_z orbitals [73].

The Hubbard Hamiltonian

$$H = H_0 + H_I, \tag{4.1}$$

is employed to compute the distribution of magnetic moments. H_0 is the noninteracting part, which represents the standard nearest neighbor tight-binding Hamiltonian, and is given by

$$H_0 = -t \sum_{<i,j>,\sigma} c^{\dagger}_{i\sigma} c_{j\sigma}, \tag{4.2}$$

where $c_{j\sigma}$ and $c^{\dagger}_{j\sigma}$ are the annihilation and creation operators, respectively, and t denotes the hopping integral. The interacting part H_I describes the *e-e* interaction

$$H_I = U \sum_i \left(n_{i\uparrow} \langle n_{i\downarrow} \rangle + n_{i\downarrow} \langle n_{i\uparrow} \rangle - \langle n_{i\uparrow} \rangle \langle n_{i\downarrow} \rangle \right), \tag{4.3}$$

where $n_{i\sigma} = c^{\dagger}_{i\sigma} c_{i\sigma}$ is the number operator, and U denotes the on-site Coulomb repulsion energy for each pair of electrons with the opposite spins orbiting the same atom. As elaborated in Chapter 2, Eq. (4.3) is formulated within the mean-field approximation, which assumes that the spin-up (spin-down) electrons interact with

the average density of spin-down (spin-up) electrons on a particular atomic site.

In our calculations, we take $t = 2.7$ eV and $U = 1.2t$ [73]. We note that there is no consensus on the actual value of the strength of the Coulomb interaction to be used in the Hubbard model in graphene. Recent density functional theory (DFT) calculations came up with a value closer to $U = 3.4t$ [91]. However, having in mind that the mean-field approximation can overestimate the tendency for magnetic order for large U [92], we chose the more conservative value of $U = 1.2t$. The solution is then obtained by means of a self-consistent procedure which starts from an initial distribution of the spins, and ends when the maximum change of the electron density over the atomic sites drops below 10^{-5}. When the self-consistent spin densities are determined, the magnetic moment per site m_i is computed as

$$m_i = \langle s_i^z \rangle = \left(\langle n_{i\uparrow} \rangle - \langle n_{i\downarrow} \rangle \right) /2. \tag{4.4}$$

For the antiferromagnetic order parameter we take the staggered magnetization

$$\mu_s^z = \frac{1}{N} \sum_i (-1)^i \langle s_i^z \rangle, \tag{4.5}$$

where $(-1)^i$ symbolizes that we sum up the contributions from opposite sublattices with opposite signs. This is the appropriate order parameter for antiferromagnetism when examining spin polarization occurring in bipartite lattices. The larger μ_s^z is, the stronger the antiferromagnetic phase. In addition to μ_s^z, the shift in the electron and the hole energy spectra which arises from the magnetic order is quantified as $\Delta E = \left(E^{HOS} + E^{LUS} \right) /2$, where E^{HOS} and E^{LUS} are the highest occupied and lowest unoccupied states in the ground state at half filling, respectively. Note that in the nonmagnetic state we have $\Delta E = 0$. We will explore how the maximum magnetic moment m_{max} varies with the ring width.

The distribution of the local magnetic moments in the $9_{AC} : N_{ZG}$ rings for several values of N is shown in Fig. 4.1(c). The symmetry of each hexagonal ring is C_{6v}, whereas the symmetry of the magnetic moment distribution is IC_{6v}, i.e. the magnetic moments alter sign when rotated over $\pi/3$ rad. Therefore, it suffices to display the distribution of magnetic moments in sectors of $\pi/3$ rad, as done in Fig. 4.1(c), which combines the sectors of different N. Orientation and color of triangles denotes the orientation of the magnetic moments, and the absolute value of m_i is depicted by color intensity.

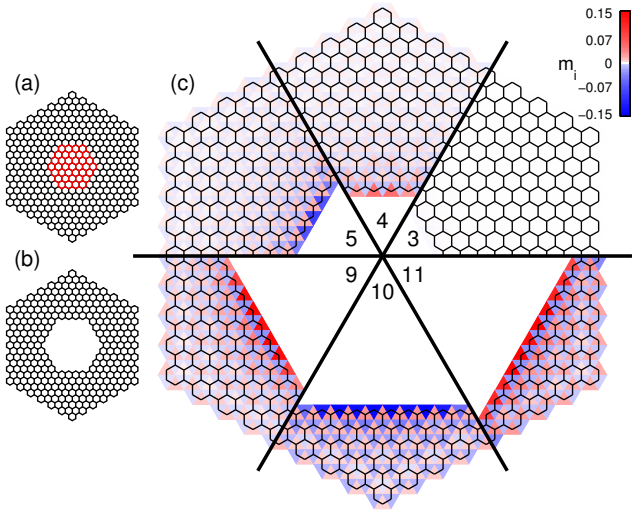

Figure 4.1: (a) The dot (red color) with four atoms at the zigzag edge removed from the larger dot (black color) which has seven dimers at the dot edge. (b) The formed ring is labeled by $7_{AC} : 4_{ZG}$. (c) The distribution of magnetic moments in the $9_{AC} : N_{ZG}$ ring shown in a sextant of the ring for N taking the values 3, 4, 5, 9, 10 and 11. The majority spin is labeled by both orientation and color of a triangle centered at an atomic site. The local magnetic moment value is proportional to the color intensity.

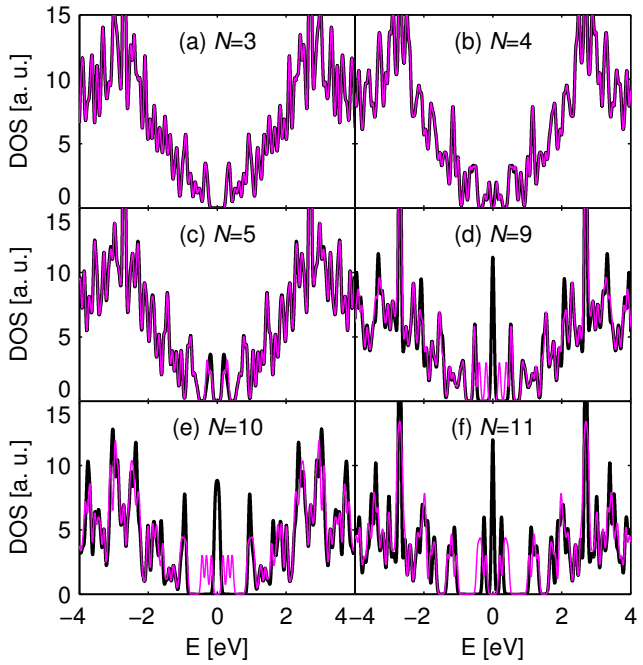

Figure 4.2: Density of states in the $9_{AC} : N_{ZG}$ rings for N taking the values 3, 4, 5, 9, 10 and 11 in the noninteracting system (black lines) and the interacting system (purple lines).

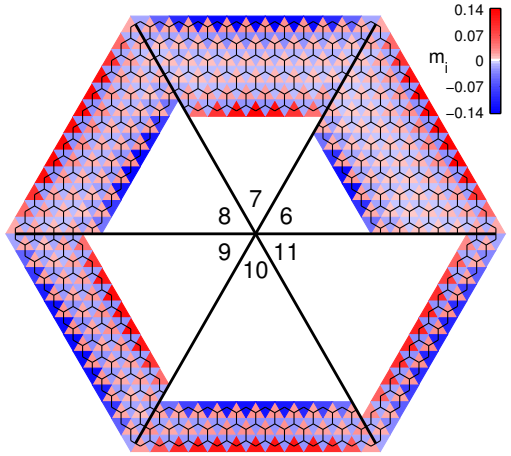

Figure 4.3: Distribution of magnetic moments in the $13_{ZG} : N_{ZG}$ rings for N ranging from 6 to 11.

It is evident in Fig. 4.1(c) that both the appearance of staggered magnetization and the total magnetic moment situated on the inner edge of the ring depend on the ring width. Furthermore, we observe a phase change from nonmagnetic order for $N \leq 3$ to antiferromagnetic order for $N \geq 4$, which is similar to previous calculations for zigzag hexagonal graphene dots [50, 75]. No magnetic ordering for zigzag segments shorter than three unit cells is found because of the close proximity of the opposite sublattice imbalance on the adjacent sides of the ring inner edge. When this edge is short, the edge states on the different sides of the inner ring boundary are subject to strong hybridization, and therefore their energy is lifted from the Dirac point. Hence, spontaneous spin polarization does not occur, which is similar to the case of nanoribbons [47].

For $N \geq 4$, the spatial spin symmetry is broken due to the e-e interaction. When the ring width decreases, the maximum magnetic moment, which is located near the middle of the zigzag edge segment increases. Furthermore, nonzero magnetization is built up on the outer ring edge, and it increases when the ring width decreases. However, as a consequence of the increasing influence of the outer edge with decreasing ring width, the difference between the distributions of the magnetic moments on the two edges is not large for $N = 10$ and $N = 11$. Similarly, the staggered magnetization increases when the ring width decreases.

Figure 4.2 shows how the density of states (DOS) of the $9_{AC} : N_{ZG}$ rings (the cases depicted in Fig. 4.1) varies with N. The density of states for the noninteracting (interacting) case is displayed by the black (purple) lines. In order to align

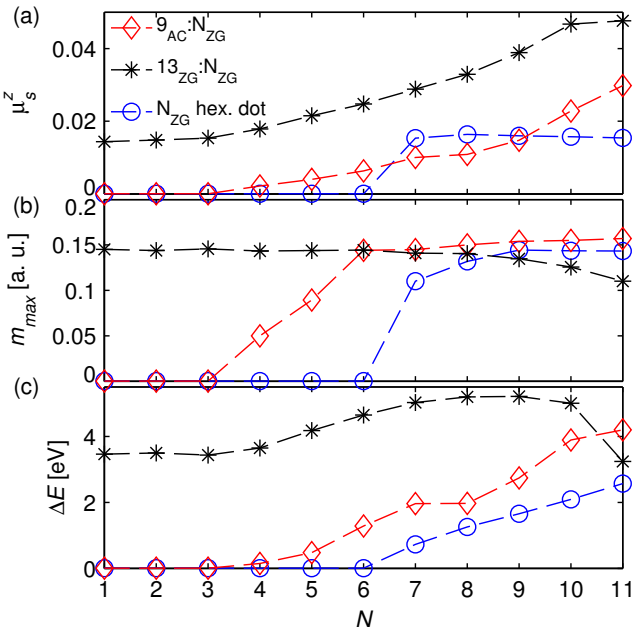

Figure 4.4: (a) Staggered magnetization μ_s^z, (b) maximum moment m_{max} and (c) energy shift ΔE as they vary with the length of the side of the inner ring edge.

the interacting and noninteracting spectra for easier comparison we subtracted ΔE for each interacting spectrum. Note that the density of states is spin degenerate, which is in accordance with Lieb's theorem. For $N = 3$, magnetic order is not present, therefore the energy dependence of the density of states for the interacting and noninteracting systems coincide (see Fig. 4.2(a)). The interacting and noninteracting electron case exhibit a small difference in the energy dependence of the DOS for rings with $N = 4$ and $N = 5$, which is shown in Figs. 4.2(b) and (c). As could be inferred from Fig. 4.1(c), the magnetization along the inner ring edge is rather small for these values of N. For larger N, the discrepancy between the DOS's for the interacting and non-interacting systems becomes larger, as demonstrated by Figs. 4.2(d)-(f) for $N = 9$, 10, and 11. In all these cases, appreciable DOS for the noninteracting system is found around zero energy. Such a configuration becomes unstable in the presence of e-e interactions, which results in the appearance of an interaction gap.

In order to demonstrate how the shape of the outer boundary affects the distribution of the magnetic moments in the ring, we show in Fig. 4.3 the magnetization in the $13_{ZG} : N_{ZG}$ rings. It is apparent that the shape of the outer edge has a large effect on the localization of the magnetic moments on this boundary (compare Figs. 4.1(c) and 4.3). It is clear that in the case of zigzag outer ring edge, the

magnetization propagates much further into the ring.

Figure 4.4 displays how μ_s^z, m_{max}, and ΔE vary with the length of the side of the inner ring edge expressed by the number N. Along with the rings whose magnetic moment distributions were shown in Figs. 4.1(c) and 4.3, the case of a hexagonal graphene dot having zigzag edge, is also displayed in Fig. 4.4. Both the staggered magnetization μ_s^z and the energy shift ΔE increase with N, i.e. with the size of the inner ring, except for the extremely narrow $M_{ZG} : N_{ZG}$ rings. Interestingly, the staggered magnetization in the hexagonal quantum dots does not exceed 0.02, whereas for the $13_{ZG} : N_{ZG}$ ring it can reach almost up to 0.05. The nearly twofold enlargement of the staggered magnetization could be accounted for by the double number of zigzag edges in the $M_{ZG} : N_{ZG}$ ring as compared to the N_{ZG} graphene dot. On the other hand, most $9_{AC} : N_{ZG}$ rings exhibit larger staggered magnetization and all show larger maximum magnetic moment than the hexagonal graphene dot. As a matter of fact, in hexagonal graphene dots the zero-energy orbitals which are localized along the adjacent zigzag sides of the edge are oriented toward each other, whereas inner zigzag edges in rings face away from each other. Hence, hybridization between the states of the two edges is larger in the former case than in the latter case. This is why $9_{AC} : N_{ZG}$ rings turn magnetic for shorter lengths of zigzag edges than hexagonal dots (four versus seven, respectively). The decrease of m_{max} with N for $13_{ZG} : N_{ZG}$ is due to the more effective hybridization between the quasi-zero-energy states localized on the inner and outer edges of the ring when the ring width decreases. Hence, the electron energy shifts from the band of zero energy states, and therefore magnetic ordering decays, which is manifested by a smaller m_{max} in the $13_{ZG} : 11_{ZG}$ ring than in the 11_{ZG} dot. The shapes of the $\Delta E(N)$ curves shown in Fig. 4.4(c) resemble the $\mu_s^z(N)$ and $m_{max}(N)$ curves in Figs. 4.4(a) and 4.4(b).

4.3 Suppression of magnetic instabilities via hybridization

In order to elucidate the difference between magnetic ordering in rings and dots, one may also analyze how the local density of states (LDOS) depends on the geometry of the structure. More specifically, the spatial distribution of the states close to zero energy determines how the magnetic moments evolve when the dimensions of the structures varies. In order to enhance the contribution of the low-energy states, we

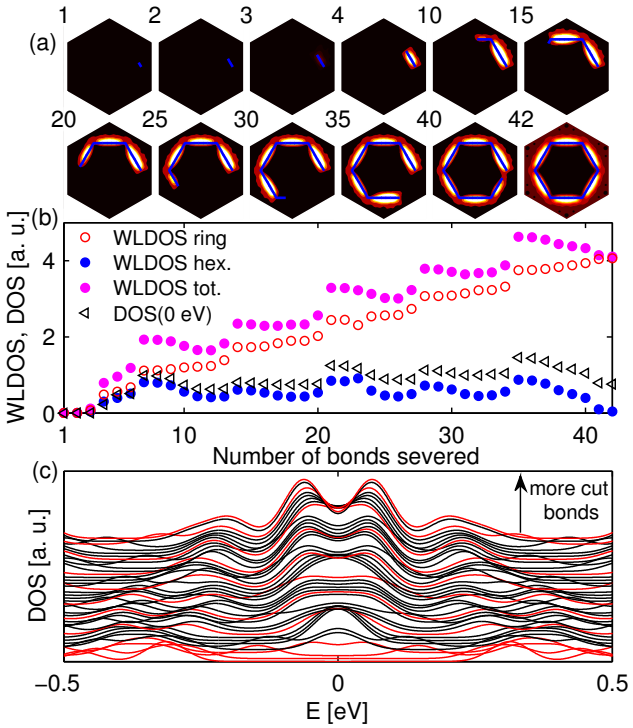

Figure 4.5: (a) Contour plot of the WLDOS at several stages of the carving process forming the $7_{AC} : 7_{ZG}$ ring and the 7_{ZG} hexagonal dot; the number in the upper left corner indicates the number of bonds cut. (b) Summed WLDOS in the ring, the dot, and in the whole structure as well as the zero energy density of states versus the number of bonds cut. (c) Stacked plot of the density of states; red depicts the densities of the stages displayed in panel (a).

will compute the weighted LDOS (WLDOS) [57]:

$$W_i = \sum_j e^{-\beta E_j^2} |\phi_{ji}|^2. \tag{4.6}$$

Here, i indexes the lattice sites, j labels the eigenstates, β is the damping coefficient chosen as $1/\sqrt{\beta} = 0.1$ eV, whereas ϕ_{ji} is the value of the probability amplitude of the j-th state at the site i. Such defined WLDOS assumes that the contribution of the states with $|E_j| > 0.1$ eV is negligible. The plots of the WLDOS in Fig. 4.5(a) illustrate how the edge states form when the inner 7_{ZG} hexagonal dot is cleaved out of the outer 7_{AC} hexagonal dot. The inner dot is separated from the ring by severing the bonds one by one between the dot and the ring. The number of the severed bonds between the dot and the ring is explicitly shown in Fig. 4.5(a), and the dot edge is depicted by the blue line. The local sublattice imbalance accumulates quickly with the number of severed bonds, but no edge states emerge when the number of cut bonds is less than four. The edge states, which are depicted by red contours around

the edge, are initially distributed evenly between the ring and the dot, but they extend more to the ring when the number of cut bonds increases.

To explore this finding in more detail, we show in Fig. 4.5(b) how the total WLDOS (full purple circles), which is the sum over the atomic sites in the dot (full blue circles) and the ring (empty red circles), varies with the number of severed bonds. Also, the DOS at zero energy is shown by the black triangles in Fig. 4.5(b). Notice that the variation of the WLDOS has a similar shape for each side of the ring's inner edge, and that the WLDOS displays step-like features. These steps arise because the imbalance between the two local sublattices, found at the ring and dot sides of the newly formed edge, are maximized when the formation of each side of the rings inner edge is completed. The next side of the rings inner edge contains the opposite sublattice imbalance, and therefore the states on this side hybridize with the states on the previous side, which leads to a decrease of WLDOS [57]. Note that after the first edge has been cut the ring and the dot WLDOSs start deviating from each other more strongly. This is because the hybridization in the dot is stronger, as the edge states on adjacent segments hybridize inward and towards each other. In the ring part the edge states face away from each other and hybridize radially outward, hence the hybridization is weaker. This is why the WLDOS in the former case experiences a decline with the beginning of each new edge segment, while in the latter case the WLDOS keeps growing. The gradual increase of WLDOS for both cases near the end of each segment is related to the accumulation of the local sublattice imbalances. This pattern reappears with each new zigzag segment, with the exception of the last bond, which after being cut results in the separation of the two structures. By the end, the WLDOS in the ring is much larger than WLDOS in the dot, which accounts for the fact that the rings exhibit a larger maximum magnetic moment and staggered magnetization than the dots. Figure 4.5(c) shows a stacked plot of DOSs for each resulting structure. Plots are stacked from the bottom up, with each subsequent line corresponding to a structure with one more bond cut. DOSs for structures depicted in Fig. 4.5(a) are colored red. It shows that only features near zero energy evolve in a similar fashion as do the WLDOSs during the separation of the ring and the dot. This justifies the damping of states higher than 0.1 eV in calculating the WLDOS, as they are not artifacts of the edge forming between the ring and the dot.

Finally, we examine the influence of the edge deformations on somewhat larger structures; namely, the $25_{ZG} : 20_{ZG}$ and $16_{AC} : 20_{ZG}$ rings and the 20_{ZG} dot. Larger

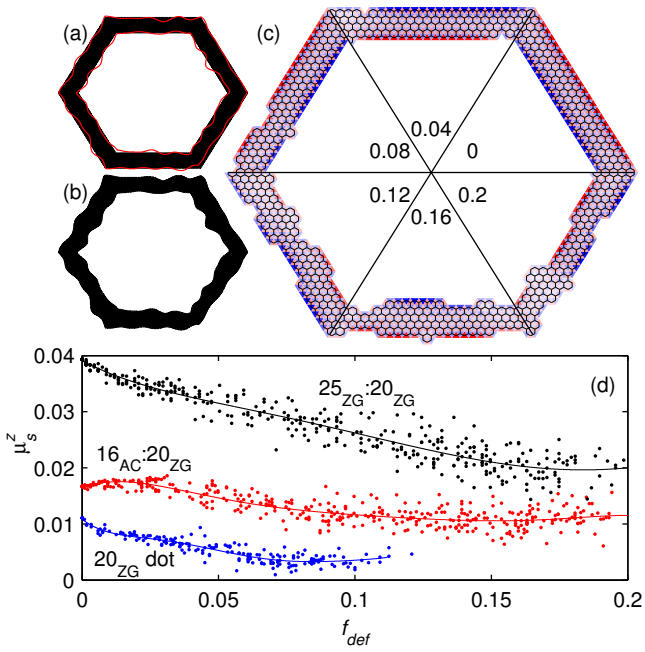

Figure 4.6: (a) Perfect edges (black region) are randomly perturbed (red lines) to produce a random set of defects. (b) Final outlook of the deformed ring. (c) Magnetic moments distributions in $25_{ZG} : 20_{ZG}$ ring for several values of f_{def}. The scale is the same as in Fig. 3. (d) Staggered magnetization of an ensemble of randomly defected structures as a function of defect ratio for $25_{ZG} : 20_{ZG}$ ring (black dots), $16_{AC} : 20_{ZG}$ ring (red dots) ring, and 20_{ZG} hexagonal dot (blue dots). The polynomial fitting curves are added to guide the eye.

structures are considered here because they can be deformed in a larger number of ways than smaller structures analyzed in the rest of the paper. Defects are induced by randomly deforming the polygons which outline the perfect structure as shown in Fig. 4.6(a). The amplitude of this deformation is itself a randomly selected number out of a specific range and the final structure is made up of all atoms that are enclosed by the deformed outline,[1] which is shown in Fig. 4.6(b). In order to quantify the amount of defects, the defect ratio f_{def} is defined as a fraction of the total number of the defects, which is a sum of the missing and the surplus sites, and the number of the sites in the original structure. The magnetic moment distributions in the $25_{ZG} : 20_{ZG}$ ring for a few values of f_{def} are shown in Fig. 4.6(c). Also, variation of the staggered magnetization with the defect fraction for the $16_{AC} : 20_{ZG}$ and $25_{ZG} : 20_{ZG}$ rings and the 20_{ZG} dot is displayed in Fig. 4.6(d). For the $25_{ZG} : 20_{ZG}$ ring and the 20_{ZG} hexagon, μ_s^z decreases with defect fraction.

[1]We remove all the dangling atoms which might appear after the edge is deformed. Also, we ensure that all the deformed structures have equal numbers of the A and B sublattice sites, thus our calculations always regarded the antiferromagnetic limit.

This is expected, having in mind that the defects can only impair the conditions for magnetism in zigzag edges. On the other hand, for the $16_{AC} : 20_{ZG}$ ring, small random defects are more likely to make the larger outer edge magnetic than to make the smaller inner edge nonmagnetic. This explains the initial rise in μ_s^z for f_{def} up to 0.02 [93].

Chapter 5

Orbital magnetic moments in insulating Dirac systems

5.1 Introduction

One of the more intriguing recent developments in the field of graphene research is the artificial generation of properties that are otherwise vanishing in intrinsic samples. For instance, carrier mass can be created by sandwiching graphene with hexagonal boron nitride, in which case a gap arises for sufficiently aligned layers [66, 67]. The occurrence of the gap is dictated by the interplay of the elastic energy of the graphene lattice, and the potential energy landscape stemming from hBN [94]. The energetically preferred commensurate structure, in which a carbon atom sits on top of a boron atom, will maximize its area at the expense of other stacking configurations by stretching the graphene layer. This in turn leads to the appearance of an average gap in the resulting van der Waals heterostructure [67].

On the other hand, it was postulated that spin-orbit coupling in graphene can be enhanced by hydrogen adsorption, which forces local rehybridization of bonds [95]. Note that quantum spin Hall transport signatures introduced by random adatoms are well described by models taking into account a renormalized and uniform SOC [96, 97]. Moreover, the proximity effect caused by an appropriate substrate was speculated to lead to SOC enhancement as well. Both of these mechanisms were recently confirmed experimentally, opening new avenues for theoretical research [98, 99].

While in graphene the carrier mass and SOC have to be artificially engineered, they are ubiquitous in other group IV monolayers such as silicene, germanene, and

stanene, thanks to their buckled structure and the heavier constituent atoms [100–102]. Note that at the time of writing of this thesis only stanene remains to be synthesized in this group; 2012 is the year in which silicene was first detected, while germanene was reportedly observed in 2014 [103–107]. And, while silicene and germanene are yet to display it, given their honeycomb lattice, they also belong to the same class of materials as graphene, with relativistic quasiparticles described by the Dirac equation. From the theoretical point of view, both of the aforementioned parameters appear in a similar form in the low-energy continuum picture. They are captured by staggered potential terms Δ and Δ_{SO} in the case of mass and SOC, respectively.[1] As explained in Chapter 1, the term "staggered potential" originates in the language of the tight-binding method, and it refers to the breaking of the sublattice symmetry by a traceless potential. Unlike SOC, for which the staggered potential changes sign depending on the spin and valley of the electron, Δ opens up a topologically trivial band gap in the vicinity of the K and K' points through inversion symmetry breaking [10], as was also pointed out in Chapter 1.

At the same time, however, the inversion symmetry breaking leads to a nontrivial alteration of the semiclassical equations of motion on a honeycomb lattice [108, 109]. The quantum corrections, which reflect the impact of the Berry phase, and are therefore topological in nature, are twofold. On the one hand, when subjected to an electric field in the plane, massive Dirac fermions will attain a velocity component transverse to the field, which is opposite in the two valleys, thus giving rise to the valley Hall effect. This effect was observed experimentally in a MoS_2 device, and also in graphene-hBN heterostructures [110, 111]. On the other hand, self-rotation of electron wavepackets near the two valleys will produce valley-contrasting orbital magnetic moments [109].

It is well established that the valley Hall and intrinsic spin Hall effects share the same origin, reflecting the Berry curvature properties of the underlying insulating systems, generated by Δ and Δ_{SO} terms, respectively. Therefore, the two Hall effects are fully analogous [112, 113]. On the other hand, valley-contrasting magnetism was first reported in Ref. [109]. Thus, exploiting the same analogy with the Hall effects, there must be magnetic moments originating from the band structure of Dirac systems with nonzero spin-orbit coupling. This type of orbital magnetization was previously investigated in a more generalized analysis of the family of Hall

[1] As noted in Chapter 1, Δ_{SO} also gives rise to massive particles, by virtue of opening the gap, however for brevity, in this and the subsequent chapter we refer only to the Δ term as mass.

effects (and the accompanying set of orbital moments), found in multilayer graphene systems in Ref. [114]. There, the electron-electron interaction leads to various broken symmetry phases, denoted by the general term "pseudospin ferromagnetism" [115–118], which are captured with a diverse set of mass terms in the low-energy continuum approximation, in models analogous to the ones studied in this thesis.

This emerging orbital magnetism is a mechanism that effectively alters the Zeeman energy, and it is the subject of this chapter, particularly the moments associated with spin-orbit coupling in monolayer Dirac systems. We first show how the intrinsic SOC in honeycomb monolayers gives rise to orbital magnetic moments coupled to spin, in the same way in which inversion symmetry breaking gives rise to moments coupled to the valley degree of freedom. These moments are completely analogous in nature, and they share exactly the same functional form, apart from coupling to different degrees of freedom. We derive expressions for the moments using both tight-binding and continuum theories, and we show their impact on the Landau level quantization in the presence of a magnetic field.

Finally, we investigate the influence of the moments on the magneto-transport properties, where we look at the transmission through a barrier with enhanced spin-orbit coupling in graphene. Such a barrier could be realized by an appropriately formed van der Waals heterostructure in an otherwise fully ultrarelativistic material [96–99] as mentioned above. We discuss this case in great detail from the semi-classical point of view, and we present conclusions that are of practical relevance, namely how the device conductance is affected by orbital magnetism. In the end of the chapter, we show that the results are identical whether one uses the continuum Dirac theory or the tight-binding nonequilibrium Green function method when calculating the transport properties. Remarkably, both approaches yield Zeeman-type transport signatures while employing the magnetic field only through kinetic terms, without actually enforcing the coupling of the spin with the magnetic field, which reflects the orbital nature of the magnetic moments [119].

5.2 Orbital moments in the tight binding picture

We start with the low-energy tight binding Kane-Mele Hamiltonian valid for a whole set of Dirac materials with prominent intrinsic spin-orbit coupling [10],

$$H = \hbar v_F \left[\tau k_x \sigma_x + k_y \sigma_y\right] + s\tau \Delta_{SO} \sigma_z, \tag{5.1}$$

where v_F is the Fermi velocity, Δ_{SO} is spin-orbit coupling, σ_z is a Pauli matrix operating in the sublattice subspace, $s = +1/-1$ labels the spin $\uparrow$ / $\downarrow$, and $\tau = +1/-1$ labels the valley K/K'. As already mentioned this form of SOC is universal to all group IV monolayers other than graphene, in which on the other hand it could be artificially generated. Note that here k_x and k_y are only parameters, and not operators. The dispersion relations extracted from Eq. (5.1) are shown by solid black curves in Fig. 5.1(a).

The Hamiltonian (5.1) describes a two-state, electron-hole symmetric system. For such systems, the orbital magnetic moment (m) is directly proportional to the Berry curvature (Ω), $m \sim \Omega$ [109, 114, 120]. On the other hand, the system is also time-reversal invariant, and since we disregard the staggered potential Δ at the moment, inversion symmetry is not broken either. Since for spatial-inversion and time-reversal symmetric systems Berry curvature vanishes [121, 122], one might conclude that the orbital moments must vanish as well. However, it is rarely stressed that this only holds for *spinless* electrons, which is not the case considered here [123]. In fact, the Hamiltonian (5.1) describes a topological insulator, having a non-zero and opposite Chern number for opposite spins [10]. This is because the Kane-Mele model is formed by two opposite copies of the Haldane model [29], thus breaking the time-reversal symmetry separately in each spin sector. Since the Chern number is obtained as an integral of Ω over the Brillouin zone, the Berry curvature is nontrivial, and consequently, the orbital magnetic moments will be nonzero.

The orbital moments are perpendicular to the monolayer, and originate from the self-rotation of the electron wave packet around its center of mass, and they can be obtained from the tight binding Bloch eigenfunctions $|u(\mathbf{k})\rangle$ [109, 114, 121]

$$m = -i\frac{e}{2\hbar}\langle\nabla_{\mathbf{k}}u| \times [H - E(\mathbf{k})]\,|\nabla_{\mathbf{k}}u\rangle, \tag{5.2}$$

which makes their topological origin much clearer. For the particular Hamiltonian in Eq. (5.1), we have

$$|u(\mathbf{k})\rangle = \begin{pmatrix} \sqrt{\frac{E+s\tau\Delta_{SO}}{2E}} \\ \tau\sqrt{\frac{E-s\tau\Delta_{SO}}{2E}}e^{i\tau\phi} \end{pmatrix}, \tag{5.3}$$

where E is the electron energy, and $\phi = \arctan k_y/k_x$. It is then straightforward to show that the expression for the magnetic moments that arise from the spin-orbit

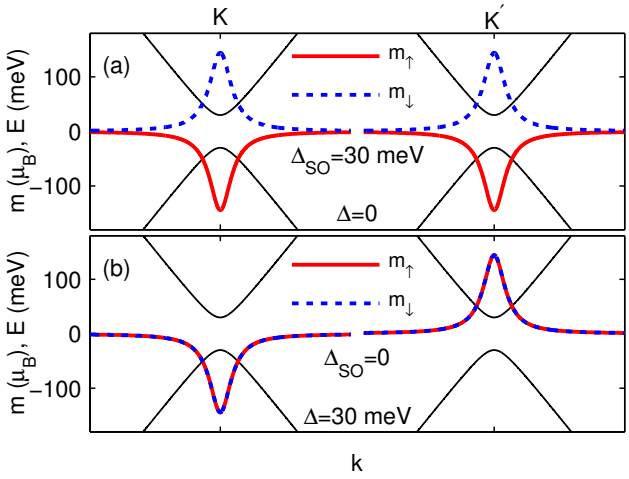

Figure 5.1: The orbital magnetic moments of the spin-up (spin-down) states shown by thick red (dashed blue) lines, and the corresponding low-energy band structure, shown in black, for: (a) $\Delta = 0$ and $\Delta_{SO} = 30$ meV, and (b) $\Delta = 30$ meV and $\Delta_{SO} = 0$. Note that in (b) the orbital magnetic moments for the two spins are equal, due to the absence of SOC.

coupling reads

$$m = -s\frac{e\hbar v_F^2 \Delta_{SO}}{2\left(\Delta_{SO}^2 + \hbar^2 v_F^2 k^2\right)}. \tag{5.4}$$

Variations of the orbital moments in the vicinity of the Dirac points are shown for both spins in Fig. 5.1(a). They are maximum near the band edges, decay away from the two Dirac points, and are obviously opposite for opposite spins.

One can compare these moments with the valley-contrasting moments, arising for $\Delta_{SO} = 0$ and $\Delta \neq 0$ [109, 121]. Their magnitude is given by

$$m = -\tau\frac{e\hbar v_F^2 \Delta}{2\left(\Delta^2 + \hbar^2 v_F^2 k^2\right)}, \tag{5.5}$$

and they are depicted in Fig. 5.1(b). It is clear that the two sets of moments share a similar functional form, except the former couple to spin, while the latter couple to the valley degree of freedom [114]. The energy region where the moments are prominent, is termed the Berry curvature hot spot in Ref. [111]. There, it was unequivocally shown that the gap in well-aligned graphene-hBN van der Waals heterostructures is accompanied by the introduction of a nontrivial Berry curvature.

Finally, in the case of both nonzero Δ_{SO} and Δ, and in the low energy limit, the

magnetic moment is given by

$$m = -\frac{e\hbar v_F^2}{2\left(s\Delta_{SO} + \tau\Delta\right)}. \tag{5.6}$$

The orbital magnetic moments are responsible for the optical selection rules of light absorption in Dirac materials, through the so-called circular dichroism effect [113, 120, 124]. Note that the orbital moments in Eq. (5.4) can dominate the Zeeman response of a system, since they can be orders of magnitude stronger than the free-electron Bohr magneton for realistic SOC strengths found in typical Dirac materials [109, 114, 118, 121]. In other words, they will lead to a renormalization of the Landé g factor, which was recently observed for transition metal dichalcogenides from first-principles calculations [125].

5.3 Landau levels, pseudospin polarization and orbital moments in the continuum picture

5.3.1 Landau levels

We proceed with the case of an applied perpendicular magnetic field $\mathbf{B} = B\mathbf{e}_z$ which is included in the Hamiltonian through minimal coupling

$$H = \hbar v_F \left[\tau k_x \sigma_x + (k_y + \frac{e}{\hbar} A_y)\sigma_y\right] + s\tau\Delta_{SO}\sigma_z + \Delta\sigma_z. \tag{5.7}$$

This equation could be employed to solve the electron spectrum in the Dirac system in the presence of Δ_{SO}, Δ, and magnetic field. It will subsequently lead us to resolve the magnetic moments. Here, the Landau gauge $\mathbf{A} = (0, A_y)$ with $A_y = Bx$ is chosen. In this gauge, k_y is a good quantum number and the solutions have the form $\Psi(x, y) = \exp(ik_y y)\left(\psi_A(x), \psi_B(x)\right)^T$. Introducing $\hbar v_F \epsilon = E$, $\hbar v_F \delta = s\tau\Delta_{SO} + \Delta$, one can obtain the LLs in the infinite graphene sheet. In solving the LL spectrum it is useful to adopt the operators $b_\tau^\dagger = -i(l_B/\sqrt{2})\left(\tau k_x + ik_y + ieA_y/\hbar\right)$ and b_τ, where $l_B = \sqrt{\hbar/eB}$ denotes the magnetic length. $b_\tau^\dagger$ and b_τ are the bosonic ladder operators, and they satisfy $\left[b_\tau, b_\tau^\dagger\right] = \tau$. It could be useful to define these operators such that they fully correspond to the standard ladder operators of the quantum harmonic oscillator (QHO) shifted by $x_0 = k_y l_B^2$ and having the mass $m = \hbar^2/l_B^4 k$. Then, as shown in Chapter 1, the eigenstates will be given by the standard (obviously

shifted and rescaled) QHO solutions

$$\langle x|n\rangle = \frac{\pi^{-1/4}}{\sqrt{2^n n!}} e^{-(x/l_B + k_y l_B)^2/2} H_n\left(\frac{x}{l_B} + k_y l_B\right), \tag{5.8}$$

where H_n are Hermite polynomials. The problem can now be solved in terms of these solutions for the case of the regular two-dimensional (2D) electron gas in a magnetic field, having in mind that $b_1^\dagger|n\rangle = \sqrt{n+1}|n+1\rangle$, $b_1|n\rangle = \sqrt{n}|n-1\rangle$ and $b_1|0\rangle = 0$, and that the ladder operators change character in the K' valley. The system of coupled equations with ladder operators is now given by

$$\delta\psi_A - i\frac{\omega_c}{v_F} b_\tau \psi_B = \epsilon\psi_A, \tag{5.9}$$

$$i\frac{\omega_c}{v_F} b_\tau^\dagger \psi_A - \delta\psi_B = \epsilon\psi_B, \tag{5.10}$$

where $\omega_c = \sqrt{2}v_F/l_B$ is the cyclotron frequency for Dirac-Weyl electrons. Then for $n \geq 1$ the energies of the LLs are given by

$$\epsilon_{n,s,\tau,\pm} = \pm\sqrt{\delta^2 + n\omega_c^2/v_F^2}. \tag{5.11}$$

The s and τ quantum numbers are contained implicitly in the definition of δ. The joint spinor for the two valleys can be written as

$$|n,s,\tau,\pm\rangle = \begin{pmatrix} |n - \frac{\tau}{2} - \frac{1}{2}\rangle \\ \pm i\left[\frac{\omega_c\sqrt{n}}{(\epsilon+\tau\delta)v_F}\right]^\tau |n + \frac{\tau}{2} - \frac{1}{2}\rangle \end{pmatrix}. \tag{5.12}$$

The case of $n = 0$ needs special attention, since the solution given by Eq. (5.12) is not valid in this case. Then, the appropriate choice for the solution is

$$|0,s,\tau\rangle = (-\tau/2 + 1/2, \tau/2 + 1/2)^T |0\rangle, \tag{5.13}$$

while the energies are expressed as [126]

$$\epsilon_{0,s,\tau} = -\tau\delta. \tag{5.14}$$

It is worth pointing out however, that observation of the conductance plateaus corresponding to the derived spectrum can depend on the symmetry class of the disorder present in the samples [127]. Note also that these eigenvectors and eigen-

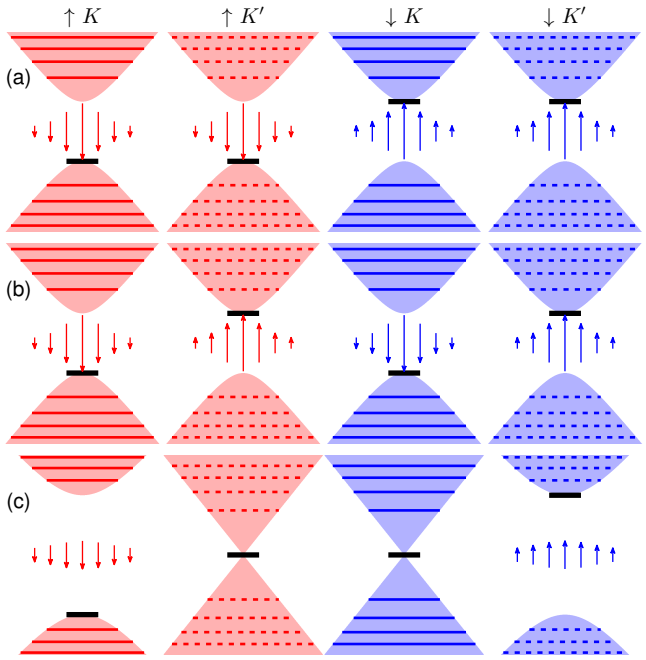

Figure 5.2: Several lowest Landau levels of all spin and valley flavors for (a) $\Delta_{SO} = 30$ meV and $\Delta = 0$, (b) $\Delta_{SO} = 0$ and $\Delta = 30$ meV, and (c) $\Delta_{SO} = \Delta = 30$ meV. The $n = 0$ Landau level is depicted by the horizontal solid black line. Also shown are the bulk bands as red (spin up) and blue (spin down) shaded regions, as well as the sketch of the corresponding orbital moments, with the length of the arrow being proportional to the intensity.

values reduce to the ones for the massless fermions, under the requirement $\delta \to 0$, collapsing the level (5.14) to zero energy. Nevertheless, massless fermions can also display quantum Hall signatures, such as a magnetic-field-independent plateau at zero filling factor, which originate from valley mixing scattering processes [127].

Thus the SOC and mass terms split and shift the zeroth LLs away from zero energy as depicted in Fig. 5.2, which shows the low-lying Landau levels for (a) only $\Delta_{SO} \neq 0$, (b) only $\Delta \neq 0$ and (c) $\Delta_{SO} = \Delta \neq 0$ at $B = 2$ T. We also depict the bands, as well as the emerging magnetic moments, given by Eqs. (5.4) and (5.5). The orientation of the moments is related to the position of the $n = 0$ Landau level, which is shown by the horizontal solid black lines. Note that the zeroth LLs always reside on the edges of the appropriate bands. The duality $\Delta_{SO} \leftrightarrow \Delta$, $s \leftrightarrow \tau$ present in Eq. (5.14) is evident in Fig. 5.2. In other words, SOC couples the LLs to spin in the same way that mass couples them to the valley degree of freedom [126, 128, 129]. The state depicted in Fig. 5.2(c) is dubbed spin-valley-polarized metal [130], and it hosts both a massless (lacking the orbital moments) and a massive relativistic Landau spectrum. It can appear in silicene subjected to a perpendicular electric

field, for instance. On the other hand, in transition-metal dichalcogenides, both parameters are inherently present, with $\Delta > \Delta_{SO}$, and SOC splits only the LLs in the valence band, yielding a unique set of Hall plateaus [131].

5.3.2 Orbital moments

The underlying explanation for the behavior of the LL spectrum can be sought in the existence of orbital magnetic moments [109, 132, 133]. In a similar fashion to Ref. [133], we can obtain the effective Bohr's magneton in the presence of Δ_{SO}, starting from the Dirac-Weyl equation, and expanding near the conduction band bottom. We first point out that near the bottom of the conduction bands, the sublattice pseudospins get polarized perpendicular to the graphene sheet, with the majority of the weight concentrated on the A (B) sublattice for $\delta > 0$ ($\delta < 0$). Likewise, at the top of the valence band, most of the weight is found on the A (B) sublattice for $\delta < 0$ ($\delta > 0$). This is obvious for the zeroth LLs, and it occurs in the $\delta = 0$ limit as well [2, 56], but to see it for higher levels it is helpful to derive the expectation value for the sublattice pseudospin,

$$\langle n, s, \tau, \pm | \sigma_z | n, s, \tau, \pm \rangle = \frac{\delta}{\epsilon}, \tag{5.15}$$

which is exactly the same as in the absence of SOC and magnetic field [134], only now it is to be used for the discrete energy values corresponding to the Landau levels. Therefore, perfect pseudospin polarization is achieved in the bottom (top) of the conduction (valence) band.

On the other hand, decoupling the Dirac equation gives

$$\left[k_x^2 + \left(k_y + \frac{x}{l_B^2} \right)^2 \pm \frac{\tau}{l_B^2} \right] \psi_{A/B} = \left(\epsilon^2 - \delta^2 \right) \psi_{A/B}. \tag{5.16}$$

Therefore, there is a spatially uniform term proportional to the magnetic field, with opposite signs on opposite sublattices and opposite valleys. Consider the importance of this term for states whose sublattice pseudospin mostly lies in the graphene plane, i.e. for states far away from the band gap, Eq. (5.15). For such states, the two signs play a tug of war, effectively canceling each other out. However, near the band gap, sublattice polarization occurs, and the term corresponding to a majority sublattice starts dominating over the other, giving rise to an effective paramagnetic moment. For instance, when $\delta > 0$ sublattice A dominates for low electron energies,

and the upper sign starts impacting the electron motion. To fully appreciate this fact, and to write the equation in a manifestly paramagnetic form, one needs to perform a low energy expansion for the equation of the majority sublattice. After reintroducing E, Δ, and Δ_{SO} explicitly, we can write $E = \xi + (s\tau\Delta_{SO} + \Delta)$ for $\delta > 0$, and $E = \xi - (s\tau\Delta_{SO} + \Delta)$ for $\delta < 0$. Taking the limit $\xi \to 0$, the following equation is obtained for the bottom of the conduction band

$$\left[\frac{p_x^2}{2m_{eff}} + \frac{(p_y + eA_y)^2}{2m_{eff}} + \frac{e\hbar v_F^2 B}{2\left(s\Delta_{SO} + \tau\Delta\right)}\right]\psi = \xi\psi, \tag{5.17}$$

where $m_{eff} = |s\tau\Delta_{SO} + \Delta|/v_F^2$ is the electron effective mass due to the band gap. This is the form of the Schrödinger equation in the presence of a magnetic field in which the emerging magnetic moments are obviously manifested. Once again, we see the duality of the orbital moments of the same nature as mentioned previously in the case of LLs: the moments are coupled to SOC through spin and to mass through the valley degree of freedom. Moreover, it is obvious that the expression for the magnetic moment is equal to the results of the low energy expansion given in Eq. (5.6). Having in mind that these moments effectively shift the low energy parabolic bands, one can use the same argument as in Ref. [132] to show that the separation between the lowest LL and the bottom of each *shifted* band is for each spin, valley and band to first order equal to half the separation between this and the first excited LL. This is in analogy with the LLs in a 2D massive-electron gas, where the lowest level sits at half the cyclotron frequency [132, 133]. The difference for higher energy LLs is a consequence of the deviation of the dispersion from the quadratic form.

5.4 Manifestation of orbital moments on magneto-transport

We proceed with considering how the emerging magnetic moments affect the transport properties. In particular, we analyze transport through a single 1D barrier in bulk graphene, extending from $x = 0$ up to $x = W$, and along the y direction, in which the intrinsic SOC is modified. The magnetic field is included only in the

barrier, so we choose the following vector potential (within the Landau gauge)

$$A_y = \begin{cases} 0 & x < 0 \\ Bx & 0 \leq x \leq W \\ BW & x > W \end{cases}. \tag{5.18}$$

The explicit derivation of the transmission coefficient is given in Appendix C.

Since we analyze a barrier made exclusively out of SOC, the valley degree of freedom plays no role in the electron transmission, which can be concluded from the theory presented in Sections 5.2 and 5.3. Therefore, the contour plots of the transmission coefficient $T = |t|^2$, for the two spin flavors, and for the 200-nm wide barrier as a function of energy and the incident angle of the incoming electron, are shown in Fig. 5.3. Each horizontal panel in this figure corresponds to a specific value of the magnetic field, which is 0, 0.1, 0.2 and 0.3 T from top to bottom. Because of the duality $\Delta_{SO} \leftrightarrow \Delta$ and $s \leftrightarrow \tau$, the results presented below also apply for transmission through a barrier when $\Delta \neq 0$ and $\Delta_{SO} = 0$. But for this case the spin and valley quantum numbers should be interchanged.

For both barrier types, we found that the magnetic field causes cyclotron motion, whose main feature is the appearance of a transmission window dependent on energy and incident angle ϕ [135, 136]. Outside of this window, the waves after the barrier become evanescent, and therefore no transmission takes place. This occurs when the longitudinal momentum $k'_x = \sqrt{\epsilon^2 - k'_y}$ of each electron state in the region after the barrier becomes imaginary. The transmission window is given by

$$\epsilon > \frac{\gamma}{1 - \sin\phi}, \tag{5.19}$$

where $\gamma = W/l_B^2$. The transmission windows for different B's are shown by solid black curves in Fig. 5.3.

When the magnetic field increases, the transmission asymmetry with respect to the incident angle becomes larger, due to the cyclotron motion, as shown in Fig. 5.3. Besides, whereas transmission coefficients are identical for both spins when no magnetic field is present, $T_\uparrow$ and $T_\downarrow$ differ when $B \neq 0$, which is a consequence of the SOC-induced magnetic moments. In fact, it is clear from Eq. (5.16) that a

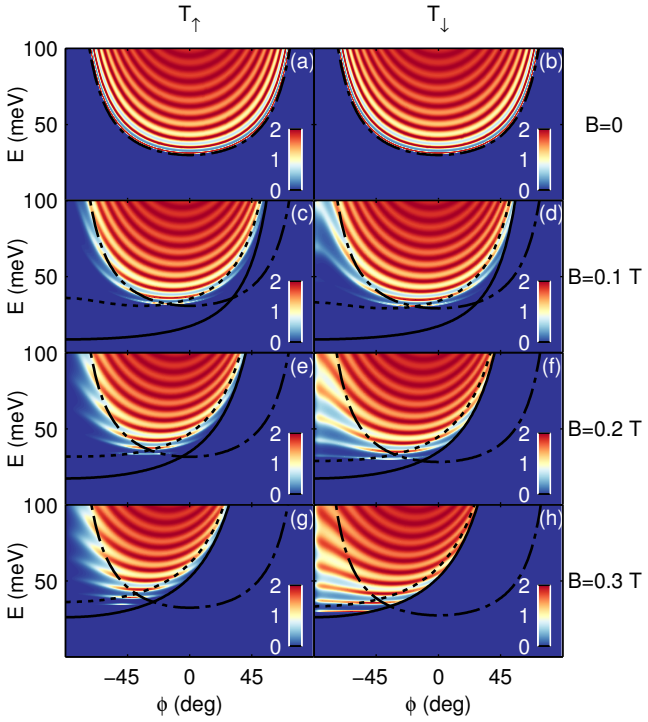

Figure 5.3: Contour plots of the transmission coefficient as function of incident angle and energy for $\Delta_{SO} = 30$ meV, $\Delta = 0$ and $W = 200$ nm. The magnetic field equals 0 T in (a-b), 0.1 T in (c-d), 0.2 T in (e-f), and 0.3 T in (g-h). The results are shown for both spin orientations. The semiclassical critical boundaries ϵ_{cr0} and ϵ_{crW} are depicted by dash-dotted and dotted lines, respectively.

quasi-classical longitudinal momentum q_x

$$q_x(x) = \sqrt{\epsilon^2 - \delta^2 - (k_y + x/l_B^2)^2 - s/l_B^2} \tag{5.20}$$

can be assigned to the sublattice-polarized states.

In order to understand the effects of the emerging magnetic moments on the transmission characteristics, it is instructive to investigate how classical turning points vary with ϵ and ϕ. Those turning points are extracted from $q_x(x) = 0$, where q_x is given by Eq. (5.20), and are given by

$$x_{1,2} = -\epsilon l_B^2 \sin\phi \mp l_B^2 \sqrt{\epsilon^2 - \delta^2 - \mu}, \tag{5.21}$$

where $\mu = s/l_B^2$ is the magnetic moment term which appears in the expression for the quasi-classical momentum in Eq. (5.20). Given that the barrier extends from 0 to W, the condition that no turning points are found within the barrier is obtained

by requiring $x_1 < 0$ and $x_2 > W$. The former condition leads to

$$x_1 < 0 \Rightarrow \begin{cases} \epsilon > \frac{\sqrt{\delta^2+\mu}}{\cos\phi}, & \phi < 0 \\ \epsilon > \sqrt{\delta^2+\mu}, & \phi > 0 \end{cases}, \tag{5.22}$$

while the latter results in

$$x_2 > W \Rightarrow \begin{cases} \epsilon > \sqrt{\delta^2+\mu}, & \epsilon\sin\phi+\gamma < 0 \\ \epsilon > \frac{\gamma\sin\phi+\sqrt{\gamma^2+(\delta^2+\mu)\cos^2\phi}}{\cos^2\phi}, & \epsilon\sin\phi+\gamma > 0 \end{cases}. \tag{5.23}$$

On the other hand, both classically forbidden and classically allowed regions will be present in the barrier if $0 < x_1 < x_2 < W$. The two extreme cases of vanishing allowed regions occur when the leftmost turning point approaches the right interface of the barrier

$$x_1 < W \Rightarrow \begin{cases} \epsilon > \frac{\gamma\sin\phi+\sqrt{\gamma^2+(\delta^2+\mu)\cos^2\phi}}{\cos^2\phi}, & \epsilon\sin\phi+\gamma < 0 \\ \epsilon > \sqrt{\delta^2+\mu}, & \epsilon\sin\phi+\gamma > 0 \end{cases}, \tag{5.24}$$

and when the rightmost turning point approaches the left barrier interface

$$x_2 > 0 \Rightarrow \begin{cases} \epsilon > \sqrt{\delta^2+\mu}, & \phi < 0 \\ \epsilon > \frac{\sqrt{\delta^2+\mu}}{\cos\phi}, & \phi > 0 \end{cases}. \tag{5.25}$$

From the angle dependent functions in the last four relations one might define the critical energies

$$\epsilon_{cr0} = \frac{\sqrt{\delta^2+\mu}}{\cos\phi}, \tag{5.26}$$

and

$$\epsilon_{crW} = \frac{\gamma\sin\phi+\sqrt{\gamma^2+(\delta^2+\mu)\cos^2\phi}}{\cos^2\phi}, \tag{5.27}$$

for which the classical turning points are located exactly at the two interfaces, i.e. they are obtained by solving $q_x(0) = 0$ and $q_x(W) = 0$, respectively. Those critical boundaries are plotted as dash-dotted and dotted curves in Fig. 5.3.

In order to elucidate the quasi-classical behavior, in Fig. 5.4(a) we plot the zones corresponding to different configurations of turning points by different colors. The same set of parameters is used as in Fig. 5.3(e) ($\Delta_{SO} = 30$ meV, $W = 200$ nm, $B = 0.2$ T and $s = +1$). In Fig. 5.4(b) we plot a set of classical trajectories that

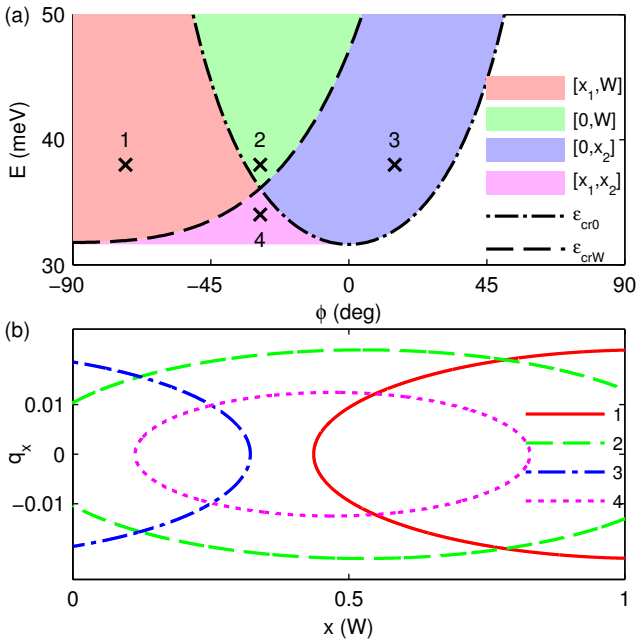

Figure 5.4: (a) The regions with different ranges of turning points for $W = 200$ nm, $\Delta_{SO} = 30$ meV, $\Delta = 0$, and $B = 0.2$ T. Different classically allowed trajectories are found in differently shaded regions, demarcated by the two critical boundaries. (b) A family of four different classical trajectories which correspond to the states labeled by numbered crosses in each region of (a).

correspond to the zones shown in Fig. 5.4(a). As could be inferred from Fig. 5.4, for ϵ larger than both ϵ_{cr0} and ϵ_{crW} (green colored region in Fig. 5.4(a)), there is no classically forbidden region inside the barrier. However, if the electron energy is between the two critical energies (red or blue colored region in Fig. 5.4(a)), a classically forbidden energy range will appear on either end of the barrier. In other words, the electron will have to tunnel through a part of the barrier adjacent to one of its interfaces, whereas propagation is free in the other part. For the most extreme case displayed as the magenta colored region in Fig. 5.4(a), the electron has to tunnel through both ends of the barrier.

One may notice that the two critical energies whose variation with ϕ is depicted by dash-dotted and dotted lines in Fig. 5.3 are almost identical for the two spins. Also, by careful inspection of Fig. 5.3 it becomes evident that the quasi-classical zones we derived explain the observed transmission very well, especially for the spin up states. For the spin down states, however, transmission is enhanced with respect to the spin up states in the zones for which the electron waves must tunnel through a region of the barrier (the red and blue energy zones in Fig. 5.4(a)). This could be understood if one recalls that the WKB expression for the tunneling coefficient

is given by

$$T \approx e^{-2Im\int q_x(x)dx}, \tag{5.28}$$

where the integration is over a classically forbidden region. Having this in mind, it is obvious that for $\Delta_{SOC} \neq 0$ and $B \neq 0$ spin-up states decay faster than the spin-down states in classically forbidden regions, due to the paramagnetic term. This difference increases at higher magnetic fields, which leads to a growing contrast between the transmission coefficients for the two spins, as Fig. 5.3 clearly demonstrates. When the magnetic field is absent, the emerging paramagnetism vanishes, and therefore, the transmission characteristics for the two spins are identical (see Figs. 5.3(a) and (b)).

Next, we explore how the presence of the magnetic moments affects the interference pattern shown in Fig. 5.3. This could be the most important effect from a practical point of view. In the Fabry-Perot model, the interference pattern depends on the phase the electron wave function accumulates between the barrier interfaces and the bounces from the interface(s) and/or turning point(s)

$$\alpha = \alpha_{WKB} + \alpha_1 + \alpha_2, \tag{5.29}$$

where α_1 and α_2 are the backreflection phases, whereas α_{WKB} is the WKB phase

$$\alpha_{WKB} = 2\int_{\max(0,x_1)}^{\min(W,x_2)} q_x\left(x\right)dx. \tag{5.30}$$

To analyze how the orbital magnetic moments influence the fringe pattern we could once again invoke Eq. (5.20) and the associated diagram in Fig. 5.4. It follows that Fabry-Perot resonances have different character in the different zones. Whenever $B \neq 0$, the WKB phase is accumulated throughout the entire barrier for $\epsilon > \max\left(\epsilon_{cr0}, \epsilon_{crW}\right)$, but only in region $[x_1, W]$ for $\epsilon_{cr0} > \epsilon > \epsilon_{crW}$ (the red-shaded region in Fig. 5.4(a)). Consequently, in the latter case the transmission maxima (depicted by the red color in Fig. 5.3) are almost linear functions of ϕ, whereas in the former case their dependence on ϕ is nonlinear.

The crucial point, however, is that the phase accumulated during the propagation differs for the different spin orientations. This occurs because magnetic moments associated with opposite spins contribute to α_{WKB} in opposite ways (see Eq. (5.20)). To see this clearly, and to provide experimentally verifiable predictions it is important to consider the conductivity of the entire studied structure, given as

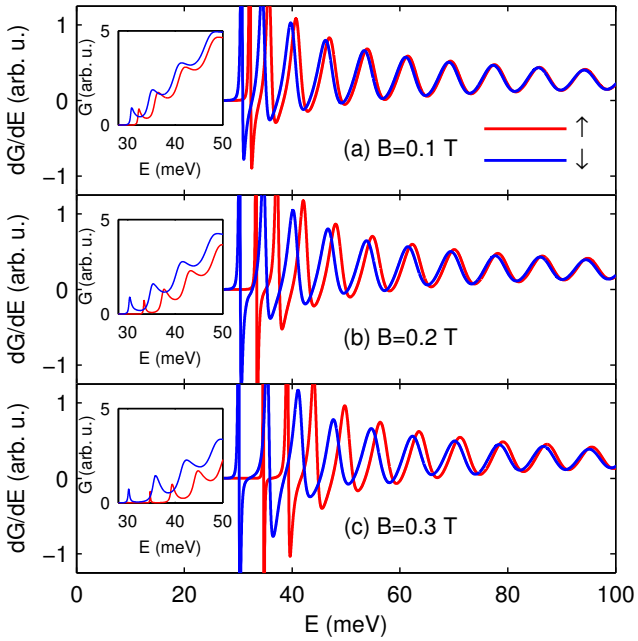

Figure 5.5: The derivative of the conductance versus incident energy, for (a) 0.1 T, (b) 0.2 T, and (c) 0.3 T. All other parameters are the same as in Fig. 5.3. Insets show the variation of the conductance with incident energy for the corresponding magnetic field.

[137],

$$G(\epsilon) = G_0 \int_{-\pi/2}^{\pi/2} T(\epsilon, \phi)\, \epsilon \cos\phi d\phi, \tag{5.31}$$

where $G_0 = e^2 L/2\hbar\pi^2$, with L denoting the lateral width of the entire structure in the y direction.

Since the effects of magnetic moments are most vividly manifested in the dependence of dG/dE on energy, we display this quantity in Fig. 5.5, for the same set of parameters as in Fig. 5.3. Alongside with dG/dE, the corresponding conductance is shown in the insets for each case. As can be seen from these insets, G only depicts the fact that the spin-down conductance is increased with respect to the spin-up conductance, due to the enhanced transmission through the classically forbidden regions, as already discussed. On the other hand, the first derivative of the conductance with respect to energy conveys the information of the interference pattern, where the effects of the orbital moments are more transparent. Two issues are of importance here: (i) The difference between the two spins is clearly more pronounced at higher magnetic fields. This happens because in such a case the orbital moments have a larger impact on the electron dynamics, as pointed out before. (ii)

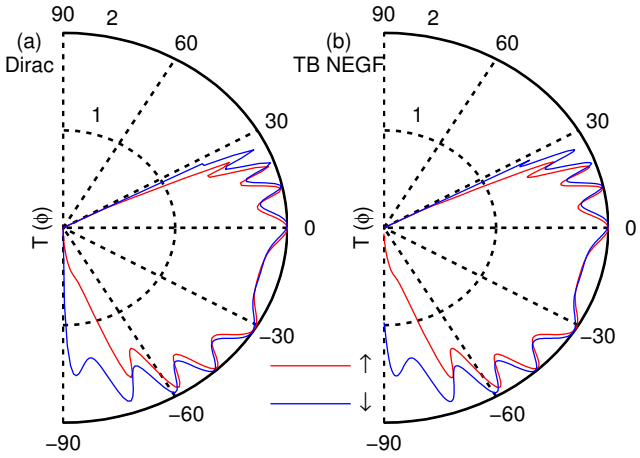

Figure 5.6: Transmission curves calculated using (a) the continuum and (b) the TB NEGF method. The parameters are $W = 200$ nm, $B = 0.3$ T, and $E = 100$ meV.

The distinction between the two spins is more prominent at lower energies. This is a consequence of the larger emerging orbital magnetic moments of the electrons whose energies are close to the band edges than of more energetic electrons, as Eq. (5.4) and Fig. 5.1(a) demonstrate.

Finally, we would like to point out that the manifestation of orbital moments in transport properties can be captured by the tight-binding nonequilibrium Green function formalism as well. To show this, in Fig. 5.6(a) we plot a set of transmission curves obtained using the derived transmission amplitude, while in Fig. 5.6(b) we plot the results of our numerical transport simulations within the TB NEGF method, for the same barrier parameters. The phenomenological model used to describe graphene in this case is the Kane-Mele tight-binding model discussed in detail in Chapter 1:

$$H = -t \sum_{\langle i,j\rangle,\alpha} e^{i\varphi_{ij}} c^{\dagger}_{i\alpha} c_{j\alpha} + i\lambda_{SO} \sum_{\langle\langle i,j\rangle\rangle,\alpha,\beta} \nu_{ij} e^{i\varphi_{ij}} c^{\dagger}_{i\alpha} s^{z}_{\alpha\beta} c_{j\beta}. \tag{5.32}$$

The first term describes the usual hopping between nearest neighbor p_z orbitals in graphene, which extends beyond the barrier. The second term describes the intrinsic spin-orbit interaction found in the barrier, through the next-nearest-neighbor hopping amplitude λ_{SO} ($\Delta_{SO} = 3\sqrt{3}\lambda_{SO}$). Note that ν_{ij} determines the sign of the hopping; it is positive (negative) if an electron makes a right (left) turn at the intermediate atom in hopping from site j to site i. The Peierls term $\varphi_{ij} = \frac{e}{\hbar}\int_{\mathbf{r_i}}^{\mathbf{r_j}} \mathbf{A}\cdot d\mathbf{l}$ accounts for the phase the electron acquires while traveling in the presence of the magnetic field. The details of the NEGF procedure were laid out in Chapter 2.

In order to compare the results with the continuum theory, we need the numerical simulations within the NEGF formalism to provide us with the angular dependence of the transmission through a structure infinite in the y-direction. To achieve this, we resort to the recipe described in Ref. [138]. In short, we take the narrowest possible zigzag nanoribbon, placed along the x-direction, where the semi-infinite left and right leads surround the barrier region in which SOC NNN hopping is nonzero. The structure is then taken to be periodic along the y-direction, prompting the use of the Bloch theorem in this direction. This means that the phase factor will enter all hopping terms along the y axis, which is none other than the transverse momentum k_y. In this way, k_y appears as a parameter, and since the incident energy E is a parameter as well, one is then able to reconstruct the angle of propagation using $\hbar v_F k_y = E \sin\phi$. Note that in our case, besides the Peierls phase factor, we must also add the vector potential, Eq. (5.18), to k_y, in order to properly model the influence of the magnetic field. Finally, one needs to connect the Fermi velocity v_F entering the Dirac equation, with the nearest-neighbor hopping t, as $v_F = 3ta/2\hbar$, where $a = 0.142$ nm is the carbon-carbon distance, and the hopping is as usual set to $t = 2.7$ eV.

Although the continuum and the TB NEGF schemes differ substantially as far as the formalism and implementation are concerned, they give practically indistinguishable results. This is not surprising, having in mind that the continuum Dirac picture is the effective theory corresponding to the low energy tight-binding method. Therefore, both approaches display these Zeeman-type effects, even though we use only minimal coupling and the Peierls substitution, to account for the influence of the magnetic field. Since strain in honeycomb lattices effectively induces time-reversal invariant pseudomagnetic fields [139], stretching of insulating Dirac monolayers will inevitable galvanize orbital moments as well [136].

Finally, note that the TB NEGF method could prove handy for studying the effects of disorder and imperfections on the manifestation of the spin-contrasting orbital moments. However, unlike the orbital moments coupled to the spin, the valley-contrasting orbital moments can not be distinguished by the TB NEGF transport simulations, since the contributions from the two valleys are inherently summed together, and cannot be separated. In this case, only the continuum calculations, where the valley degree of freedom is explicit, can elucidate the underlying physics.

Chapter 6

Spin-valley filtering in strained graphene heterostructures

6.1 Introduction

Graphene is considered a promising material for future spintronic applications, in part due to its long spin relaxation length [140–142]. Furthermore, owing to its band structure with two inequivalent valleys, K and K', it has revived the field of valleytronics [18, 143]. The low energy excitations in the two valleys behave as Dirac-Weyl particles, which is most famously manifested in the presence of a magnetic field, in which Landau levels scale as $\sqrt{B}$, with a unique level at zero energy [18, 56]. Besides, it is known that straining graphene causes time-reversal invariant gauge fields to appear, i.e. an effective magnetic field with opposite signs in opposite valleys, providing a tool for manipulating the valley degree of freedom [18]. Recent experiments demonstrated large values of this pseudomagnetic field, which could hardly be matched in practical applications by real magnetic fields [144].

In this chapter we study the transmission through a thin 1D graphene barrier with artificially induced mass and spin-orbit coupling, in the presence of pseudomagnetic field using the continuum approach. The motivation for studying such a structure is twofold. In part it is due to a shift to a new paradigm in 2D materials research, whereby their properties are custom tailored according to specific needs by stacking different 2D crystals on top of each other. These are the so called van der Waals heterostructures, also discussed in the previous chapter [145]. More importantly, and in the light of this paradigm, recent theoretical and experimental work shows that mass and SOC, which are vanishing in intrinsic graphene, could

be induced with appropriate substrates and/or adatom deposition [66, 95, 98, 99, 146–152]. We will show that the studied device behaves as a spin-valley filter, thus laying in the intersection of the fields of spintronics and valleytronics.

6.2 Pseudomagnetic field in strained honeycomb lattices

First we derive the low energy Hamiltonian of strained graphene starting from tight binding picture. The simplest such procedure takes into account the variation of the hopping integral as a function of the stretching of the bonds. When a deformation of the nearest neighbor bonds from equilibrium occurs, the hopping amplitude changes according to $te^{-\beta\Delta u_n}$, where $\beta \approx 3$ is a material parameter, $\Delta u_n = |\delta'|/a - 1$ is a relative distance change and $|\delta'|$ is the non-equilibrium NN distance [153–155].

On the other hand, any distortion of the lattice can be captured by the displacement or deformation field $\mathbf{u} = (u_x, u_y)$, connecting the deformed lattice coordinates $\mathbf{r}'_i$ with the undeformed ones $\mathbf{r}_i$, through $\mathbf{r}'_i(\mathbf{r}_i) = \mathbf{r}_i + \mathbf{u}(\mathbf{r}_i)$. In the case of homogenous strain, which is considered here for simplicity, there can only be three distinct hopping amplitudes, corresponding to the three neighbors surrounding a given atom. Referring back to Chapter 1 and Fig. 1.1, the three different undeformed NN vectors pointing from an A atom to a B atom are

$$\delta_0 = a(0, 1), \tag{6.1}$$

$$\delta_1 = a\left(-\frac{\sqrt{3}}{2}, -\frac{1}{2}\right), \tag{6.2}$$

$$\delta_2 = a\left(+\frac{\sqrt{3}}{2}, -\frac{1}{2}\right). \tag{6.3}$$

Then, up to linear terms, the non-equilibrium NN vectors read

$$\delta'_n(\mathbf{r}) \approx \delta_n + (\delta_n \cdot \nabla)\mathbf{u}(\mathbf{r}). \tag{6.4}$$

The magnitude of δ_n is then

$$|\delta'_n| = a\sqrt{1 + \frac{2\delta_{nx}^2 u_{xx} + 2\delta_{ny}^2 u_{yy} + 4\delta_{nx}\delta_{ny}u_{xy}}{a^2}}, \tag{6.5}$$

where $u_{ij} = \frac{1}{2}(\partial_i u_j + \partial_j u_i)$ are the components of the strain tensor. Expanding the

root up to the linear terms yields the relative distance change

$$\Delta u_n \approx \frac{\delta_{nx}^2 u_{xx} + \delta_{ny}^2 u_{yy} + 2\delta_{nx}\delta_{ny} u_{xy}}{a^2}. \tag{6.6}$$

Having established this, we can go on to Fourier transforming the TB Hamiltonian, as in Chapter 1. However, in this procedure we shall use the equilibrium lattice sites and, thus, the effects of strain will only be incorporated through the modification of the hopping amplitude. Also, in the spirit of the entire derivation, the modification of the hopping amplitude will only enter the Hamiltonian up to first order. Then, the matrix element $\gamma(\mathbf{k})$ defined in Chapter 1 reads

$$\gamma(\mathbf{k}) = -t\left[1 - \beta\Delta u_0 + (1 - \beta\Delta u_1)\, e^{-i\mathbf{k}\cdot\mathbf{a}_1} + (1 - \beta\Delta u_2)\, e^{-i\mathbf{k}\cdot\mathbf{a}_2}\right]. \tag{6.7}$$

Finally, expanding the Hamiltonian around the $\mathbf{K}_\tau = \left(\tau\frac{4\pi}{3\sqrt{3}a}, 0\right)$ points, and keeping only the terms linear in either real space or momentum space displacement, one obtains the effective low-energy description

$$H = v_F\left[\tau\left(p_x + eA_x\right)\sigma_x + \left(p_y + eA_y\right)\sigma_y\right], \tag{6.8}$$

where

$$A_x = -\tau\frac{\hbar\beta}{2ea}\left(u_{xx} - u_{yy}\right), \quad A_y = \tau\frac{\hbar\beta}{ea}u_{xy}. \tag{6.9}$$

It is clear from this that small strains in graphene manifest themselves through vector potentials in the Dirac-Weyl equation [156, 157]. Moreover, the resulting pseudomagnetic fields are opposite in opposite valleys, as can be seen in Eq. (6.9), therefore preserving the time-reversal symmetry of the system.

A few comments are in order, before we explore the possible applications of this phenomenon in the subsequent section. Besides the appearance of the pseudomagnetic field, higher order expansions uncover the renormalization of the Fermi velocity, which becomes position-dependent [158]. On the other hand, including the actual positions of the displaced atomic sites in the calculations does not have an impact on the pseudomagnetic field [159–161]. It does, however, induce other terms, which we will ignore for simplicity.

6.3 Spin-valley filtering

In the continuum approach the carrier mass is captured by a staggered potential term Δ, while SOC is captured by a mass-like term Δ_{SO}. The presence of both will result in a competition to open topologically distinct gaps [9]. This competition reflects on the bulk band gap given by $2\left|s\tau\Delta_{SO}+\Delta\right|$, where $s=+1/-1$ labels the spin $\uparrow/\downarrow$ and $\tau=+1/-1$ labels the valley K/K' degrees of freedom [162]. Thus, for different spin-valleys different gaps can arise. In order to get some insight into the problem, we will first study transmission through a barrier with a real magnetic field. As can be expected, regardless of the magnetic field, whenever $\Delta_{SO}\neq 0$ and $\Delta\neq 0$, there is an energy range where $s\tau=+1$ states are suppressed, while $s\tau=-1$ states are not. In other words only one spin from one valley, and the opposite spin from the opposite valley are transmitted. The main effect of the magnetic field is to impose restrictions on incident angles over which the transmission can occur. This is caused by the cyclotron orbits, which are the same for all spins and valleys.

We subsequently apply the pseudomagnetic field, which leads to the reversal of the effective field, and the effective cyclotron orbits in one of the valleys. This provides the benefit of spatially separating the transmitted states according to their valley degree of freedom, and accordingly their spin degree of freedom as well. Thus a combined spin-valley filter can be obtained. Furthermore, we show that chemical potential and strain can act as a switch, rendering control over the filtering behavior. Filtering behavior in graphene devices was studied before [163–171], however the mechanism proposed in this chapter is novel, and previously unexplored. Practical implications are discussed at the end of the chapter.

Our starting point is the Dirac-Weyl equation, in the presence of mass, SOC, and a magnetic field perpendicular to the sheet, B_z. In this case we choose the Landau gauge $\mathbf{A}=(0,A_y)$, and the Dirac-Weyl Hamiltonian reads

$$H=\hbar v_F\left[\tau k_x\sigma_x+(k_y+\frac{e}{\hbar}A_y)\sigma_y\right]+s\tau\Delta_{SO}\sigma_z+\Delta\sigma_z, \tag{6.10}$$

where v_F is the Fermi velocity, and σ_z is a Pauli matrix operating in the sublattice subspace.

We use the parameter τ_B, such that $B_z=\tau_B B$, to capture the valley-dependent nature of the pseudomagnetic field. Setting $\tau_B=+1$ models the influence of the real magnetic field, while $\tau_B=\pm\tau$ models the two types of the pseudomagnetic field. Including the (pseudo)magnetic field only in the barrier of width W means that the

magnetic vector potential is given by

$$A_y = \begin{cases} 0, & x < 0 \\ \tau_B B x, & 0 \leq x \leq W \\ \tau_B B W, & x > W \end{cases}. \tag{6.11}$$

In the chosen Landau gauge k_y is a good quantum number and the solutions have the form $\Psi(x,y) = \exp(ik_y y)\,(\psi_A(x), \psi_B(x))^T$. Introducing $\hbar v_F \epsilon = E$, and $\hbar v_F \delta = s\tau\Delta_{SO} + \Delta$, and decoupling the system, in the barrier one obtains

$$\left[\partial_x^2 \mp \tau\tau_B \frac{1}{l_B^2} - (k_y + \tau_B \frac{x}{l_B^2})^2 + \epsilon^2 - \delta^2\right] \psi_{A/B} = 0, \tag{6.12}$$

where $l_B = \sqrt{\hbar/eB}$. Using the transformation $z = \sqrt{2}\,(k_y l_B + \tau_B x/l_B)$, the solutions are expressed in terms of the parabolic cylinder functions $D_\nu(z)$ (see Appendix C for a detailed derivation), and read

$$\psi_{II} = C_1 \begin{pmatrix} D_{\nu_A}(z) \\ g D_{\nu_B}(z) \end{pmatrix} + C_2 \begin{pmatrix} D_{\nu_A}(-z) \\ -g D_{\nu_B}(-z) \end{pmatrix}, \tag{6.13}$$

where $\nu_{A/B} = (\epsilon^2 - \delta^2)\, l_B^2/2 \mp \tau\tau_B/2 - 1/2$, and

$$g = i \left[\frac{\sqrt{2}}{(\epsilon + \tau\tau_B\delta)\, l_B}\right]^{\tau\tau_B}. \tag{6.14}$$

On the other hand, the incident wave function is

$$\psi_I = e^{ik_x x} \begin{pmatrix} 1 \\ \tau e^{i\tau\phi} \end{pmatrix} + r e^{-ik_x x} \begin{pmatrix} 1 \\ \tau e^{i\tau(\pi-\phi)} \end{pmatrix}, \tag{6.15}$$

while the solution in the third region reads

$$\psi_{III} = t\sqrt{\frac{k_x}{k_x'}} e^{ik_x' x} \begin{pmatrix} 1 \\ \tau e^{i\tau\theta} \end{pmatrix}. \tag{6.16}$$

Here, $\phi = \arctan k_y/k_x$ and $\theta = \arctan k_y'/k_x'$ denote the energy propagation directions before and after the barrier, where $k_y = q_y(0)$ and $k_y' = q_y(W)$, while $q_y(x) = \epsilon \sin\phi + eA(x)/\hbar$ is the effective transverse momentum. The longitudinal momenta before and after the barrier are given by $k_x = \epsilon\cos\phi$ and $k_x' = \epsilon\cos\theta$. Note that all these expressions are valid for the valence band as well. Matching the wave functions at the interfaces gives a system of equations, whose solution yields

the transmission amplitude t

$$t = \frac{2g\tau\cos\phi\left(G_A^+G_B^- + G_A^-G_B^+\right)}{e^{ik_x'W}f}\sqrt{\frac{k_x'}{k_x}}, \tag{6.17}$$

where

$$\begin{aligned} f = g^2\left(F_B^+G_B^- - F_B^-G_B^+\right) + e^{i\tau(\theta-\phi)}\left(F_A^+G_A^- - F_A^-G_A^+\right) \\ +g\tau e^{i\tau\theta}\left(F_B^-G_A^+ + F_B^+G_A^-\right) + g\tau e^{-i\tau\phi}\left(F_A^+G_B^- + F_A^-G_B^+\right). \end{aligned} \tag{6.18}$$

Here the coefficients $F^{\pm}$ and $G^{\pm}$ are given by

$$F_{A/B}^{\pm} = D_{\nu_{A/B}}\left[\pm\sqrt{2}k_y l_B\right], \tag{6.19}$$

$$G_{A/B}^{\pm} = D_{\nu_{A/B}}\left[\pm\sqrt{2}\left(k_y l_B + \tau_B\frac{W}{l_B}\right)\right]. \tag{6.20}$$

In Fig. 6.1 we look at the behavior of transmission coefficients ($T = |t|^2$) in detail for a real magnetic field ($\tau_B = +1$). Here we show contour plots of, from top to bottom, $T_{\uparrow K}$, $T_{\uparrow K'}$, $T_{\downarrow K}$ and $T_{\downarrow K'}$, as a function of incident energy and angle. We adopt a set of parameters that illustrates our main points clearly: $\Delta_{SO} = 30$ meV, $W = 100$ nm and $B = 0.2$ T, whereas Δ varies from 0 in (a), to $\Delta = 15$ meV in (b) and $\Delta = 30$ meV in (c).

A common feature of all the cases depicted in Fig. 6.1 is that transmission is forbidden outside the transmission window delineated by the solid black line, akin to the scenario of the previous chapter. This is because the magnetic field enforces cyclotron motion, resulting in asymmetric transmission curves with respect to the incidence angle [135, 172]. This boundary is obtained by requiring that the longitudinal momentum after the barrier becomes imaginary, so that only evanescent waves can exit, and therefore no transmission can occur. The longitudinal momentum in the third region is given by $k_x'^2 = \epsilon^2 - q_y\left(W\right)^2$. Hence, this window is determined by a critical energy, below (above) which the transmission is not possible

$$\epsilon_{cr1}^{c/v} = \frac{\pm\gamma}{1 \mp \tau_B\sin\phi}, \tag{6.21}$$

where $\gamma = W/l_B^2$, and c (v) denotes conduction (valence) band. This window depends solely on W, B and ϕ, i.e. it is not a function of Δ_{SO}, Δ, s or τ at all, as can be observed in Fig. 6.1. However, the transmission within this window obviously depends on Δ_{SO}, Δ, s and τ.

As already mentioned, in the presence of mass and SOC, the bulk band gap is given by $2\left|s\tau\Delta_{SO}+\Delta\right|$. Therefore, when both parameters are present, the $s\tau=+1$ states experience a larger gap than the $s\tau=-1$ states. To see how this might reflect on the transmission through a barrier we need to examine the behavior of the quasiclassical momentum within the barrier $q_x\left(x\right)=\sqrt{\epsilon^2-\delta^2-q_y\left(x\right)^2}$. Therefore, through the appearance of δ, the quasiclassical momentum depends on Δ_{SO},Δ,s and τ. More specifically, when both Δ and Δ_{SO} are nonzero, whether classically forbidden regions inside the barrier will appear depends crucially on the product $s\tau$, which is a clear manifestation of the bulk band gap. The existence of forbidden regions in the barrier does not necessarily imply that the momentum after the barrier is imaginary. To see this, one can express the critical energy below (above) which the former happens

$$\epsilon_{cr2}^{c/v}=\pm\max\left(\frac{\pm\tau_B\gamma\sin\phi+\sqrt{\gamma^2+\delta^2\cos^2\phi}}{\cos^2\phi},\frac{\left|\delta\right|}{\cos\phi}\right). \tag{6.22}$$

This critical boundary is drawn in dashed black lines in Fig 6.1, and it coincides with the transmission window (Eq. (6.21)) only when the bulk band gap is closed. Therefore, in between ϵ_{cr1}^{c} and ϵ_{cr2}^{c} the transmission is possible, but only by tunneling through forbidden region (regions) in the barrier, and thus perfect transmission cannot occur. Above ϵ_{cr2}^{c} boundary, however, there is no attenuation within the barrier, and the resulting transmission is determined by the interference of electron waves. It is important to point out that below the minimum of ϵ_{cr2}^{c}, which coincides with the bottom of the conduction band, the transmission is strongly suppressed.

One issue requires clarification. For the case $\Delta=0$, shown in column (a), ϵ_{cr2}^{c} is the same for all spin and valley flavors. However, the transmissions for spin up and spin down are obviously different. This discrepancy arises numerically due to the factor g, appearing in the transmission amplitude, Eq. (6.17). This factor is in turn just a reflection of the form of the Landau level eigenstates (see Appendix C). In fact one can easily show that the solution given by Eq. (6.13) reduces to the LL eigenstates once the incident energy is equal to a particular LL.

The true reason for this discrepancy however lies in the orbital magnetic moments which arise for massive Dirac fermions. It is known that inversion symmetry breaking can lead to the appearance of magnetic moments coupled with the valley degree of freedom, which in turn influence the LLs [109]. Analogous moments arise when SOC is present as well, albeit coupled with the spin degree of freedom. These spin-

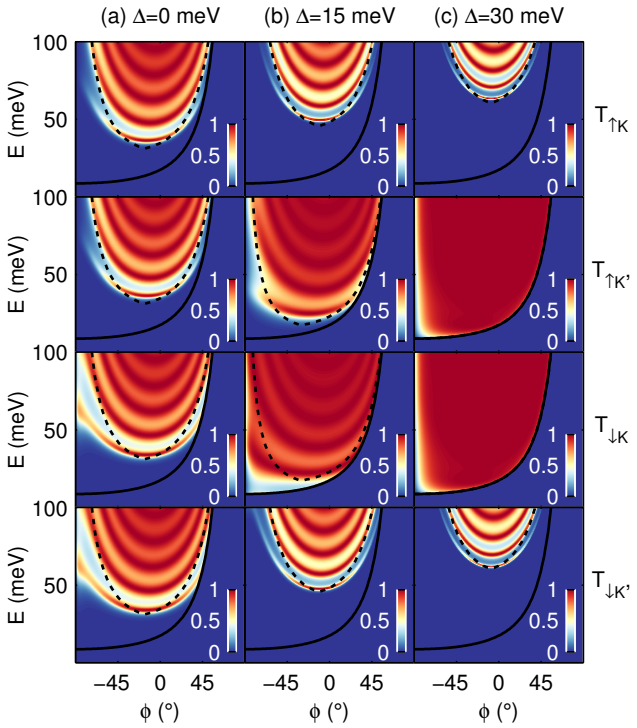

Figure 6.1: Contour plots of transmission coefficient versus energy and incident angle, for all spin and valley flavors. Δ_{SO} equals 30 meV, while Δ varies: in (a) $\Delta = 0$, (b) $\Delta = 15$ meV and (c) $\Delta = 30$ meV. The width of the barrier is taken to be $W = 100$ nm, and $B = 0.2$ T.

contrasting magnetic moments were thoroughly studied in Chapter 5. It is these moments that cause spin-distinguished transmission found in Fig. 6.1(a). A similar behavior occurs when only Δ is nonzero, but with valley differentiation instead. In fact, we have found that all of the contour plots obey the symmetry $\Delta_{SO} \leftrightarrow \Delta$, $s \leftrightarrow \tau$. This stems from the fact that the band gap and the magnetic moments display the same symmetry as well (see Chapter 5). We stress however that this behavior has little to no impact on the effect we describe here.

Introducing Δ will cause shrinking/enlarging of the evanescent region for $s\tau = -1/+1$, column (b). This will lead to the appearance of an energy range where only $s\tau = -1$ states are not suppressed. Furthermore note that these states also experience lower fringe contrast. This is because the effective gap in the barrier is now reduced for these states. Finally, for the case $\Delta_{SO} = \Delta$, depicted in column (c), $s\tau = +1$ states are even further suppressed. On the other hand, for $s\tau = -1$ the band gap in the barrier becomes zero, and the effective dispersion returns to a Dirac cone. These states are transmitted as if there was only a magnetic field barrier in bulk graphene [135, 172], which can also be inferred from the fact that

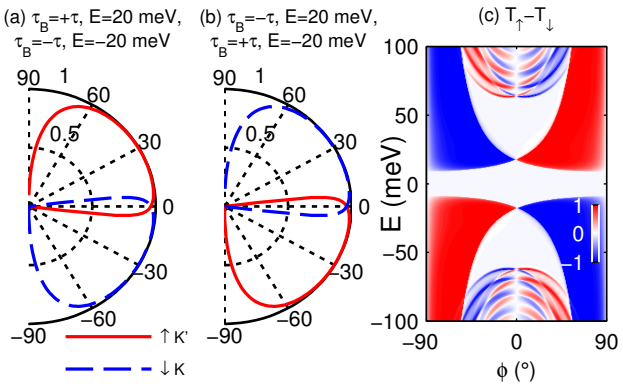

Figure 6.2: Polar plots of the transmission coefficient versus the incident angle for various strains and energies. In (a) $\tau_B = \pm\tau$, $E = \pm 20$ meV give the same transmission, while in (b) $\tau_B = \mp\tau$, $E = \pm 20$ meV give the same transmission. All other parameters are the same as in Fig. 6.1(c). The electric control of the spin-valley filtering is clearly seen in (c), where the contour plot of $T_\uparrow - T_\downarrow$ is shown.

now $\epsilon^{c/v}_{cr1} = \epsilon^{c/v}_{cr2}$. This means that they experience no reflection at the walls of the barrier and as a consequence there are no resonances.

Therefore, as long as $\Delta_{SO} \neq 0$ and $\Delta \neq 0$, in a particular energy range only spin up states from the K valley and spin down states from the K' valley are transmitted. Introducing pseudomagnetic field, by for instance setting $\tau_B = +\tau$, means that the effective magnetic field in K' valley flips. This in turn flips the transmission window in this valley to $\epsilon^{c}_{cr1K'} = \gamma/\left(1 + \sin\phi\right)$. Thus, spatial separation of the states from each valley will occur, which is an obvious consequence of their opposite cyclotron trajectories. Furthermore, since spin is coupled to the valley degree of freedom in the transmitted states, this will inevitably lead to spin separation as well.

Additionally, it follows from Eq. (6.17) that the transmission coefficient for $-\phi$, $-s$, $-\tau$ equals the one for ϕ, s, τ, which is a manifestation of time reversal symmetry.[1] In other words, the transmission for spins in the valley where the effective magnetic field is reversed, will just be a mirror image of the transmission from the opposite valley and opposite spin, for which the effective magnetic field stayed the same. This is displayed in Fig. 6.2(a), for the same set of parameters as in Fig. 6.1(c), and $E = 20$ meV, where the spin-valley filtering behavior is apparent. On the other hand, by choosing the opposite strain, $\tau_B = -\tau$, the effective magnetic field will be flipped in both valleys. This will lead to flipping of the filtered spin and valley, as depicted in Fig. 6.2(b), since both transmission windows flip (see Eq.

[1]It can easily be established that $T\left(\theta\right) = T\left(-\phi\right)$, allowing a straightforward interpretation of Fig. 6.2 in terms of the exiting angle as well.

(6.21)). In other words strain could act as a switch.[1]

Furthermore, the switching can also be achieved by controlling the chemical potential instead of strain. To see this, note that the transmission window for a given spin and valley in the valence band ϵ^v_{cr1} is a mirror reverse of the one in the conduction band ϵ^c_{cr1}, Eq. (6.21). This is a consequence of different cyclotron trajectories for electrons and holes, and the same symmetry is obeyed by the semiclassical critical boundary, given in Eq. (6.22). Moreover, since $T(\epsilon, \tau_B = +\tau) = T(-\epsilon, \tau_B = -\tau)$ holds, Figs. 6.2(a) and (b) also correspond to $\tau_B = -\tau$, $E = -20$ meV and $\tau_B = \tau$, $E = -20$ meV, respectively. The effect of controlling the chemical potential on spin filtering is depicted in Fig. 6.2(c), where the outlines of the transmission windows can be clearly seen. Note that the same plot holds for $T_{K'} - T_K$, albeit with opposite filtering in the overlap region of both transmission windows. Therefore, the control of the transmitted spin-valley outside of the transmissionless gap $[-\gamma/2, \gamma/2]$ could be established by means of electrical gating. Additionally, there exist optimal energy ranges for filtering in the valence and conduction band, $[-\gamma, -\gamma/2]$ and $[\gamma/2, \gamma]$, respectively, where the transmitted states do not overlap.

Finally, let us conclude with some practical considerations. First note that only minor straining would be required for inducing pseudomagnetic field of 0.2 T in a 100 nm wide barrier, given the strain pattern described in [173]. Since Δ_{SO} and Δ equal zero in graphene, these two parameters would have to be induced artificially in the barrier, a feat possible because bulk electrons are fully exposed on the graphene surface. Hexagonal Boron Nitride has an intrinsically broken inversion symmetry, and forms a generally higher quality electronic heterostructure with graphene as opposed to other substrates [65], manifested in reduced charge impurity, ultra-flatness, and high electron mobility. It also has a minuscule lattice mismatch with respect to graphene [146], which causes a moiré pattern, resulting in Hofstadter fractal spectrum [174, 175]. While the emerging superlattice potential was suggested to induce insulating puddles with opposing masses [147, 176], it was also argued that an average gap will be opened nevertheless [148]. As already mentioned in the previous chapter, a gap of about 30 meV in a graphene/hBN composite, consistent with inversion symmetry breaking was detected recently [66, 67]. The average gap appears because the area of the favored commensurate stacking expands by stretching of the graphene lattice, once the two layers are well aligned [67, 94, 149]. This strain can

[1] Note that the symmetry $\tau_B = +\tau, \phi \to \tau_B = -\tau, -\phi$ does not hold in general, due to the aforementioned interplay with the orbital magnetic moments, although it effectively appears so for the parameter window of interest.

also produce pseudmagnetic field patterns in graphene [177].

On the other hand, it was suggested that engineering SOC in graphene can be achieved by adatoms or substrates [95, 150–152]. This was indeed experimentally verified recently, where SOC as high as 17 meV was observed [98, 99]. Since SOC in Eq. (6.10) commutes with out-of-plane spin, increasing it will not affect scattering of this spin component. However, inversion symmetry breaking will cause new extrinsic spin relaxation mechanisms [140, 178]. The use of hBN as a substrate would prove beneficial here, since it was shown that the resulting heterostructure supports very long spin relaxation lengths [142]. Moreover, we argue that scattering processes could also be reasonably reduced by manipulating barrier length and/or strain patterns.

Chapter 7

Conclusion

In this thesis a range of graphene structures with varying geometries were studied. In particular, phenomena related to the manifestation of magnetism were analyzed, either due to the response to an external (pseudo)magnetic field, magnetic moments emerging from the e-e interaction or the band structure, or both. After laying out the basic theory in two introductory chapters, in Chapter 3 the electron and hole states in a monolayer graphene circular quantum dot were modeled using the Dirac-Weyl equation. Two distinct types of boundary conditions were employed, namely the infinite-mass and the zigzag boundary conditions. An energy gap was found only for the case of infinite-mass boundary condition, whereas the peculiar zero energy state, which is pseudo-spin polarized and localized close to the zigzag boundary, exists when the zigzag boundary condition is imposed. Increase of the magnetic field diminishes the influence of the edge on the electron confinement, and the states merge into Landau levels. The obtained spectra exhibit different symmetries between the electron and hole spectra, and also different intervalley symmetries. However, the variation of the angular current density with magnetic field is quite similar for the two adopted boundary conditions.

The states which collapse into $n = 0$ Landau level (for $B \to \infty$) are found to exhibit paramagnetic behavior due to the influence of the edge, and become pseudo-spin polarized when the magnetic field increases. Negative m states are found to exhibit both clockwise and counterclockwise currents when the magnetic field increases. Furthermore, the boundary conditions and the intervalley symmetry are found to influence the absorption spectra. Equal transition energies in the two valleys lead to the most intense absorption line for the adopted infinite mass boundary condition. On the other hand, different transition energies in the two

valleys lead to much smaller absorption oscillator strength if the zigzag boundary condition is used.

It is also found that many features of the more realistic tight-binding model of graphene quantum dots can be described by a simplified continuum approach to circular quantum dots. Namely, the energy states in the continuum and TB models converge to the Landau levels at high magnetic field in a similar way. However, due to their inevitable zigzag edges, circular graphene quantum dots cut out from a graphene lattice exhibit a dense quasi-zero energy band, formed by groups of states which exhibit self-similarity. This is a manifestation of the microscopic character of these dots, which cannot be properly described by any continuum-based model. Nevertheless, for circular dots based on mass confinement, the tight-binding results and the analytical infinite mass boundary condition results agree very well for low energies and large dot radius. Thus, another conclusion is extracted from this comparison: the infinite mass boundary condition for the Dirac-Weyl equation, frequently used to simulate electron states in graphene nanostructures, can describe only quantum dots created by mass-related confinement, whereas the dots cut out from a graphene layer obtained in recent experiments [179] have a much more complex spectrum which, at least in the absence of possible additional potential terms (due to e.g. edge reconstruction, magnetization, etc.), cannot be described by either infinite mass or zigzag boundary condition in the continuum model.

Subsequently, in Chapter 4 we predicted an antiferromagnetic phase in hexagonal graphene quantum rings with zigzag inner edge described by the mean-field Hubbard model. The distribution of magnetic moments was found to strongly depend on the type of the outer edge, and larger antiferromagnetic order was found in rings than in hexagonal dots. Peculiar hybridization between the states of adjacent sides of the inner ring edge is the reason behind the increase of magnetization of rings with respect to dots. Also, the staggered magnetization and the maximum magnetic moment are found to be strongly influenced by the size and the shape of the rings. For wide rings, the maximum magnetic moment is largest when both the inner and outer edges are zigzag. But, as a consequence of the hybridization between the states of the two edges, the maximum magnetic moment in a ring with armchair outer edge exceeds the one for the zigzag outer edge when the ring width decreases. The staggered magnetization in both the hexagonal dots and the rings with zigzag outer edge is found to decrease faster than in the rings with armchair outer edge when the number of the edge defects increases.

In Chapter 5, we addressed the orbital magnetic moments emerging from the band topology of insulating Dirac systems, as well as their manifestation on transport characteristics. In particular, we closely examined the moments coupled to the spin degree of freedom, arising due to strong spin-orbit coupling, and thus leading to the renormalization of the g-factor. Their duality with the valley-contrasting orbital moments found in honeycomb lattices with broken spatial symmetry was demonstrated, alongside with the duality of the Landau spectrum, particularly manifested in the behavior of the zeroth Landau level.

After establishing that magnetic properties couple with Δ_{SO} and the spin quantum number on the one hand, and Δ and the valley quantum number on the other hand in an analogous fashion, we explored the influence of the orbital magnetic moments on the transport properties. In particular, we focused on the transmission through a single 1D barrier made of artificially enhanced spin-orbit coupling in graphene. We have shown that certain Zeeman-like magneto-transport signatures are a clear manifestation of the induced moments. The conductance G through the device for the two spins start deviating from each other with increasing magnetic field. The effects of the moments on the fringe pattern of the transmission coefficients are most clearly observed in the energy dependence of the derivative of the conductance with respect to the electron energy dG/dE. This quantity reflects the increasing shifts in the interference maxima of opposite spins with increasing magnetic field; they are largest near the band edges, and they decrease for larger energies due to the decrease of the orbital magnetic moments themselves.

Because of the analogy between the mass and the SOC terms and the orbital moments they induce, the presented results are also valid for valley transmission through a barrier with only $\Delta \neq 0$. This, however, cannot be captured by numerical techniques such as the TB NEGF method, which is only able to account for the spin degree of freedom, and the associated orbital moments. Nevertheless, this behavior should be present in real devices, even in the absence of a clearly observable transport gap, since the Berry curvature hot spot can extend over a wide energy range.

In the end, in Chapter 6 we proposed a device which enables spatial separation of opposite spin-valley pairs. The proposed spin-valley filter consists of a strained barrier with artificially engineered electron mass and SOC. The pseudomagnetic field enforces opposite cyclotron trajectories for the two gapless spin-valleys. Nanoribbon geometry could provide the practical testing ground for this effect, with the barrier formed perpendicular to the ribbon. If $\Delta > \Delta_{SO}$, the device would be in the

topologically trivial phase, and the polarized current could in principle be detected by leads attached to the edges of the ribbon. On the other hand, if $\Delta_{SO} > \Delta$, edge states could become a nuisance. However the device could still operate in the domain of electron optics. In other words, the effect would be observable for a sufficiently collimated beam injected far from the edges. Collimation could also be achieved by means of a smooth Klein barrier in front of the studied device [180].

Appendix A

Bloch theorem and Peierls substitution

The Hamiltonian is given by

$$H = \frac{\mathbf{p}^2}{2m} + U(\mathbf{r}), \tag{A.1}$$

where $U(\mathbf{r}) = \sum_{\mathbf{R}} V_c(\mathbf{r} - \mathbf{R}_A) + V_c(\mathbf{r} - \mathbf{R}_B)$, is the potential landscape due to the honeycomb crystal lattice. The Bloch theorem asserts that the solution to the problem

$$H\Psi_{\mathbf{k}} = E(\mathbf{k})\,\Psi_{\mathbf{k}}, \tag{A.2}$$

is to be sought in the Bloch sum form

$$\Psi_{\mathbf{k}} = c_A \Psi_{\mathbf{k}A} + c_B \Psi_{\mathbf{k}B}. \tag{A.3}$$

where

$$\Psi_{\mathbf{k}\alpha} = \frac{1}{\sqrt{N}} \sum_{\mathbf{R}} e^{i\mathbf{k}\cdot\mathbf{R}} \phi(\mathbf{r} - \mathbf{R}_\alpha). \tag{A.4}$$

The corresponding eigenvalues $E(\mathbf{k})$, which form bands depending on the crystal momentum $\mathbf{k}$, are obtained by calculating the matrix elements $\langle \Psi_{\mathbf{k}\alpha} | H | \Psi_{\mathbf{k}} \rangle$. For instance, multiplying Eq. (A.2) with A component of the Bloch sum results in

$$\begin{aligned}\frac{c_A}{N}\sum_{\mathbf{R}\mathbf{R}'} e^{i\mathbf{k}(\mathbf{R}'-\mathbf{R})}\int d\mathbf{r}\phi^*\left(\mathbf{r}-\mathbf{R}_A\right)H\phi\left(\mathbf{r}-\mathbf{R}'_A\right)+\\ \frac{c_B}{N}\sum_{\mathbf{R}\mathbf{R}'} e^{i\mathbf{k}(\mathbf{R}'-\mathbf{R})}\int d\mathbf{r}\phi^*\left(\mathbf{r}-\mathbf{R}_A\right)H\phi\left(\mathbf{r}-\mathbf{R}'_B\right).\end{aligned} \tag{A.5}$$

Note that the matrix element depends only on the difference $\mathbf{R}'-\mathbf{R}$, which allows summation over the unit cells in the lattice, canceling the N factor in the denominator. In the light of the tight binding approximation, which refers to strong ties of a valence electron to its parent atom, one can neglect overlap of orbitals on neighboring atoms. Additionally, employing the two-center approximation, which disregards any matrix elements where orbitals and the potential are located on three different sites, allows further simplification. This means that the first part reduces to the on-site energy ϵ_A, without any phase factors. On the other hand, the second part collects phase factors corresponding to hopping from three nearest neighbor atoms of an atom A, multiplied by the hopping integral $-t = \int d\mathbf{r}\phi^*\left(\mathbf{r}-\mathbf{R}_A\right)V_c\left(\mathbf{r}-\mathbf{R}_A\right)\phi\left(\mathbf{r}-\mathbf{R}_B\right)$. Setting $\epsilon_\alpha = 0$ gives the kernel of the Hamiltonian in Eq. (1.13).

In the presence of the magnetic field the Hamiltonian changes to

$$H = \frac{\left(\mathbf{p}-q\mathbf{A}\right)^2}{2m}+U\left(\mathbf{r}\right), \tag{A.6}$$

where q is the charge of the particle. In the thesis the convention $q=-e$ for electrons is used (i.e. $e>0$). The additional term introduces complications, and the original Bloch sum becomes inadequate. As it turns out, simply adding a phase term

$$\Psi_{\mathbf{k}\alpha} = \frac{1}{\sqrt{N}}\sum_{\mathbf{R}} e^{i\left(\mathbf{k}\cdot\mathbf{R}+\frac{e}{\hbar}G_{\mathbf{R}}\right)}\phi\left(\mathbf{r}-\mathbf{R}_\alpha\right), \tag{A.7}$$

where

$$G_{\mathbf{R}} = \int_{\mathbf{R}}^{\mathbf{r}}\mathbf{A}\cdot d\mathbf{l}, \tag{A.8}$$

resolves the issue. The hopping matrix elements now read

$$
\begin{aligned}
H_{AB} =& \frac{1}{N}\sum_{\mathbf{R}\mathbf{R}'} e^{i\mathbf{k}(\mathbf{R}'-\mathbf{R})} \int d\mathbf{r} e^{-i\frac{q}{\hbar}G_{\mathbf{R}}} \phi^*\left(\mathbf{r}-\mathbf{R}_A\right) \left[\frac{\left(\mathbf{p}-q\mathbf{A}\right)^2}{2m} + U\left(\mathbf{r}\right)\right] e^{i\frac{q}{\hbar}G_{\mathbf{R}'}} \phi\left(\mathbf{r}-\mathbf{R}'_B\right) \\
=& \frac{1}{N}\sum_{\mathbf{R}\mathbf{R}'} e^{i\mathbf{k}(\mathbf{R}'-\mathbf{R})} e^{i\frac{q}{\hbar}\int_{\mathbf{R}'}^{\mathbf{R}} \mathbf{A}\cdot d\mathbf{l}} \\
& \times \int d\mathbf{r} e^{i\frac{q}{\hbar}\Phi(\mathbf{r})} \phi^*\left(\mathbf{r}-\mathbf{R}_A\right) \left[\frac{\left(\mathbf{p}-q\mathbf{A}+q\nabla G_{\mathbf{R}'}\right)^2}{2m} + U\left(\mathbf{r}\right)\right] \phi\left(\mathbf{r}-\mathbf{R}'_B\right) \\
=& \frac{1}{N}\sum_{\mathbf{R}\mathbf{R}'} e^{i\mathbf{k}(\mathbf{R}'-\mathbf{R})} e^{i\frac{q}{\hbar}\int_{\mathbf{R}'}^{\mathbf{R}} \mathbf{A}\cdot d\mathbf{l}} \int d\mathbf{r} \phi^*\left(\mathbf{r}-\mathbf{R}_A\right) \left[\frac{\mathbf{p}^2}{2m} + U\left(\mathbf{r}\right)\right] \phi\left(\mathbf{r}-\mathbf{R}'_B\right). \quad \text{(A.9)}
\end{aligned}
$$

The relation $\nabla G_{\mathbf{R}'} = \mathbf{A}$ holds for the tight binding condition and in the case when the magnetic field is invariant at the scale of the crystal lattice [181]. On the other hand, the flux $\Phi\left(\mathbf{r}\right) = \oint_{\mathbf{R}'\to\mathbf{r}\to\mathbf{R}} \mathbf{A}\cdot d\mathbf{l}$ is larger when the integrand $\mathbf{r}$ is further from the two vectors $\mathbf{R}$ and $\mathbf{R}'$, where the atomic orbitals are effectively zero, while the flux is vanishing where the hopping integral is nonzero. Having these two things in mind helps explain the transition from the second to the third line.

Now it becomes obvious that the matrix elements are the same as in the case without magnetic field, apart from the phase factor picked up, which is denoted the Peierls phase [182]. This is tremendously convenient, since then we get to use the same material parameters regardless of the magnetic field value, and the corresponding phase is computationally trivial to take into account. For electrons it amounts to replacing the hopping term t_{ij} with $t_{ij}e^{i\frac{e}{\hbar}\int_i^j \mathbf{A}\cdot d\mathbf{l}}$. Finally, let us note that a beautiful and elucidating explanation for this phase can be found in Feynman's Lectures (Vol. III, Chapter 21) [183].

Appendix B

Energy levels for low magnetic fields

We start from Eq. (7) for zero magnetic field which can be rewritten as,

$$D^{(0)}|\chi_{1i}^{(0)}\rangle = \lambda_i^{(0)}|\chi_{1i}^{(0)}\rangle, \tag{B.1}$$

where the operator $D^{(0)} = -[\frac{d^2}{d\rho^2} + \frac{1}{\rho}\frac{d}{d\rho} - \frac{m^2}{\rho^2}]$, $\lambda_i^{(0)} = (\varepsilon_{\pm 1,m,n}^{e,h,(0)})^2$ (with i being the eigenvalue index) and $|\chi_{1i}^0(\rho)\rangle$ is given by Eq. (3.9). For the case of non-zero magnetic field we have

$$(D^{(0)} + \beta D_1^{(1)} + \beta^2 D_2^{(1)})|\chi_{1i}^{(1)}\rangle = \lambda_i^{(1)}|\chi_{1i}^{(1)}\rangle, \tag{B.2}$$

where $D_1^{(1)} = 2(m+1)$ and $D_2^{(1)} = \rho^2$. We assume that $|\chi_{1i}^{(1)}\rangle = |\chi_{1i}^{(0)}\rangle$ for small magnetic fields. Multiplying $\langle\chi_{1i}^{(0)}|$ on both sides of the above equation we have,

$$\lambda_i^{(1)} = \lambda_i^{(0)} + 2\beta(m+1) + \beta^2 \frac{\langle\chi_{1i}^{(0)}|\rho^2|\chi_{1i}^{(0)}\rangle}{\langle\chi_{1i}^{(0)}|\chi_{1i}^{(0)}\rangle} \tag{B.3}$$

and finally we obtain,

$$\varepsilon_{\pm 1,m,n}^{e,h,(1)}(\beta) = \sqrt{(\varepsilon_{\pm 1,m,n}^{e,h,(0)})^2 + 2\beta(m+1) + \beta^2 A(m)}, \tag{B.4}$$

where

$$A(m) = \frac{\int_0^1 \rho^3 J_m^2(\varepsilon_{\pm 1,m,n}^{e,h,(0)}\rho)d\rho}{\int_0^1 \rho J_m^2(\varepsilon_{\pm 1,m,n}^{e,h,(0)}\rho)d\rho} = \frac{m+1}{m+2}\frac{{}_2\widetilde{F}_3(m+\frac{1}{2}, m+2; m+1, m+3, 2m+1; -\varepsilon_{n,m}^{2(0)})}{{}_2\widetilde{F}_3(m+\frac{1}{2}, m+1; m+1, m+2, 2m+1; -\varepsilon_{n,m}^{2(0)})} \tag{B.5}$$

Appendix C

Transmission through a barrier in bulk graphene

The studied structure and the chosen gauge for the vector potential [Eqs. (5.18) and (6.11)] ensure translational invariance along the y direction, so k_y is a good quantum number and the solutions have the form $\Psi(x,y) = \exp(ik_y y)\,(\psi_A(x), \psi_B(x))^T$. The following coupled system of differential equations, for the amplitudes on the two sublattices can then be obtained:

$$\left(\tau k_x \mp i k_y \mp i\frac{e}{\hbar}A_y\right)\psi_{B/A} \pm \delta\psi_{A/B} = \epsilon\psi_{A/B}. \tag{C.1}$$

Reducing the coupled system to a set of two independent second order differential equations leads to

$$\left[\partial_x^2 \mp \tau\frac{e}{\hbar}(\partial_x A_y) - \left(k_y + \frac{e}{\hbar}A_y\right)^2 + \epsilon^2 - \delta^2\right]\psi_{A/B} = 0. \tag{C.2}$$

Bearing in mind the form of the vector potential of the pseudomagnetic field [Eq. (6.11)], the differential equation in the barrier becomes

$$\left[\partial_x^2 \mp \frac{\tau\tau_B}{l_B^2} - \left(k_y + \tau_B\frac{x}{l_B^2}\right)^2 + \epsilon^2 - \delta^2\right]\psi_{A/B} = 0. \tag{C.3}$$

The solutions for real magnetic field can be restored in the limit $\tau_B = 1$. By using the transformation $z = \sqrt{2}\,(k_y l_B + \tau_B x/l_B)$ the following equation is obtained

$$\left[\partial_z^2 + 1/2 - 1/2 \mp \tau\tau_B\frac{1}{2} + \left(\epsilon^2 - \delta^2\right)\frac{l_B^2}{2} - \frac{z^2}{4}\right]\psi_{A/B} = 0, \tag{C.4}$$

which is of the form of the parabolic cylinder (Webers) differential equation

$$y'' + \left(\nu + \frac{1}{2} - \frac{z^2}{4}\right) y = 0, \tag{C.5}$$

whose solutions are given in terms of parabolic cylinder functions

$$y = C_1 D_\nu(z) + C_2 D_\nu(-z). \tag{C.6}$$

Finally the solution for the first sublattice is given by

$$\begin{aligned} \psi_A =& C_1 D_{\nu_A}\left[\sqrt{2}\left(k_y l_B + \tau_B x/l_B\right)\right] \\ &+ C_2 D_{\nu_A}\left[-\sqrt{2}\left(k_y l_B + \tau_B x/l_B\right)\right], \end{aligned} \tag{C.7}$$

where $\nu_A = \left(\epsilon^2 - \delta^2\right) l_B^2/2 - \tau\tau_B/2 - 1/2$. For the other sublattice after employing the recurrence relations

$$\frac{\partial D_\nu(z)}{\partial_z} = \frac{1}{2} z D_\nu(z) - D_{\nu+1}(z), \tag{C.8}$$

$$\frac{\partial D_\nu(z)}{\partial_z} = \nu D_{\nu-1}(z) - \frac{1}{2} z D_\nu(z), \tag{C.9}$$

for $\tau\tau_B = +1$ and $\tau\tau_B = -1$ respectively, and the relationship (C.1), one obtains the following expression

$$\begin{aligned} \psi_B =& C_1 g D_{\nu_B}\left[\sqrt{2}\left(k_y l_B + \tau_B x/l_B\right)\right] \\ &- C_2 g D_{\nu_B}\left[-\sqrt{2}\left(k_y l_B + \tau_B x/l_B\right)\right], \end{aligned} \tag{C.10}$$

where $\nu_B = \left(\epsilon^2 - \delta^2\right) l_B^2/2 + \tau\tau_B/2 - 1/2$, and

$$g = i\left[\frac{\sqrt{2}}{\left(\epsilon + \tau\tau_B\delta\right) l_B}\right]^\tau. \tag{C.11}$$

If the relation

$$D_\nu\left(z\right) = 2^{-\nu/2} e^{-z^2/4} H_\nu\left(\frac{z}{\sqrt{2}}\right) \tag{C.12}$$

is employed, the spinor multiplied by C_1 in Eqs. (C.7) and (C.10) reduces to the solution (5.12), once the incident energy is equal to a particular Landau level, as could be expected.

The incident wave function is given by

$$\psi_I = e^{ik_x x} \begin{pmatrix} 1 \\ \tau e^{i\tau\phi} \end{pmatrix} + r e^{-ik_x x} \begin{pmatrix} 1 \\ \tau e^{i\tau(\pi-\phi)} \end{pmatrix}, \tag{C.13}$$

where $\phi = \arctan k_y/k_x$.

Finally, in the third region the vector potential is a non-zero constant, and employing the standard plane wave ansatz, the solution is given by

$$\psi_{III} = t\sqrt{\frac{k_x}{k'_x}} e^{ik'_x x} \begin{pmatrix} 1 \\ \tau e^{i\tau\theta} \end{pmatrix}, \tag{C.14}$$

with the energy of the plane wave given by $\epsilon = \alpha\sqrt{k_x'^2 + k_y'^2}$, $k'_x = \epsilon\cos\theta$, the effective transverse momentum after the barrier $k'_y = \epsilon\sin\theta = k_y + \tau_B W/l_B^2$ and θ being the angle of energy propagation, with respect to the direction transverse to the barrier. The additional factor under the square root follows from current conservation [23]. Again by replacing the expression for the momenta before and after the barrier, one obtains the effective law of refraction for a barrier of thickness W with nonzero Δ, Δ_{SO} and B as

$$\epsilon\sin\theta = \epsilon\sin\phi + \tau_B W/l_B^2. \tag{C.15}$$

The expressions for the wave functions in different regions, (C.13), (C.7), (C.10), and (C.14) are then matched at the interfaces $x = 0$ and $x = W$, which gives a system of equations, whose solution yields the transmission amplitude t

$$t = \frac{2g\tau\cos(\tau\phi)\left(G_A^+ G_B^- + G_A^- G_B^+\right)}{e^{ik'_x W} f}\sqrt{\frac{k'_x}{k_x}}, \tag{C.16}$$

where

$$\begin{aligned} f = g^2\left(F_B^+ G_B^- - F_B^- G_B^+\right) + e^{i\tau(\theta-\phi)}\left(F_A^+ G_A^- - F_A^- G_A^+\right) \\ + g\tau e^{i\tau\theta}\left(F_B^- G_A^+ + F_B^+ G_A^-\right) + g\tau e^{-i\tau\phi}\left(F_A^+ G_B^- + F_A^- G_B^+\right). \end{aligned} \tag{C.17}$$

Here the coefficients $F^\pm$ and $G^\pm$ are given by

$$F^\pm_{A/B} = D_{\nu_{A/B}}\left[\pm\sqrt{2}k_y l_B\right], \tag{C.18}$$

$$G^\pm_{A/B} = D_{\nu_{A/B}}\left[\pm\sqrt{2}(k_y l_B + \tau_B\frac{W}{l_B})\right]. \tag{C.19}$$

Bibliography

[1] R. Saito, G. Dresselhaus, and M. S. Dresselhaus, *Physical Properties of Carbon Nanotubes*, Vol. 4 (World Scientific, 1998) (cit. on p. 1).

[2] M. O. Goerbig, "Electronic properties of graphene in a strong magnetic field", Rev. Mod. Phys. **83**, 1193–1243 (2011) (cit. on pp. 1, 7, 9, 81).

[3] S. Park, D. Srivastava, and K. Cho, "Generalized Chemical Reactivity of Curved Surfaces: Carbon Nanotubes", Nano Lett. **3**, 1273–1277 (2003) (cit. on p. 2).

[4] S Niyogi, M. Hamon, H Hu, B Zhao, P Bhowmik, R Sen, M. Itkis, and R. Haddon, "Chemistry of Single-Walled Carbon Nanotubes", Accounts Chem. Res. **35**, 1105–1113 (2002) (cit. on p. 2).

[5] N. D. Mermin, "Crystalline Order in Two Dimensions", Phys. Rev. **176**, 250–254 (1968) (cit. on p. 2).

[6] R. E. Peierls, "Quelques proprietes typiques des corps solides", Ann. Inst. H. Poincare **5**, 177–222 (1935) (cit. on p. 2).

[7] L. D. Landau, "Theory of phase transformations. I", Phys. Z. Sowjetunion **11**, 26–35 (1937) (cit. on p. 2).

[8] K. S. Novoselov, A. K. Geim, S. V. Morozov, D. Jiang, Y. Zhang, S. V. Dubonos, I. V. Grigorieva, and A. Firsov, "Electric Field Effect in Atomcially Thin Carbon Films", Science **306**, 666–669 (2004) (cit. on pp. 2, 61).

[9] C. L. Kane and E. J. Mele, "Quantum Spin Hall Effect in Graphene", Phys. Rev. Lett. **95**, 226801 (4 p.) (2005) (cit. on pp. 3, 13, 15, 94).

[10] C. L. Kane and E. J. Mele, "Z_2 Topological Order and the Quantum Spin Hall Effect", Phys. Rev. Lett. **95**, 146802 (4 p.) (2005) (cit. on pp. 3, 74–76).

[11] C. Lee, X. Wei, J. W. Kysar, and J. Hone, "Measurement of Elastic Properties and Intrinsic Strength of Monolayer Graphene", Science **321**, 385–388 (2008) (cit. on p. 3).

[12] A. A. Balandin, S. Ghosh, W. Bao, I. Calizo, D. Teweldebrhan, F. Miao, and N. Lau, Chun, "Superior Thermal Conducitivty of Single-Layer Graphene", Nano. Lett. **8**, 902–907 (2008) (cit. on p. 3).

[13] J.-H. Chen, C. Jang, S. Xiao, M. Ishigami, and M. S. Fuhrer, "Intrinsic and extrinsic performance limits of graphene devices on SiO_2", Nature Nanotech. **3**, 206–209 (2008) (cit. on p. 3).

[14] S. V. Morozov, K. S. Novoselov, M. I. Katsnelson, F. Schedin, D. C. Elias, J. A. Jaszczak, and A. K. Geim, "Giant Intrinsic Carrier Mobilities in Graphene and Its Bilayer", Phys. Rev. Lett. **100**, 016602 (4 p.) (2008) (cit. on p. 3).

[15] K. I. Bolotin, K. J. Sikes, Z. Jiang, M. Klima, G. Fudenberg, J. Hone, P. Kim, and H. L. Stormer, "Ultrahigh electron mobility in suspended graphene", Solid State Commun. **146**, 351–355 (2008) (cit. on p. 3).

[16] K. S. Novoselov, A. K. Geim, S. V. Morozov, D. Jiang, M. I. Katsnelson, I. V. Grigorieva, S. V. Dubonos, and A. A. Firsov, "Two-dimensional gas of massless Dirac fermions in graphene", Nature (London) **438**, 197–200 (2005) (cit. on pp. 3, 21).

[17] Y. Zhang, Y.-W. Tan, H. L. Stormer, and P. Kim, "Experimental observation of the quantum Hall effect and Berry's phase in graphene", Nature (London) **438**, 201–204 (2005) (cit. on pp. 3, 21).

[18] A. H. Castro Neto, F. Guinea, N. M. R. Peres, K. S. Novoselov, and A. K. Geim, "The electronic properties of graphene", Rev. Mod. Phys. **81**, 109–162 (2009) (cit. on pp. 5, 10, 53, 91).

[19] C. Bena and G. Montambaux, "Remarks on the tight-binding model of graphene", New. J. Phys. **11**, 095003 (15 p.) (2009) (cit. on p. 7).

[20] C. W. J. Beenakker, "Colloquium: Andreev reflection and Klein tunneling in graphene", Rev. Mod. Phys. **80**, 1337–1354 (2008) (cit. on pp. 9, 11).

[21] V. P. Gusynin, S. G. Sharapov, and J. P. Carbotte, "AC conductivity of graphene: From tight-binding model to $2 + 1$-dimensional quantum electrodynamics", Int. J. Mod. Phys. B **21**, 4611–4658 (2007) (cit. on p. 10).

[22] M. I. Katsnelson, K. S. Novoselov, and A. K. Geim, "Chiral tunnelling and the Klein paradox in graphene", Nat. Phys. **2**, 620–625 (2006) (cit. on pp. 11, 36).

[23] P. E. Allain and J. N. Fuchs, "Klein tunneling in graphene: optics with massless elctrons", Eur. Phys. J. B **83**, 301–317 (2011) (cit. on pp. 11, 113).

[24] A. Bostwick, T. Ohta, T. Seyller, K. Horn, and E. Rotenberg, "Quasiparticle dynamics in graphene", Nat. Phys. **3**, 36–40 (2007) (cit. on p. 12).

[25] D. Huertas-Hernando, F. Guinea, and A. Brataas, "Spin-orbit soupling in curved graphene, fullerene, nanotubes, and nanotube caps", Phys. Rev. B **74**, 155426 (15 p.) (2006) (cit. on p. 14).

[26] S. Konschuh, M. Gmitra, and J. Fabian, "Tight-bidning theory of spin-orbit coupling in graphene", Phys. Rev. B **82**, 245412 (11 p.) (2010) (cit. on pp. 14, 15).

[27] M. Gmitra, S. Konschuh, C. Ertler, C. Ambrosch-Drax, and J. Fabian, "Band-structure topologies of graphene: Spin-orbit coupling effects from first principles", Phys. Rev. B **80**, 235431 (5 p.) (2009) (cit. on p. 14).

[28] K. Watanabe, T. Taniguchi, and H. Kanda, "Direct-bandgap properties and evidence for ultraviolet lasing of hexagonal-boron nitride single crystal", Nat. Mater. **3**, 404–409 (2004) (cit. on p. 16).

[29] F. D. M. Haldane, "Model for a Quantum Hall Effect without Landau Levels: Condensed-Matter Realization of the "Parity Anomaly"", Phys. Rev. Lett. **61**, 2015–2018 (1988) (cit. on pp. 17, 76).

[30] K. S. Novoselov, Z. Jiang, Y. Zhang, S. V. Morozov, H. L. Stormer, U. Zeitler, J. C. Maan, G. S. Boebinger, P. Kim, and A. K. Geim, "Room Temperature Quantum Hall Effect in Graphene", Science **315**, 1379 (2007) (cit. on p. 21).

[31] L. P. Kadanoff and G. Baym, *Quantum Statistical Mechanics* (Benjamin, New York, Les Ulis Cedex, 1962) (cit. on p. 22).

[32] L. V. Keldysh, "Diagram Technique for Nonequilibrium Processes", Sov. Phys. JETP **20**, 1018–1026 (1965) (cit. on p. 22).

[33] S. Datta, *Electronic Transport in Mesoscopic Systems* (Cambridge University Press, Cambridge, Les Ulis Cedex, 1995) (cit. on pp. 22, 23).

[34] T. Li and S.-P. Lu, "Quantum conductance of graphene nanoribbons with edge defects", Phys. Rev. B **77**, 085408 (8 p.) (2008) (cit. on p. 24).

[35] M. Wimmer, "Quantum transport in nanostructures: From computational concepts to spintronics in graphene and magnetic tunnel junctions", PhD thesis (Universität Regensburg, Physics Department, 2008) (cit. on p. 24).

[36] D. S. Fisher and P. A. Lee, "Relation between conductivity and transmition matrix", Phys. Rev. B **23**, 6851–6854 (1981) (cit. on p. 24).

[37] C. H. Lewenkopf and E. R. Mucciolo, "The recursive Green's function method for graphene", J. Computat. Electron. **12**, 203–231 (2013) (cit. on p. 25).

[38] F. Miao, S. Wijeratne, Y. Zhang, U. C. Coskun, W. Bao, and C. N. Lau, "Phase-Coherent Transport in Graphene Quantum Billiards", Science **317**, 1530–1533 (2007) (cit. on p. 25).

[39] K. Wakabayashi, K.-i. Sasaki, T. Nakanishi, and T. Enoki, "Electronic states of graphene nanoribbons and analytical solutions", Sci. Technol. Adv. Matter. **11**, 054504 (18 p.) (2010) (cit. on pp. 27, 29, 34).

[40] M. Wimmer, A. R. Akhmerov, and F. Guinea, "Robustness of edge states in graphene quantum dots", Phys. Rev. B **82**, 045409 (9 p.) (2010) (cit. on pp. 29, 37).

[41] M. Ezawa and N. Nagaosa, "Interference of topologically protected edge states in silicene nanoribbons", Phys. Rev. B **88**, 121401 (5 p.) (2013) (cit. on p. 30).

[42] W. Yao, S. A. Yang, and Q. Niu, "Edge States in Graphene: From Gapped Flat-Band to Gapless Chiral Modes", Phys. Rev. Lett. **102**, 096801 (4 p.) (2009) (cit. on p. 32).

[43] G. Z. Magda, X. Jin, I. Hagymási, P. Vancsó, Z. Osváth, P. Nemes-Incze, C. Hwang, L. P. Biró, and L. Tapasztó, "Room-temperature magnetic order on zigzag edges of narrow graphene nanoribbons", Nature (London) **514**, 608–611 (2014) (cit. on pp. 35, 62).

[44] M. I. Katsnelson and K. S. Novoselov, "Graphene: New bridge between condensed matter physics and quantum electrodynamics", Solid State Commun. **143**, 3–13 (2007) (cit. on pp. 36, 45).

[45] L. A. Ponomarenko, F. Schedin, M. I. Katsnelson, R. Yang, E. W. Hill, K. S. Novoselov, and A. K. Geim, "Chaotic Dirac Billiard in Graphene Quantum Dots", Science **320**, 356–358 (2008) (cit. on p. 36).

[46] S. Schnez, K. Ensslin, M. Sigrist, and T. Ihn, "Analytic model of the energy spectrum of a graphene quantum dot in a perpendicular magnetic field", Phys. Rev. B **78**, 195427 (4 p.) (2008) (cit. on pp. 36, 37, 44).

[47] K. Nakada, M. Fujita, G. Dresselhaus, and M. S. Dresselhaus, "Edge state in graphene ribbons: Nanometer size effect and edge shape dependence", Phys. Rev. B **54**, 17954–17961 (1996) (cit. on pp. 36, 66).

[48] H. P. Heiskanen, M. Manninen, and J. Akola, "Electronic structure of triangular, hexagonal and round graphene flakes near the Fermi level", New J. Phys. **10**, 103015 (14 p.) (2008) (cit. on p. 36).

[49] H. Lee, Y. W. Son, N. Park, S. Han, and J. Yu, "Magnetic ordering at the edges of graphitic fragments: Magnetic tail interactions between the edge-localized states", Phys. Rev. B **72**, 174431 (8 p.) (2005) (cit. on p. 37).

[50] J. Fernádez-Rossier and J. J. Palacios, "Magnetism in Graphene Nanoislands", Phys. Rev. Lett. **99**, 177204 (4 p.) (2007) (cit. on pp. 37, 61, 66).

[51] X. Yan, X. Cui, B. Li, and L. Li, "Large, Solution-Processable Graphene Quantum Dots as Light Absorbers for Photovoltaics", Nano Lett. **10**, 1869–1873 (2010) (cit. on p. 37).

[52] Z. Z. Zhang, K. Chang, and F. M. Peeters, "Tuning of energy levels and optical properties of graphene quantum dots", Phys. Rev. B **77**, 235411 (5 p.) (2008) (cit. on p. 37).

[53] M. V. Berry and R. J. Mondragon, "Neutrino Billiards: Time-Reversal Symmetry-Breaking Without Magnetic Fields", Proc. R. Soc. Lond. A **412**, 53–74 (1987) (cit. on p. 39).

[54] D. P. DiVincenzo and E. J. Mele, "Self-consistent effective-mass theory for intralayer screening in graphite intercalation compounds", Phys. Rev. B **29**, 1685–1694 (1984) (cit. on p. 39).

[55] A. R. Akhmerov and C. W. J. Beenakker, "Boundary conditions for Dirac fermions on a terminated honeycomb lattice", Phys. Rev. B **77**, 085423 (10 p.) (2008) (cit. on pp. 39, 41).

[56] M Grujić, M Zarenia, A Chaves, M Tadić, G. Farias, and F. Peeters, "Electronic and optical properties of a circular graphene quantum dot in a magnetic field: Influence of the boundary conditions", Phys. Rev. B **84**, 205441 (12 p.) (2011) (cit. on pp. 44, 54, 81, 91).

[57] J. Palacios, J. J. Fernández-Rossier and L. Brey, "Vacancy-induced magnetism in graphene and graphene ribbons", Phys. Rev. B **77**, 195428 (14 p.) (2008) (cit. on pp. 44, 61, 69, 70).

[58] S. C. Kim, P. S. Park, and S. R. Eric Yang, "States near Dirac points of a rectangular graphene dot in a magnetic field", Phys. Rev. B **81**, 085432 (6 p.) (2010) (cit. on p. 44).

[59] C. S. Lent, "Edge states in a circular quantum dot", Phys. Rev. B **43**, 4179–4186 (1991) (cit. on p. 44).

[60] T. M. Rusin and W. Zawadzki, "Zitterbewegung of electrons in graphene in a magnetic field", Phys. Rev. B **78**, 125419 (9 p.) (2008) (cit. on p. 50).

[61] V. P. Gusynin and S. G. Sharapov, "Transport of Dirac quasiparticles in graphene: Hall and optical conductivities", Phys. Rev. B **73**, 245411 (18 p.) (2006) (cit. on p. 51).

[62] M Grujić, M Zarenia, M Tadić, and F. Peeters, "Interband optical absorption in a circular graphene quantum dot", Phys. Scripta **2012**, 014056 (4 p.) (2012) (cit. on p. 52).

[63] M. Grujić and M. Tadić, "Electronic states and optical transitions in a graphene quantum dot in a normal magnetic field", Serb. J. Electr. Eng. **8**, 53–62 (2011) (cit. on p. 53).

[64] S. Y. Zhou, G.-H. Gweon, A. V. Fedorov, P. N. First, W. A. de Heer, D.-H. Lee, F. Guinea, A. H. Castro Neto, and A. Lanzara, "Substrate-induced bandgap opening in epitaxial graphene", Nat. Mater. **6**, 770–775 (2007) (cit. on p. 57).

[65] C. R. Dean, A. F. Young, I. Meric, C. Lee, L. Wang, S. Sorgenfrei, K. Watanabe, T. Taniguchi, P. Kim, K. L. Shepard, and J. Hone, "Boron nitride substrates for high-quality graphene electronics", Nature Nanotech. **5**, 722–726 (2010) (cit. on pp. 57, 100).

[66] B Hunt, J. Sanchez-Yamagishi, A. Young, M Yankowitz, B. J. LeRoy, K Watanabe, T Taniguchi, P Moon, M Koshino, P Jarillo-Herrero, and R. Ashoori, "Massive Dirac Fermions and Hofstadter Butterfly in a van der Waals Heterostructure", Science **340**, 1427–1430 (2013) (cit. on pp. 57, 73, 92, 100).

[67] C. Woods, L Britnell, A Eckmann, R. Ma, J. Lu, H. Guo, X Lin, G. Yu, Y Cao, R. Gorbachev, A. V. Kretinin, J. Park, L. A. Ponomarenko, M. I. Katsnelson, Y. N. Gornostyrev, K. Watanabe, T. Taniguchi, C. Casiraghi, H.-J. Gao, A. K. Geim, and K. S. Novoselov, "Commensurate-incommensurate transition in graphene on hexagonal boron nitride", Nature Phys. **10**, 451–456 (2014) (cit. on pp. 57, 73, 100).

[68] M. T. Ong and E. J. Reed, "Engineered Piezoelectricity in Graphene", ACS Nano **6**, 1387–1394 (2012) (cit. on p. 61).

[69] M. F. El-Kady, V. Strong, S. Dubin, and R. B. Kaner, "Laser Scribing of High-Performance and Flexible Graphene-Based Electrochemical Capacitors", Science **335**, 1326–1330 (2012) (cit. on p. 61).

[70] T. Echtermeyer, L Britnell, P. Jasnos, A Lombardo, R. Gorbachev, A. Grigorenko, A. Geim, A. Ferrari, and K. Novoselov, "Strong plasmonic enhancement of photovoltage in graphene", Nat. Commun. **2**, 458 (5 p.) (2011) (cit. on p. 61).

[71] Y.-M. Lin, C. Dimitrakopoulos, K. A. Jenkins, D. B. Farmer, H.-Y. Chiu, A. Grill, and P. Avouris, "100-GHz Transistors from Wafer-Scale Epitaxial Graphene", Science **327**, 662 (1 p.) (2010) (cit. on p. 61).

[72] L Britnell, R. Gorbachev, R Jalil, B. Belle, F Schedin, A Mishchenko, T Georgiou, M. Katsnelson, L Eaves, S. Morozov, N. M. R. Peres, J. Leist, A. K. Geim, K. S. Novoselov, and L. A. Ponomarenko, "Field-Effect Tunneling Transistor Based on Vertical Graphene Heterostructures", Science **335**, 947–950 (2012) (cit. on p. 61).

[73] O. V. Yazyev, "Emergence of magnetism in graphene materials and nanostructures", Rep. Prog. Phys. **73**, 056501 (16 p.) (2010) (cit. on pp. 61, 63, 64).

[74] Y.-W. Son, M. L. Cohen, and S. G. Louie, "Half-metallic graphene nanoribbons", Nature (London) **444**, 347–349 (2006) (cit. on pp. 61, 62).

[75] J Fernández-Rossier, "Prediction of hidden multiferroic order in graphene zigzag ribbons", Phys. Rev. B **77**, 075430 (5 p.) (2008) (cit. on pp. 61, 66).

[76] H. R. Matte, K. Subrahmanyam, and C. Rao, "Novel Magnetic Properties of Graphene: Presence of Both Ferromagnetic and Antiferromagnetic Features and Other Aspects", J. Phys. Chem. C **113**, 9982–9985 (2009) (cit. on p. 61).

[77] T. Enoki and K. Takai, "The edge state of nanographene and the magnetism of the edge-state spins", Solid State Commun. **149**, 1144–1150 (2009) (cit. on p. 61).

[78] V. J. Joly, M. Kiguchi, S.-J. Hao, K. Takai, T. Enoki, R. Sumii, K. Amemiya, H. Muramatsu, T. Hayashi, Y. A. Kim, M. Endo, J. Campos-Delgado, F. López-Urías, A. Botello-Méndez, H. Terrones, M. Terrones, and M. S. Dresselhaus, "Observation of magnetic edge state in graphene nanoribbons", Phys. Rev. B **81**, 245428 (6 p.) (2010) (cit. on p. 61).

[79] A. Ney, P. Papakonstantinou, A. Kumar, N.-G. Shang, and N. Peng, "Irradiation enhanced paramagnetism on graphene nanoflakes", Appl. Phys. Lett. **99**, 102504 (3 p.) (2011) (cit. on p. 61).

[80] R. Nair, M Sepioni, I.-L. Tsai, O Lehtinen, J Keinonen, A. Krasheninnikov, T Thomson, A. Geim, and I. Grigorieva, "Spin-half paramagnetism in graphene induced by point defects", Nature Phys. **8**, 199–202 (2012) (cit. on p. 61).

[81] Y. Wang, Y. Huang, Y. Song, X. Zhang, Y. Ma, J. Liang, and Y. Chen, "Room-Temperature Ferromagnetism of Graphene", Nano Lett. **9**, 220–224 (2009) (cit. on p. 61).

[82] J. Hong, E. Bekyarova, P. Liang, W. A. de Heer, R. C. Haddon, and S. Khizroev, "Room-temperature Magnetic Ordering in Functionalized Graphene", Sci. Rep. **2**, 624 (6 p.) (2012) (cit. on p. 61).

[83] J. Kunstmann, C. Özdoğan, A. Quandt, and H. Fehske, "Stability of edge states and edge magnetism in graphene nanoribbons", Phys. Rev. B **83**, 045414 (8 p.) (2011) (cit. on p. 62).

[84] O. V. Yazyev and M. Katsnelson, "Magnetic Correlations at Graphene Edges: Basis for Novel Spintronics Devices", Phys. Rev. Lett. **100**, 047209 (4 p.) (2008) (cit. on p. 62).

[85] M. Wimmer, I. Adagideli, S. Berber, D. Tománek, and K. Richter, "Spin Currents in Rough Graphene Nanoribbons: Universal Fluctuations and Spin Injection", Phys. Rev. Lett. **100**, 177207 (4 p.) (2008) (cit. on p. 62).

[86] W. L. Wang, O. V. Yazyev, S. Meng, and E. Kaxiras, "Topological Frustration in Graphene Nanoflakes: Magnetic Order and Spin Logic Devices", Phys. Rev. Lett. **102**, 157201 (4 p.) (2009) (cit. on p. 62).

[87] M. Ezawa, "Generation and manipulation of spin current in graphene nanodisks: Robustness against randomness and lattice defects", Phys. E **42**, 703–706 (2010) (cit. on p. 62).

[88] X. Wei, M.-S. Wang, Y. Bando, and D. Golberg, "Electron-Beam-Induced Substitutional Carbon Doping of Boron Nitride Nanosheets, Nanoribbons, and Nanotubes", ACS Nano **5**, 2916–2922 (2011) (cit. on p. 62).

[89] E. Lieb, "Two theorems on the Hubbard model", Phys. Rev. Lett. **62**, 1201–1204 (1989) (cit. on p. 63).

[90] P Potasz, A. Güçlü, O Voznyy, J. Folk, and P Hawrylak, "Electronic and magnetic properties of triangular graphene quantum rings", Phys. Rev. B **83**, 174441 (6 p.) (2011) (cit. on p. 63).

[91] T. Wehling, E Şaşıoğlu, C Friedrich, A. Lichtenstein, M. Katsnelson, and S Blügel, "Strength of Effective Coulomb Interactions in Graphene and Graphite", Phys. Rev. Lett. **106**, 236805 (4 p.) (2011) (cit. on p. 64).

[92] H. Feldner, Z. Y. Meng, A. Honecker, D. Cabra, S. Wessel, and F. F. Assaad, "Magnetism of finite graphene samples: Mean-field theory compared with exact diagonalization and quantum Monte Carlo simulations", Phys. Rev. B **81**, 115416 (5 p.) (2010) (cit. on p. 64).

[93] M Grujić, M Tadić, and F. Peeters, "Antiferromagnetism in hexagonal graphene structures: Rings versus dots", Phys. Rev. B **87**, 085434 (6 p.) (2013) (cit. on p. 72).

[94] J. Jung, A. DaSilva, S. Adam, and A. H. MacDonald, "Origin of band gaps in graphene on hexagonal boron nitride", arXiv preprint arXiv:1403.0496 (2014) (cit. on pp. 73, 100).

[95] A. C. Neto and F. Guinea, "Impurity-Induced Spin-Orbit Coupling in Graphene", Phys. Rev. Lett. **103**, 026804 (4 p.) (2009) (cit. on pp. 73, 92, 101).

[96] O. Shevtsov, P. Carmier, C. Groth, X. Waintal, and D. Carpentier, "Tunable thermopower in a graphene-based topological insulator", Phys. Rev. B **85**, 245441 (6 p.) (2012) (cit. on pp. 73, 75).

[97] H. Jiang, Z. Qiao, H. Liu, J. Shi, and Q. Niu, "Stabilizing Topological Phases in Graphene via Random Adsorption", Phys. Rev. Lett. **109**, 116803 (5 p.) (2012) (cit. on pp. 73, 75).

[98] J. Balakrishnan, G. K. W. Koon, M. Jaiswal, A. C. Neto, and B. Özyilmaz, "Colossal enhancement of spin-orbit coupling in weakly hydrogenated graphene", Nature Phys. **9**, 284–287 (2013) (cit. on pp. 73, 75, 92, 101).

[99] A Avsar, J. Tan, T Taychatanapat, J Balakrishnan, G. Koon, Y Yeo, J Lahiri, A Carvalho, A. Rodin, E. OFarrell, G. Eda, A. H. Castro Neto, and B. Ozyilmaz, "Spin–orbit proximity effect in graphene", Nat. Commun. **5**, 4875 (6 p.) (2014) (cit. on pp. 73, 75, 92, 101).

[100] S. Cahangirov, M. Topsakal, E. Aktürk, H Şahin, and S. Ciraci, "Two-and One-Dimensional Honeycomb Structures of Silicon and Germanium", Phys. Rev. Lett. **102**, 236804 (4 p.) (2009) (cit. on p. 74).

[101] C.-C. Liu, W. Feng, and Y. Yao, "Quantum Spin Hall Effect in Silicene and Two-Dimensional Germanium", Phys. Rev. Lett. **107**, 076802 (4 p.) (2011) (cit. on p. 74).

[102] Y. Xu, B. Yan, H.-J. Zhang, J. Wang, G. Xu, P. Tang, W. Duan, and S.-C. Zhang, "Large-Gap Quantum Spin Hall Insulators in Tin Films", Phys. Rev. Lett. **111**, 136804 (5 p.) (2013) (cit. on p. 74).

[103] P. Vogt, P. De Padova, C. Quaresima, J. Avila, E. Frantzeskakis, M. C. Asensio, A. Resta, B. Ealet, and G. Le Lay, "Silicene: Compelling Experimental Evidence for Graphenelike Two-Dimensional Silicon", Phys. Rev. Lett. **108**, 155501 (5 p.) (2012) (cit. on p. 74).

[104] C.-L. Lin, R. Arafune, K. Kawahara, N. Tsukahara, E. Minamitani, Y. Kim, N. Takagi, and M. Kawai, "Structure of Silicene Grown on Ag (111)", Appl. Phys. Express **5**, 045802 (3 p.) (2012) (cit. on p. 74).

[105] A. Fleurence, R. Friedlein, T. Ozaki, H. Kawai, Y. Wang, and Y. Yamada-Takamura, "Experimental Evidence for Epitaxial Silicene on Diboride Thin Films", Phys. Rev. Lett. **108**, 245501 (5 p.) (2012) (cit. on p. 74).

[106] M. Dávila, L Xian, S Cahangirov, A Rubio, and G Le Lay, "Germanene: a novel two-dimensional germanium allotrope akin to graphene and silicene", New. J. Phys. **16**, 095002 (10 p.) (2014) (cit. on p. 74).

[107] L. Li, S.-z. Lu, J. Pan, Z. Qin, Y.-q. Wang, Y. Wang, G.-y. Cao, S. Du, and H.-J. Gao, "Buckled Germanene Formation on Pt (111)", Adv. Mater. **26**, 4820–4824 (2014) (cit. on p. 74).

[108] M.-C. Chang and Q. Niu, "Berry phase, hyperorbits, and the Hofstadter spectrum: Semiclassical dynamics in magnetic Bloch bands", Phys. Rev. B **53**, 7010–7023 (1996) (cit. on p. 74).

[109] D. Xiao, W. Yao, and Q. Niu, "Valley-Contrasting Physics in Graphene: Magnetic Moment and Topological Transport", Phys. Rev. Lett. **99**, 236809 (4 p.) (2007) (cit. on pp. 74, 76–78, 81, 97).

[110] K. F. Mak, K. L. McGill, J. Park, and P. L. McEuen, "The valley Hall effect in MoS_2 transistors", Science **344**, 1489–1492 (2014) (cit. on p. 74).

[111] R. V. Gorbachev, J. C. W. Song, G. L. Yu, A. V. Kretinin, F. Withers, Y. Cao, A. Mishchenko, I. V. Grigorieva, K. S. Novoselov, L. S. Levitov, and A. K. Geim, "Detecting topological currents in graphene superlattices", Science **346**, 448–451 (2014) (cit. on pp. 74, 77).

[112] W. Feng, Y. Yao, W. Zhu, J. Zhou, W. Yao, and D. Xiao, "Intrinsic spin Hall effect in monolayers of group-VI dichalcogenides: A first-principles study", Phys. Rev. B **86**, 165108 (6 p.) (2012) (cit. on p. 74).

[113] D. Xiao, G.-B. Liu, W. Feng, X. Xu, and W. Yao, "Coupled Spin and Valley Physics in Monolayers of MoS_2 and Other Group-VI Dichalcogenides", Phys. Rev. Lett. **108**, 196802 (5 p.) (2012) (cit. on pp. 74, 78).

[114] F. Zhang, J. Jung, G. A. Fiete, Q. Niu, and A. H. MacDonald, "Spontaneous Quantum Hall States in Chirally Stacked Few-Layer Graphene Systems", Phys. Rev. Lett. **106**, 156801 (4 p.) (2011) (cit. on pp. 75–78).

[115] H. Min, G. Borghi, M. Polini, and A. H. MacDonald, "Pseudospin magnetism in graphene", Phys. Rev. B **77**, 041407 (4 p.) (2008) (cit. on p. 75).

[116] F. Zhang, H. Min, M. Polini, and A. MacDonald, "Spontaneous inversion symmetry breaking in graphene bilayers", Phys. Rev. B **81**, 041402 (4 p.) (2010) (cit. on p. 75).

[117] R. Nandkishore and L. Levitov, "Quantum anomalous Hall state in bilayer graphene", Phys. Rev. B **82**, 115124 (8 p.) (2010) (cit. on p. 75).

[118] J. Jung, F. Zhang, and A. H. MacDonald, "Lattice theory of pseudospin ferromagnetism in bilayer graphene: Competing interaction-induced quantum Hall states", Phys. Rev. B **83**, 115408 (12 p.) (2011) (cit. on pp. 75, 78).

[119] M. M. Grujić, M. Ž. Tadić, and F. M. Peeters, "Orbital magnetic moments in insulating Dirac systems: Impact on magnetotransport in graphene van der Waals heterostructures", Phys. Rev. B **90**, 205408 (10 p.) (2014) (cit. on p. 75).

[120] W. Yao, D. Xiao, and Q. Niu, "Valley-dependent optoelectronics from inversion symmetry breaking", Phys. Rev. B **77**, 235406 (7 p.) (2008) (cit. on pp. 76, 78).

[121] D. Xiao, M.-C. Chang, and Q. Niu, "Berry phase effects on electronic properties", Rev. Mod. Phys. **82**, 1959–2007 (2010) (cit. on pp. 76–78).

[122] M.-C. Chang and Q. Niu, "Berry curvature, orbital moment, and effective quantum theory of electrons in electromagnetic fields", J. Phys.: Condens. Matter **20**, 193202 (17 p.) (2008) (cit. on p. 76).

[123] M Gradhand, D. Fedorov, F Pientka, P Zahn, I Mertig, and B. Györffy, "First-principle calculations of the Berry curvature of Bloch states for charge and spin transport of electrons", J. Phys.: Condens. Matter **24**, 213202 (23 p.) (2012) (cit. on p. 76).

[124] M. Ezawa, "Spin-valley optical selection rule and strong circular dichroism in silicene", Phys. Rev. B **86**, 161407 (4 p.) (2012) (cit. on p. 78).

[125] A. Kormányos, V. Zólyomi, N. D. Drummond, and G. Burkard, "Spin-Orbit Coupling, Quantum Dots, and Qubits in Monolayer Transition Metal Dichalcogenides", Phys. Rev. X **4**, 011034 (16 p.) (2014) (cit. on p. 78).

[126] C. J. Tabert and E. J. Nicol, "Valley-Spin Polarization in the Magneto-Optical Response of Silicene and Other Similar 2D Crystals", Phys. Rev. Lett. **110**, 197402 (5 p.) (2013) (cit. on pp. 79, 80).

[127] P. Ostrovsky, I. Gornyi, and A. Mirlin, "Theory of anomalous quantum Hall effects in graphene", Phys. Rev. B **77**, 195430 (13 p.) (2008) (cit. on pp. 79, 80).

[128] P. Krstajić and P Vasilopoulos, "Integer quantum Hall effect in gapped single-layer graphene", Phys. Rev. B **86**, 115432 (8 p.) (2012) (cit. on p. 80).

[129] J. L. Lado, J. W. González, and J. Fernández-Rossier, "Quantum Hall effect in gapped graphene heterojunctions", Phys. Rev. B **88**, 035448 (11 p.) (2013) (cit. on p. 80).

[130] M. Ezawa, "Valley-Polarized Metals and Quantum Anomalous Hall Effect in Silicene", Phys. Rev. Lett. **109**, 055502 (5 p.) (2012) (cit. on p. 80).

[131] X. Li, F. Zhang, and Q. Niu, "Unconventional Quantum Hall Effect and Tunable Spin Hall Effect in Dirac Materials: Application to an Isolated MoS_2 Trilayer", Phys. Rev. Lett. **110**, 066803 (5 p.) (2013) (cit. on p. 81).

[132] T. Cai, S. A. Yang, X. Li, F. Zhang, J. Shi, W. Yao, and Q. Niu, "Magnetic control of the valley degree of freedom of massive Dirac fermions with application to transition metal dichalcogenides", Phys. Rev. B **88**, 115140 (8 p.) (2013) (cit. on pp. 81, 82).

[133] M. Koshino and T. Ando, "Anomalous orbital magnetism in Dirac-electron systems: Role of pseudospin paramagnetism", Phys. Rev. B **81**, 195431 (9 p.) (2010) (cit. on pp. 81, 82).

[134] L. Majidi and M. Zareyan, "Pseudospin polarized quantum transport in monolayer graphene", Phys. Rev. B **83**, 115422 (6 p.) (2011) (cit. on p. 81).

[135] M. R. Masir, P Vasilopoulos, A Matulis, and F. Peeters, "Direction-dependent tunneling through nanostructured magnetic barriers in graphene", Phys. Rev. B **77**, 235443 (11 p.) (2008) (cit. on pp. 83, 96, 98).

[136] M. M. Grujić, M. Ž. Tadić, and F. M. Peeters, "Spin-Valley Filtering in Strained Graphene Structures with Artificially Induced Carrier Mass and Spin-Orbit Coupling", Phys. Rev. Lett. **113**, 046601 (5 p.) (2014) (cit. on pp. 83, 90).

[137] M. R. Masir, P Vasilopoulos, and F. Peeters, "Tunneling, conductance, and wavevector filtering through magnetic barriers in bilayer graphene", Phys. Rev. B **79**, 035409 (8 p.) (2009) (cit. on p. 88).

[138] M.-H. Liu, J. Bundesmann, and K. Richter, "Spin-dependent Klein tunneling in graphene: Role of Rashba spin-orbit coupling", Phys. Rev. B **85**, 085406 (9 p.) (2012) (cit. on p. 90).

[139] F Guinea, M. Katsnelson, and A. Geim, "Energy gaps and a zero-field quantum Hall effect in graphene by strain engineering", Nature Phys. **6**, 30–33 (2009) (cit. on p. 90).

[140] D. Pesin and A. H. MacDonald, "Spintronics and pseudospintronics in graphene and topological insulators", Nature Mater. **11**, 409–416 (2012) (cit. on pp. 91, 101).

[141] N. Tombros, C. Jozsa, M. Popinciuc, H. T. Jonkman, and B. J. Van Wees, "Electronic spin transport and spin precession in single graphene layers at room temperature", Nature (London) **448**, 571–574 (2007) (cit. on p. 91).

[142] P. Zomer, M. Guimaraes, N Tombros, and B. van Wees, "Long-distance spin transport in high-mobility graphene on hexagonal boron nitride", Phys. Rev. B **86**, 161416 (4 p.) (2012) (cit. on pp. 91, 101).

[143] A Rycerz, J Tworzydło, and C. Beenakker, "Valley filter and valley valve in graphene", Nature Phys. **3**, 172–175 (2007) (cit. on p. 91).

[144] N Levy, S. Burke, K. Meaker, M Panlasigui, A Zettl, F Guinea, A. C. Neto, and M. Crommie, "Strain-Induced Pseudo–Magnetic Fields Greater Than 300 Tesla in Graphene Nanobubbles", Science **329**, 544–547 (2010) (cit. on p. 91).

[145] A. Geim and I. Grigorieva, "Van der Waals heterostructures", Nature (London) **499**, 419–425 (2013) (cit. on p. 91).

[146] X. Zhong, Y. K. Yap, R. Pandey, and S. P. Karna, "First-principles study of strain-induced modulation of energy gaps of graphene/BN and BN bilayers", Phys. Rev. B **83**, 193403 (4 p.) (2011) (cit. on pp. 92, 100).

[147] B Sachs, T. Wehling, M. Katsnelson, and A. Lichtenstein, "Adhesion and electronic structure of graphene on hexagonal boron nitride substrates", Phys. Rev. B **84**, 195414 (7 p.) (2011) (cit. on pp. 92, 100).

[148] M Kindermann, B. Uchoa, and D. Miller, "Zero-energy modes and gate-tunable gap in graphene on hexagonal boron nitride", Phys. Rev. B **86**, 115415 (4 p.) (2012) (cit. on pp. 92, 100).

[149] F Amet, J. Williams, K Watanabe, T Taniguchi, and D Goldhaber-Gordon, "Insulating Behavior at the Neutrality Point in Single-Layer Graphene", Phys. Rev. Lett. **110**, 216601 (5 p.) (2013) (cit. on pp. 92, 100).

[150] C. Weeks, J. Hu, J. Alicea, M. Franz, and R. Wu, "Engineering a Robust Quantum Spin Hall State in Graphene via Adatom Deposition", Phys. Rev. X **1**, 021001 (15 p.) (2011) (cit. on pp. 92, 101).

[151] J. Hu, J. Alicea, R. Wu, and M. Franz, "Giant Topological Insulator Gap in Graphene with 5 d Adatoms", Phys. Rev. Lett. **109**, 266801 (5 p.) (2012) (cit. on pp. 92, 101).

[152] K.-H. Jin and S.-H. Jhi, "Proximity-induced giant spin-orbit interaction in epitaxial graphene on a topological insulator", Phys. Rev. B **87**, 075442 (6 p.) (2013) (cit. on pp. 92, 101).

[153] V. M. Pereira, A. C. Neto, and N. Peres, "Tight-binding approach to uniaxial strain in graphene", Phys. Rev. B **80**, 045401 (8 p.) (2009) (cit. on p. 92).

[154] R. Ribeiro, V. M. Pereira, N. Peres, P. Briddon, and A. C. Neto, "Strained graphene: tight-binding and density functional calculations", New. J. Phys. **11**, 115002 (11 p.) (2009) (cit. on p. 92).

[155] M Ramezani Masir, D Moldovan, and F. Peeters, "Pseudo magnetic field in strained graphene: Revisited", Solid State Communications **175**, 76–82 (2013) (cit. on p. 92).

[156] H. Suzuura and T. Ando, "Phonons and electron-phonon scattering in carbon nanotubes", Phys. Rev. B **65**, 235412 (15 p.) (2002) (cit. on p. 93).

[157] J. L. Manes, "Symmetry-based approach to electron-phonon interactions in graphene", Phys. Rev. B **76**, 045430 (10 p.) (2007) (cit. on p. 93).

[158] F. de Juan, M. Sturla, and M. A. Vozmediano, "Space Dependent Fermi Velocity in Strained Graphene", Phys. Rev. Lett. **108**, 227205 (5 p.) (2012) (cit. on p. 93).

[159] A. L. Kitt, V. M. Pereira, A. K. Swan, and B. B. Goldberg, "Lattice-corrected strain-induced vector potentials in graphene", Phys. Rev. B **85**, 115432 (6 p.) (2012) (cit. on p. 93).

[160] A. L. Kitt, V. M. Pereira, A. K. Swan, and B. B. Goldberg, "Erratum: Lattice-corrected strain-induced vector potentials in graphene [Phys. Rev. B 85, 115432 (2012)]", Phys. Rev. B **87**, 159909 (2 p.) (2013) (cit. on p. 93).

[161] F. de Juan, J. L. Mañes, and M. A. Vozmediano, "Gauge fields from strain in graphene", Phys. Rev. B **87**, 165131 (6 p.) (2013) (cit. on p. 93).

[162] M. Ezawa, "Single Dirac-cone state and quantum Hall effects in a honeycomb structure", Europhys. Lett. **104**, 27006 (5 p.) (2013) (cit. on p. 94).

[163] A. Chaves, L Covaci, K. Y. Rakhimov, G. Farias, and F. Peeters, "Wave-packet dynamics and valley filter in strained graphene", Phys. Rev. B **82**, 205430 (11 p.) (2010) (cit. on p. 94).

[164] M. R. Masir, A Matulis, and F. Peeters, "Scattering of Dirac electrons by circular mass barriers: Valley filter and resonant scattering", Phys. Rev. B **84**, 245413 (9 p.) (2011) (cit. on p. 94).

[165] Z. Wu, F Zhai, F. Peeters, H. Xu, and K. Chang, "Valley-Dependent Brewster Angles and Goos-Hänchen Effect in Strained Graphene", Phys. Rev. Lett. **106**, 176802 (4 p.) (2011) (cit. on p. 94).

[166] D Moldovan, M. R. Masir, L Covaci, and F. Peeters, "Resonant valley filtering of massive Dirac electrons", Phys. Rev. B **86**, 115431 (12 p.) (2012) (cit. on p. 94).

[167] Y. Jiang, T. Low, K. Chang, M. I. Katsnelson, and F. Guinea, "Generation of Pure Bulk Valley Current in Graphene", Phys. Rev. Lett. **110**, 046601 (5 p.) (2013) (cit. on p. 94).

[168] N. Myoung and G. Ihm, "Valley-dependent resonant tunneling through double magnetic barriers in suspended graphene", arXiv preprint arXiv:1312.2667 (2013) (cit. on p. 94).

[169] W.-F. Tsai, C.-Y. Huang, T.-R. Chang, H. Lin, H.-T. Jeng, and A. Bansil, "Gated silicene as a tunable source of nearly 100% spin-polarized electrons", Nat. Commun. **4**, 1500 (6 p.) (2013) (cit. on p. 94).

[170] W.-T. Lu, W. Li, Y.-L. Wang, H. Jiang, and C.-T. Xu, "Tunable wavevector and spin filtering in graphene induced by resonant tunneling", Appl. Phys. Lett. **103**, 062108 (4 p.) (2013) (cit. on p. 94).

[171] T. Yokoyama, "Controllable valley and spin transport in ferromagnetic silicene junctions", Phys. Rev. B **87**, 241409 (4 p.) (2013) (cit. on p. 94).

[172] A De Martino, L DellAnna, and R Egger, "Magnetic Confinement of Massless Dirac Fermions in Graphene", Phys. Rev. Lett. **98**, 066802 (4 p.) (2007) (cit. on pp. 96, 98).

[173] F Guinea, A. Geim, M. Katsnelson, and K. Novoselov, "Generating quantizing pseudomagnetic fields by bending graphene ribbons", Phys. Rev. B **81**, 035408 (5 p.) (2010) (cit. on p. 100).

[174] L. Ponomarenko, R. Gorbachev, G. Yu, D. Elias, R Jalil, A. Patel, A Mishchenko, A. Mayorov, C. Woods, J. Wallbank, M. Mucha-Kruczynski, B. A. Piot, M. Potemski, I. V. Grigorieva, K. S. Novoselov, F. Guinea, V. I. Falko, and A. K. Geim, "Cloning of Dirac fermions in graphene superlattices", Nature (London) **497**, 594–597 (2013) (cit. on p. 100).

[175] C. Dean, L Wang, P Maher, C Forsythe, F Ghahari, Y Gao, J Katoch, M Ishigami, P Moon, M Koshino, et al., "Hofstadter's butterfly and the fractal quantum Hall effect in moiré superlattices", Nature (London) **497**, 598–602 (2013) (cit. on p. 100).

[176] M Zarenia, O Leenaerts, B Partoens, and F. Peeters, "Substrate-induced chiral states in graphene", Phys. Rev. B **86**, 085451 (5 p.) (2012) (cit. on p. 100).

[177] M Neek-Amal and F. Peeters, "Graphene on hexagonal lattice substrate: Stress and pseudo-magnetic field", Appl. Phys. Lett. **104**, 173106 (5 p.) (2014) (cit. on p. 101).

[178] H Ochoa, A. C. Neto, and F Guinea, "Elliot-Yafet Mechanism in Graphene", Phys. Rev. Lett. **108**, 206808 (5 p.) (2012) (cit. on p. 101).

[179] C. Volk, C. Neumann, S. Kazarski, S. Fringes, S. Engels, F. Haupt, A. Müller, and C. Stampfer, "Probing relaxation times in graphene quantum dots", Nat. Commun. **4**, 1753 (6 p.) (2013) (cit. on p. 103).

[180] V. V. Cheianov and V. I. Falko, "Selective transmission of Dirac electrons and ballistic magnetoresistance of n-p junctions in graphene", Phys. Rev. B **74**, 041403 (4 p.) (2006) (cit. on p. 105).

[181] J. M. Luttinger, "The Effect of a Magnetic Field on Electrons in a Periodic Potential", Phys. Rev. B **84**, 814–817 (1951) (cit. on p. 108).

[182] R. Peierls, "Zur Theorie des Diamagnetismus von Leitungselektronen", Z. Phys. **80**, 763–791 (1933) (cit. on p. 108).

[183] R. P. Feynman, *Lectures on Physics Vol. iii* (Addison-Wesley, New York, Les Ulis Cedex, 1965) (cit. on p. 108).

Biography

Marko M. Grujić was born in Belgrade, Serbia on January 25th, 1987. After completing "Nikola Tesla" electrotechnical high school in 2005, he enrolled in the School of Electrical Engineering, University of Belgrade. He graduated from the Department of Physical Electronics in 2009 with the GPA of 9,70 (out of 10) with a Bachelor's thesis titled "Laterally coupled quantum dots under the influence of electric and magnetic field". He received the award for the best student of the Department in 2009.

In October 2009 he enrolled in the Master studies at the Department of Physical Electronics of the School of Electrical Engineering, and graduated in October 2010 with a Master thesis titled "Electronic structure of graphene quantum dots in a normal magnetic field". Soon afterwards he enrolled in the PhD program in Nanoelectronics and photonics. He has been pursuing the PhD degree under the title "Manifestations of intrinsic and induced magnetic properties of graphene nanostructures". The work on this topic has been jointly organized by the School of Electrical Engineering, University of Belgrade and the Department of Physics, University of Antwerp. He has been affiliated with the School of Electrical Engineering, University of Belgrade, as a researcher in the project "Optoelectronic nanodimensional systems - the road to applications" of the Ministry of Education, Science and Technological Development of Serbia.

The most important research results of the Ph.D. candidate Marko M. Grujić are summarized in four articles published in leading international journals (M21 category), and one article published in an international journal (M23). In all of his publications Marko Grujić was the first signed author.

List of Publications

1. Marko M. Grujić, Milan Ž. Tadić, and François M. Peeters, Spin-valley filtering in strained graphene structures with artificially induced carrier mass and spin-orbit coupling, *Phys. Rev. Lett.* **113**, 046601 (2014). [6]

2. Marko M. Grujić, Milan Ž. Tadić, and François M. Peeters, Orbital magnetic moments in insulating Dirac systems: Impact on magnetotransport in graphene van der Waals heterostructures, *Phys. Rev. B* **90**, 205408 (2014). [5]

3. M. Grujić, M. Tadić, and F. M. Peeters, Antiferromagnetism in hexagonal graphene structures: Rings versus dots, *Phys. Rev. B* **87**, 085434 (2013). [4]

4. M. Grujić, M. Zarenia, M. Tadić, and F. Peeters, Interband optical absorption in a circular graphene quantum dot, *Physica Scripta* **2012**, 014056 (2012). [3]

5. M. Grujić, M. Zarenia, A. Chaves, M. Tadić, G. Farias, and F. M. Peeters, Electronic and optical properties of a circular graphene quantum dot in a magnetic field: influence of the boundary conditions, *Phys. Rev. B* **84**, 205441 (2011). [3]

The numbers in square brackets refer to the chapters in this thesis which include the results presented in the actual publication.

Прилог 1.

Изјава о ауторству

Потписани-а Марко М. Грујић

број индекса 10/5003

Изјављујем

да је докторска дисертација под насловом

Испољавање сопствених и индукованих магнетских својстава графенских наноструктура

Manifestations of intrinsic and induced magnetic properties of graphene nanostructures

- резултат сопственог истраживачког рада,
- да предложена дисертација у целини ни у деловима није била предложена за добијање било које дипломе према студијским програмима других високошколских установа,
- да су резултати коректно наведени и
- да нисам кршио/ла ауторска права и користио интелектуалну својину других лица.

Потпис докторанда

У Београду, 09.02.2015. год.

Прилог 2.

Изјава о истоветности штампане и електронске верзије докторског рада

Име и презиме аутора Марко М. Грујић

Број индекса 10/5003

Студијски програм Наноелектроника и фотоника

Наслов рада Испољавање сопствених и индукованих магнетских својстава графенских наноструктура (Manifestations of intrinsic and induced magnetic properties of graphene nanostructures)

Ментор Проф. Др Милан Ж. Тадић, Prof. Dr. François M. Peeters

Потписани/а Марко М. Грујић

Изјављујем да је штампана верзија мог докторског рада истоветна електронској верзији коју сам предао/ла за објављивање на порталу **Дигиталног репозиторијума Универзитета у Београду.**

Дозвољавам да се објаве моји лични подаци везани за добијање академског звања доктора наука, као што су име и презиме, година и место рођења и датум одбране рада.

Ови лични подаци могу се објавити на мрежним страницама дигиталне библиотеке, у електронском каталогу и у публикацијама Универзитета у Београду.

Потпис докторанда

У Београду, 09.02.2015. год.

Прилог 3.

Изјава о коришћењу

Овлашћујем Универзитетску библиотеку „Светозар Марковић“ да у Дигитални репозиторијум Универзитета у Београду унесе моју докторску дисертацију под насловом:

Испољавање сопствених и индукованих магнетских својстава графенских наноструктура

Manifestations of intrinsic and induced magnetic properties of graphene nanostructures

---

која је моје ауторско дело.

Дисертацију са свим прилозима предао/ла сам у електронском формату погодном за трајно архивирање.

Моју докторску дисертацију похрањену у Дигитални репозиторијум Универзитета у Београду могу да користе сви који поштују одредбе садржане у одабраном типу лиценце Креативне заједнице (Creative Commons) за коју сам се одлучио/ла.

1. Ауторство
2. Ауторство - некомерцијално
3. Ауторство – некомерцијално – без прераде
4. Ауторство – некомерцијално – делити под истим условима
5. Ауторство – без прераде
6. Ауторство – делити под истим условима

(Молимо да заокружите само једну од шест понуђених лиценци, кратак опис лиценци дат је на полеђини листа).

Потпис докторанда

У Београду, 09.02.2015. год.